UNIVERSITY OF COPENHAGEN
FACULTY OF SCIENCE

MSc thesis

Superconductivity in kagome materials:

The possible pairing states and the effect of impurities

Sofie Castro Holbæk

Advisor: Brian Møller Andersen

Submitted: August 6, 2023

Abstract

It was recently discovered that a family of compounds, AV_3Sb_5 ($A = K, Rb, Cs$), becomes superconducting at low temperature. All three compounds feature layers of vanadium atoms organized in a two-dimensional kagome lattice. At present, there is no full consensus regarding the symmetry of the superconducting order parameter. Motivated by this, the aim of the current thesis is to study superconductivity on a kagome lattice with an emphasis on modelling impurity probes. We focus on the effects of impurities since, in many cases, they act as phase-sensitive probes.

Within mean-field theory we systematically classify all symmetry-allowed superconducting states on a two-dimensional kagome lattice up to third nearest neighbor interactions. The pairing states are illustrated both in real and momentum space, and the pairing matrices are explicitly written. The classification reveals two main findings: first of all we find that (in addition to the regular s-wave case) an order parameter with d-wave symmetry can arise from on-site interactions. Secondly, at the level of nearest neighbor interactions, a set of pairing states which corresponds exclusively to interband pairing is allowed on the kagome lattice.

Proceeding with the intraband pairing states as they open up a gap at the Fermi energy, we study the response to single point-like potential and magnetic impurities. Due to the fact that a point-like potential impurity is located on a lattice site which has lower symmetry than the lattice itself, the electronic wave functions on the kagome lattice are found to only give non-zero weight to certain portions of the Fermi surface. This, combined with an even-parity order parameter like a d-wave gap, leads to a d-wave condensate reacting to impurities effectively like an s-wave superconductor. Consequently, no low-energy bound states are found within the full gap of a system with $d + id$ superconductivity. This is the case although a d-wave superconductor conventionally would be sensitive to potential impurities. For comparison with the results on the kagome lattice, a single-impurity study on the square lattice is additionally presented.

Furthermore, the suppression of the critical temperature by an impurity average is studied and shows that an unconventional singlet order parameter with d-wave symmetry is less sensitive to potential impurities while unconventional triplet order parameters remain sensitive. This result is in agreement with our single-impurity study. Lastly, we discuss the simplifying assumptions made and the implications of our findings for other systems.

The study presented in the thesis nuances the discussion of impurity effects in superconductors, and it shows that conventional results may not always apply if the site symmetry is smaller than the point group symmetry of the lattice.

Acknowledgements

> "I wanna thank me for believin' in me, I wanna thank me for doin' all this hard work... I wanna thank me for being me at all times"
>
> *Snoop Dogg*
> upon receiving Walk of Fame star

Although it is a common impression that scientific discoveries are made single handedly by some genius who locks her-/himself in an office and works very hard on solving a problem on her/his own, my experience is that the best scientific understanding is gained through discussions and with open doors. In this regard I have many people to thank.

I am very grateful to Brian M. Andersen and Morten H. Christensen for their guidance, support and interest in my project work and for always being available for meetings during which they have frequently made me laugh from telling such amusing anecdotes. Thank you Brian for being a down-to-earth supervisor and for introducing me to the wonderfully interesting topic of my thesis. A big thank you to Morten who has given me invaluable lessons in everything from group theory, Inkscape to bouldering. I want to thank Andreas Kreisel whose physical intuition has impressed me over and over and who always meets me with a happy smile. Thank you to Henrik S. Røising, Mercè Roig and Clara N. Beiø for making me feel like a part of the group. Thank you Henrik for sharing a lot of good references and to Mercè for showing me how to use the CMT cluster. Thank you also to Per Hedegård for the coffee break discussions and for inspiring me with your physical understanding.

I have truly enjoyed going to the office, especially because it meant being together with my lovely office mates, Eva and Luca, and meeting with Madalena and Qiyu for lunch break. From a physics perspective, thank you for all of the discussions we had and from which I have learned a lot, but more importantly, thank you for being my friends and for sharing so many fun experiences with me.

Thank you to Simon for bringing joy to my everyday life and to Gry for always being there.

I am every day thankful for my family: Lisa and company (Jon, Rosa and Leo), David, mor and papa. Life has meaning because of you.

Dedicado a mi querido tío Emilio.

Contents

Chapter 1

Introduction

"Kwik nagenoeg nul."

Dutch physicist Heike Kamerlingh Onnes, April 8, 1911 in his laboratory notebook

Before 1908 the lowest achievable temperature in a laboratory was 14 K [1]. Back then, it was understood that electrons cause electrical conductance, but one of the questions physicists of the time were trying to answer was what would happen to the resistivity of a metal upon cooling it to absolute zero. One of the theories brought forward by Lord Kelvin in 1902 was that the mobility of the electrons would be reduced at low temperatures such that the resistivity eventually would go to infinity at absolute zero [1]. Other than this, it was expected that the resistivity would decrease until reaching a constant level, the value of which would depend on the purity of the sample. A breakthrough for low-temperature physics happened in 1908 when Dutch physicist Heike Kamerlingh Onnes together with his coworkers in their laboratory in Leiden succeeded in liquefying helium. Following this, they started experimenting with cooling of platinum wires and found that the resistivity became constant below 4.25 K, thus ruling out the theory by Kelvin [1]. They then started experimenting with mercury, and in a laboratory notebook from April 1911 the words "Kwik nagenoeg nul" were scribbled down. Loosely translated, the phrase means "Quick[silver] close-enough to zero" [1]. Maybe not as poetic as the first words spoken by the first person on the moon, but nevertheless they heralded a new era: the era of superconductivity.

At present time, superconducting materials still only enter their superconducting phase at rather low temperature as compared to room-temperature. Figure 1.1 shows a timeline of a selection of discovered superconducting materials and their critical temperatures. The highest achieved critical temperatures, T_c, at ambient pressure are for copper-oxide superconductors (cuprates), represented by blue diamonds in Figure 1.1, where $T_c \sim 140$ K. One important present application of superconductors is for magnetic resonant imaging (MRI), where superconductors are used to generate the high magnetic fields necessary for the technology which has allowed doctors to image structures deep within a living body. Another application is in the development of quantum computers where superconducting materials are used in many cases as the basis for building quantum bits. Furthermore, if superconductors were to work at room-temperature and ambient pressure, an important application would be to use them for efficient electrical transportation, since currently a lot of energy is being lost to heat over the large distances that electricity might have to travel.

After the discovery of superconductivity it would take nearly 50 years before a microscopic theory describing a possible mechanism for superconductivity was put forward. Bardeen, Cooper and Schrieffer formulated what is now known as BCS theory in 1957 [3]. BCS theory explains how a

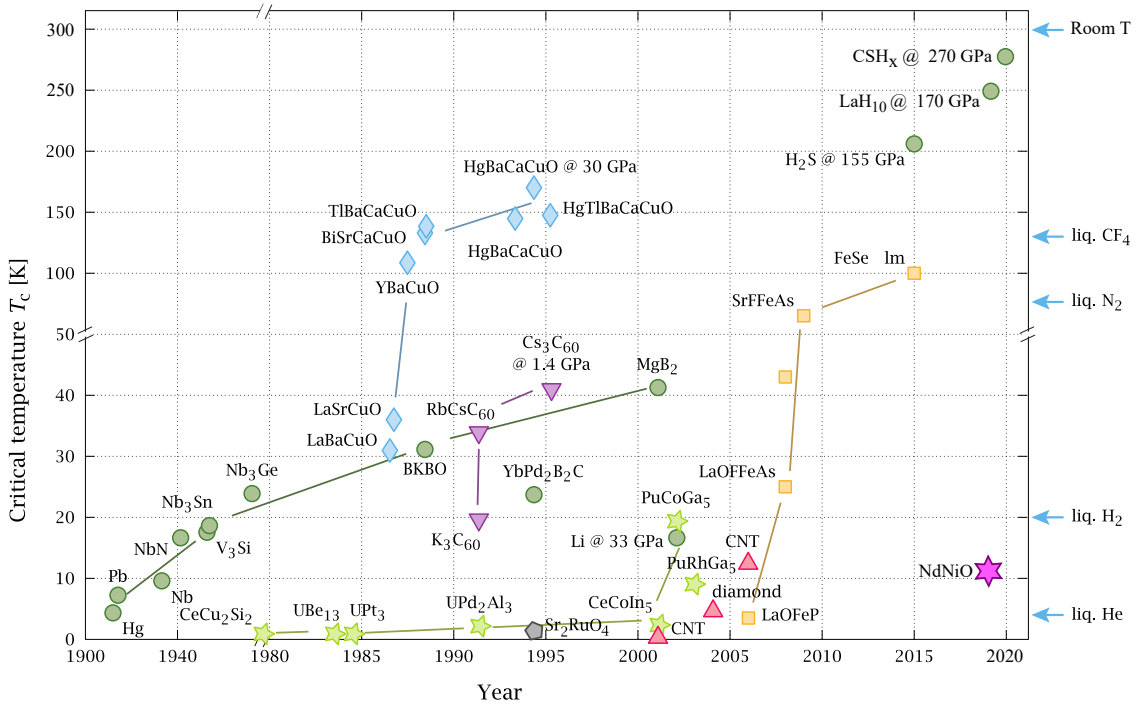

Figure 1.1: A timeline of the discovery of superconductivity in a selection of materials. The critical temperature T_c is given on the left axis. Notice that some of the critical temperatures are reported at high pressure. For comparison the Standard Atmospheric Pressure (defined at sea-level and at 273° K) is $\sim 10^{-4}$ GPa. Additionally, notice that the intervals on the axes change at $T_c = 50$ K and at approximately year 1980. Finally, it should be remarked that the article on superconductivity in the CSH_x compound has been retracted. The marker colours have the purpose of grouping different compounds: the dark green circles represent materials which are known to have properties described well by BCS theory, heavy-fermion based superconductors are represented by light green stars, the cuprates by blue diamonds, iron-based superconductors by orange squares, etc. The illustration is not original, but from [2].

superconducting phase is favorable when the attractive phonon-driven interaction between electrons (with a small energy difference) exceeds the screened repulsive Coulomb force. The theory laid the foundation for our current understanding of superconductivity as a condensate of electrons, the so-called Cooper pairs, forming due to an effective attraction between them [4]. Through BCS theory it is possible to understand and model numerous properties of many superconducting materials, but not all.

In the preface of the book Superconductivity: Volume 2, R. D. Parks writes ”During the preparation of this treatise one of the authors commented that it would be ”the last nail in the coffin [of superconductivity].” While we may hope this is unduly pessimistic, it is clear that the field is well advanced in maturity and sophistication.” [5]. As it turned out, this was by far the last nail in the coffin of superconductivity. By the end of the 1970s, superconductivity was discovered in heavy-fermion materials, and another development was made by Bednorz and Müller in 1986 with their discovery of superconductivity in copper-oxide materials [6]. This second discovery led to a historical March meeting in 1987, later known to condensed matter physicists as ”the Woodstock of physics”, where discussions went on late into the night [7]. The discussions revolved around the discovery of cuprates: a discovery which started a new era of ”high T_c” superconductivity (high T_c compared to former materials but still not room-temperature superconductivity).

Today, one of the big goals of the condensed matter physics community still is to understand what ingredients are necessary to make a room-temperature superconductor. In the search for it, hopefully a lot of useful knowledge is obtained. The present master thesis studies the superconducting phase of a group of materials called AV_3Sb_5. These compounds become superconducting only at $T_c \sim 1 - 3$ K, which would place them at a very low position in Figure 1.1. Surely, these compounds are not high T_c superconductors so what is the rational behind studying them? One motive is that there are still many insights to be gained from "low T_c" superconductors. Several aspects of the superconducting phase of AV_3Sb_5 are not yet well understood, and understanding the mechanism of superconductivity in currently known superconductors is presumably a good stepping stone in the effort of understanding high T_c superconductivity.

As indicated above, there are still many open questions to be answered. In this thesis we present a theoretical study of superconductivity on the kagome lattice, motivated by the superconducting AV_3Sb_5 compounds. The thesis is structured in the following manner: In Chapter 2 we introduce some of the experimental results which have motivated our studies on the AV_3Sb_5 compounds. In Chapter 3 we introduce a simple tight-binding model on the kagome lattice, and in Section 4.3 we do a full classification of the symmetry-allowed mean-field superconducting order parameters on the kagome lattice up to third nearest neighbor interactions. Furthermore, in Chapter 5 an analysis of the response of the different allowed order parameters to single-impurities is carried out, both on the kagome lattice and on the square lattice for comparison. Finally, in Chapter 6 the response to a density of impurities is examined and compared to Abrikosov-Gor'kov theory.

Note: Figures 3.1, 3.3(a), 3.4(c), 5.1, 5.9, 5.10, 5.11, 5.12 and 6.2, and tables 4.2 and 4.3 appear in a similar form in [8]. They are originally made by S. C. Holbæk.

Chapter 2

The kagome metals AV_3Sb_5, $A = K, Rb, Cs$

> "Man kan ikke bruge så lang tid på så lidt."
>
> *Berit Lykke Holbæk aka. mor*

In 2019 three new members of a broader group of kagome materials were synthesized and characterized [9]. The three compounds have the same crystalline structure comprised of an alkali (A) atom: either potassium (K), rubidium (Rb) or cesium (Cs), together with vanadium (V) and antimony atoms (Sb). They are commonly referred to by their chemical name AV_3Sb_5. Following their synthesis, it was discovered in 2020 that the kagome metal CsV_3Sb_5 enters a superconducting phase at a critical temperature $T_c \sim 2.5$ K [10]. Shortly following this, superconductivity was also discovered in the K- and Rb-variants ([11], [12]). These discoveries introduced a new challenge to the superconductivity-community, namely to determine the type of superconductivity present in the materials and to understand its interplay with other competing orders. In this section we give a brief overview of some of the experimental results on the AV_3Sb_5 compounds. We will not attempt to cover all aspects of the discussion, in which case we refer to review papers available on the topic, e.g. [13]. Here, we only cover experimental results which are most essential for our later analysis.

Figure 2.1(a) illustrates the crystalline structure of the AV_3Sb_5 compounds. The crystal consists of alternating layers of alkali atoms (K, Rb, Cs) and V-Sb atoms. The vanadium-atoms make up a kagome lattice and the antimony-atoms make up two sublattices, $Sb1$ and $Sb2$. The $Sb1$ sublattice is positioned in the plane of the kagome lattice and makes up a triangular lattice with Sb atoms centered in the hexagons of the kagome lattice. The $Sb2$ atoms are positioned above and below the V-$Sb1$ layer and form honeycomb lattices. Low temperature measurements of the electrical resistivity shows that the resistivity drops to zero around a critical temperature of $T_c \sim 2.5$ K for CsV_3Sb_5 which, together with other experimental results, demonstrates the occurrence of a second-order phase transition into a superconducting phase, see Figure 2.1(b). Superconductivity sets in at critical temperatures of ~ 0.93 K [11] and ~ 0.92 K [12] for the K- and Rb-variants, respectively.

Measurements of the electrical resistivity and heat capacity at higher temperatures show an additional phase transition occurring at $T_* \sim 94$ K for the Cs-variant [10], $T_* \sim 78$ K for K [11] and $T_* \sim 103$ K for Rb [12]. Figure 2.2(a) shows the electrical resistivity for CsV_3Sb_5 with a visible kink appearing at $T \sim 94$ K. The resistivity measurements show that the out-of-plane (along the

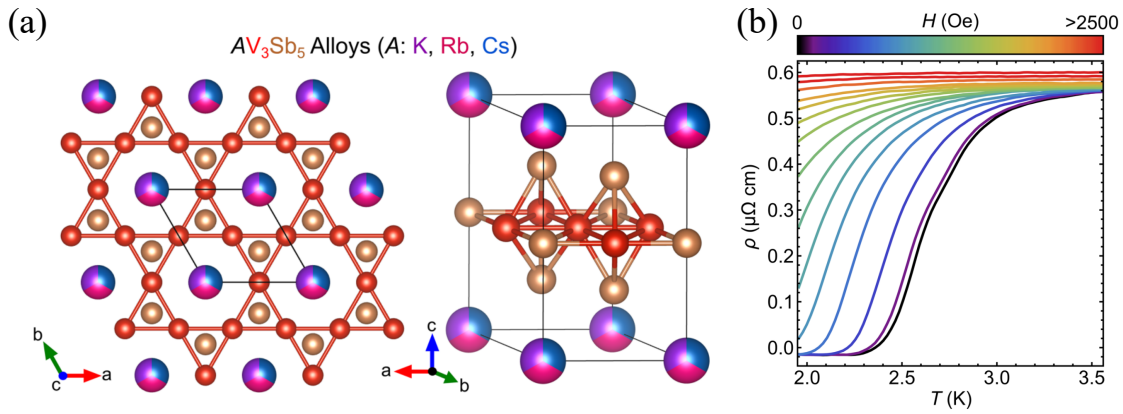

Figure 2.1: (a) The crystalline structure of the AV_3Sb_5 compounds viewed from above (left) and from the side (right). The alkali atom is either K, Rb or Cs but the three compounds are isostructural. The ab-plane is defined to be parallel to the vanadium kagome layer (red) while the c-axis is perpendicular to it. Image from [14]. (b) Low-temperature measurements of the electrical resistivity for single crystals of CsV_3Sb_5. The curves are field-dependent as illustrated in colours. Image from [10].

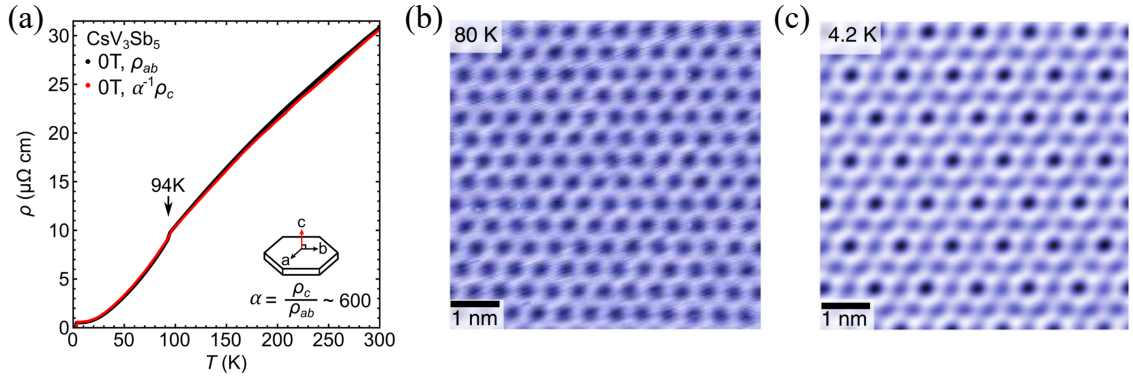

Figure 2.2: (a) Electrical resistivity as a function of temperature for single crystals of CsV_3Sb_5. The resistivity is measured in the ab-plane (black) and in the direction of the c-axis (red). The former is a factor of $\alpha \sim 600$ times smaller than the latter and has thus been multiplied by α for enhanced visibility. Image from [10]. (b) Atomically resolved STM topography of an Sb-surface in the normal phase. The data is for a KV_3Sb_5 crystal which enters the CDW phase at ~ 78 K. Image from [16]. (c) Topography of Sb-surface of KV_3Sb_5 in the CDW phase which compared to (b) shows a 2×2 charge modulation. Image from [16].

c-axis, see the inset of Figure 2.2(a)) resistivity is approximately 600 times larger than the in-plane (the ab-plane) resistivity. The instability at T_* causes a reordering of the electronic charges which expands the in-plane unit cell twice in each direction making a 2×2 modulation. This phase is identified as a charge density wave (CDW). Figure 2.2(b) and (c) show topographic data of an Sb-surface in the normal phase and in the CDW phase, respectively, where the charge modulation is visible. The interplay between CDW and superconductivity has been examined by applying pressure which decreases T_* of the CDW. A study shows that the CDW is entirely suppressed at a pressure of ~ 2 GPa, above which superconductivity persists [15].

The Fermi surface of the materials has been mapped out by angle-resolved photo-emission spectroscopy (ARPES) measurements. ARPES data for CsV_3Sb_5 at 80 K is shown in Figure 2.3(a) and

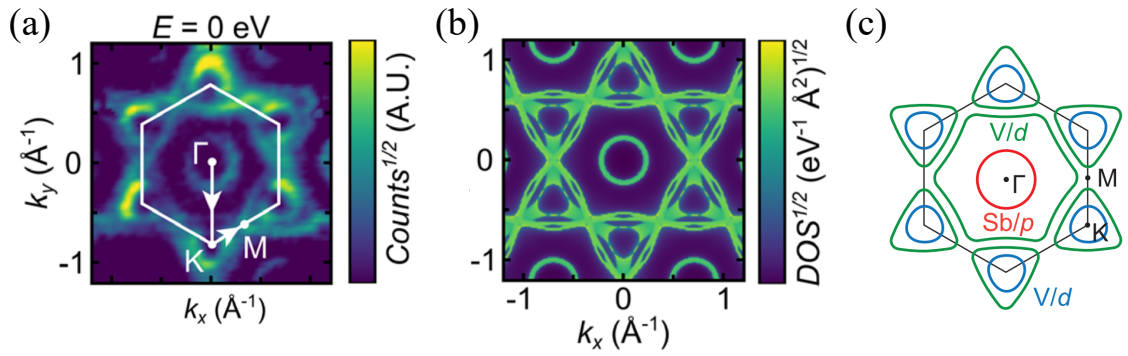

Figure 2.3: (a) ARPES data for CsV_3Sb_5 at 80 K and $E = 0$ eV. The hexagonal Brillouin zone is illustrated in white. Image from [10]. (b) DFT calculations for comparison with (a). Image from [10]. (c) Illustration of the 2D Fermi surface of CsV_3Sb_5 highlighting its different orbital character. Image from [17].

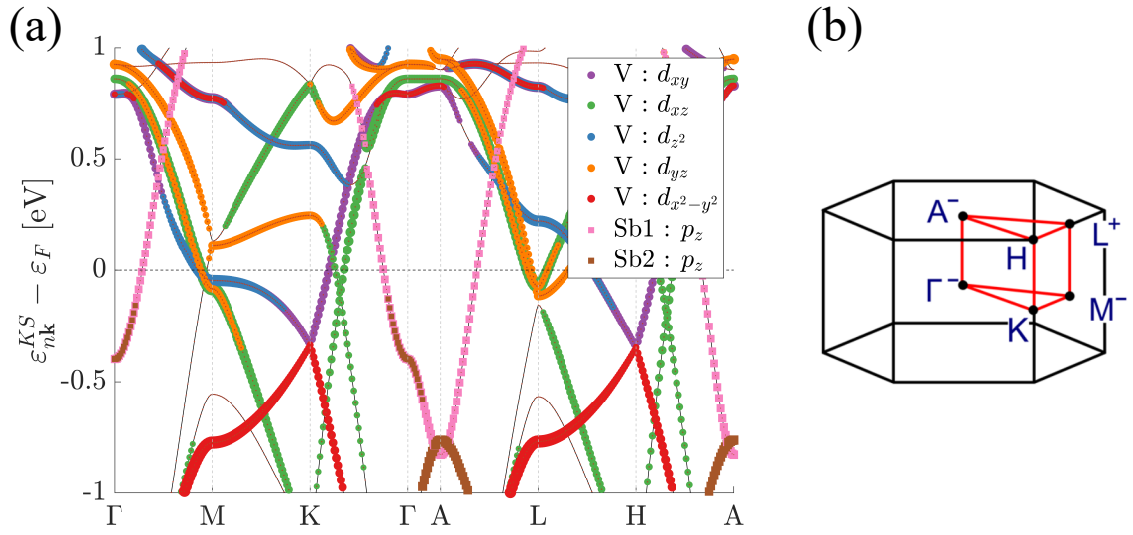

Figure 2.4: (a) The bands close to the Fermi surface have contributions mainly from vanadium d-orbitals and antimony p_z-orbitals. The orbital character is found from projecting the wave functions onto the orbitals shown in the legend. Image from [19]. (b) The Brillouin zone of the $P6/mmm$ space group which the AV_3Sb_5 compounds belong to. Image from [10].

a comparison to Figure 2.3(b) shows good agreement with density-functional theory (DFT) calculations [10]. The 2D Fermi surface has different orbital character as illustrated in Figure 2.3(c): The circular pocket (red) around the central point, called Γ, of the hexagonal Brillouin zone consists of *Sb* p-orbitals, and the hexagonal Fermi surface also centered at Γ consists of vanadium d-orbitals. The circular and triangular Fermi pockets around the K points (blue and green) both consist of vanadium d-orbitals.

A DFT calculation of the bands close to the Fermi surface is shown in Figure 2.4(a), and it illustrates the domination of the vanadium d-orbitals and antimony p_z-orbitals [18] in this range. The band just below the Fermi energy at the M-point is dominated by vanadium d_{z^2}-orbitals and it has a saddle point structure which gives rise to a van Hove singularity in the density of states. In Figure 2.4(b), the high-symmetry points used to generate Figure 2.4(a) are illustrated.

To uncover what type of superconducting order is present in AV_3Sb_5, the effect of impurities

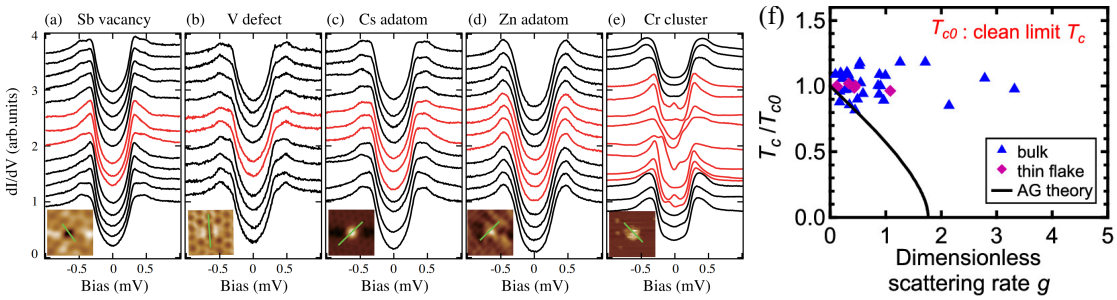

Figure 2.5: (a)-(e) STM scans along the green lines shown in the insets across different impurities in a CsV_3Sb_5 sample. (a) Non-magnetic intrinsic Sb vacancy, (b) non-magnetic hole-like defect on a V site, (b) non-magnetic Cs adatom, (d) non-magnetic Zn adatom evaporated onto the sample and (e) magnetic Cr cluster evaporated onto the sample. The red lines indicate positions close to the impurity. Image from [20]. (f) Evolution of the critical temperature as a function of a dimensionless scattering rate g for thin flakes (pink) and crystals (blue) of CsV_3Sb_5. The black curve depicts the suppression within Abrikosov-Gor'kov theory. Image from [21].

have been studied. This is due to the fact that impurity-effects conventionally are able to reveal whether the order parameter has sign-changes or not. Figure 2.5(a)-(e) shows scanning tunneling microscopy (STM) scans across different impurities on a CsV_3Sb_5 sample. The plots show the differential conductance dI/dV which under certain circumstances (such as an essentially constant density of states of the scanning tip in the energy range of interest) probes the density of states of the material under examination. In the case of Figures 2.5(a) and (b) the impurities have been characterized as being intrinsic hole-like defects on an $Sb1$ site and a V-site, respectively [20]. These defects are regarded as non-magnetic and no effect on the density of states is visible in the region close to the impurity. In particular, no in-gap bound states are observed. The same conclusion applies for the case of a non-magnetic Cs adatom seen in Figure 2.5(c). Non-magnetic Zn atoms and magnetic Cr atoms were independently evaporated onto the surface, and if the adatoms interact weakly with the underlying crystal, it can be assumed that the adatoms retain their (non-)magnetic nature after the evaporation [20]. In the case of the Zn adatom, Figure 2.5(d), the gap is not affected. The story is different for the Cr cluster, where in-gap peaks appear close to the cluster but disappear away from it. In [20] this result is interpreted as an indication of a pairing state which is non-sign-changing as a function of momentum.

Measurements of the critical temperature as a function of scattering rate have additionally been carried out in CsV_3Sb_5, see Figure 2.5(f). The data indicates that the superconducting condensate is insensitive to disorder as compared to the full black line in Figure 2.5(f) corresponding to the curve of Abrikosov-Gor'kov theory. The latter is expected to model the suppression of T_c for an s-wave superconductor in the presence of magnetic impurities as well as the suppression of unconventional superconductivity in the presence of potential impurities.

As a final remark, there has been some indications of the breaking of time-reversal symmetry (TRS) within the CDW phase [22], and thus the superconducting state is *possibly* forming within a TRS broken state.

Chapter 3

Features of the tight-binding model on the kagome lattice

"Ut af mit køkken."

Manuel Castro Pacheco aka. papa

Real materials, such as the AV_3Sb_5 metals, are complex systems containing numerous electrons which might interact strongly with each other and with the vibrational degrees of freedom of the lattice. Other properties such as the three-dimensional nature of a material, spin-orbit coupling, multiple orbitals crossing the Fermi level etc. may further complicate the modelling of real world systems. Nevertheless, specific effects are in some cases weak, and to capture the main aspects of a material it might serve as a good approximation to neglect them. Inspired by literature on the AV_3Sb_5 compounds, we briefly motivate some of the approximations made before introducing a simple tight-binding model on the kagome lattice and discussing its features.

In the case of the AV_3Sb_5 metals, it was shown that there is a strong anisotropy in the electrical conductivity, as mentioned in Chapter 2, which means that the electrons mainly move on a two-dimensional plane. This motivates the approximation of modelling the system as two-dimensional. Furthermore, DFT calculations show that the inclusion of spin-orbit coupling does not alter the energy bands significantly close to the van Hove singularities [23] and hence spin-orbit coupling is omitted in the following description. This approximation is of course not valid for any material. For example, in another material of great interest since it was considered to be a possible candidate for unconventional superconductivity, Sr_2RuO_4, spin-orbit coupling is strong and therefore cannot be ignored [24]. The hexagonal part of the Fermi surface, shown in Chapter 2, is dominated by electrons located on the vanadium kagome lattice, and while some studies indicate the importance of the Γ-pocket Fermi surface which has its main contribution from Sb atoms [25], in this work we study superconductivity on the kagome lattice. Our starting point is to write up a simple model describing electrons moving around on a lattice. We later add superconductivity to the model. Apart from fixing the electronic filling to a value which seems to agree with that of the AV_3Sb_5 compounds, the following results are general and could apply to other kagome materials than the AV_3Sb_5 compounds.

3.1 The tight-binding model

In this section we introduce a tight-binding (TB) model for the two-dimensional kagome lattice. The TB model describes electrons moving around on a lattice by hopping to nearest neighbor sites.

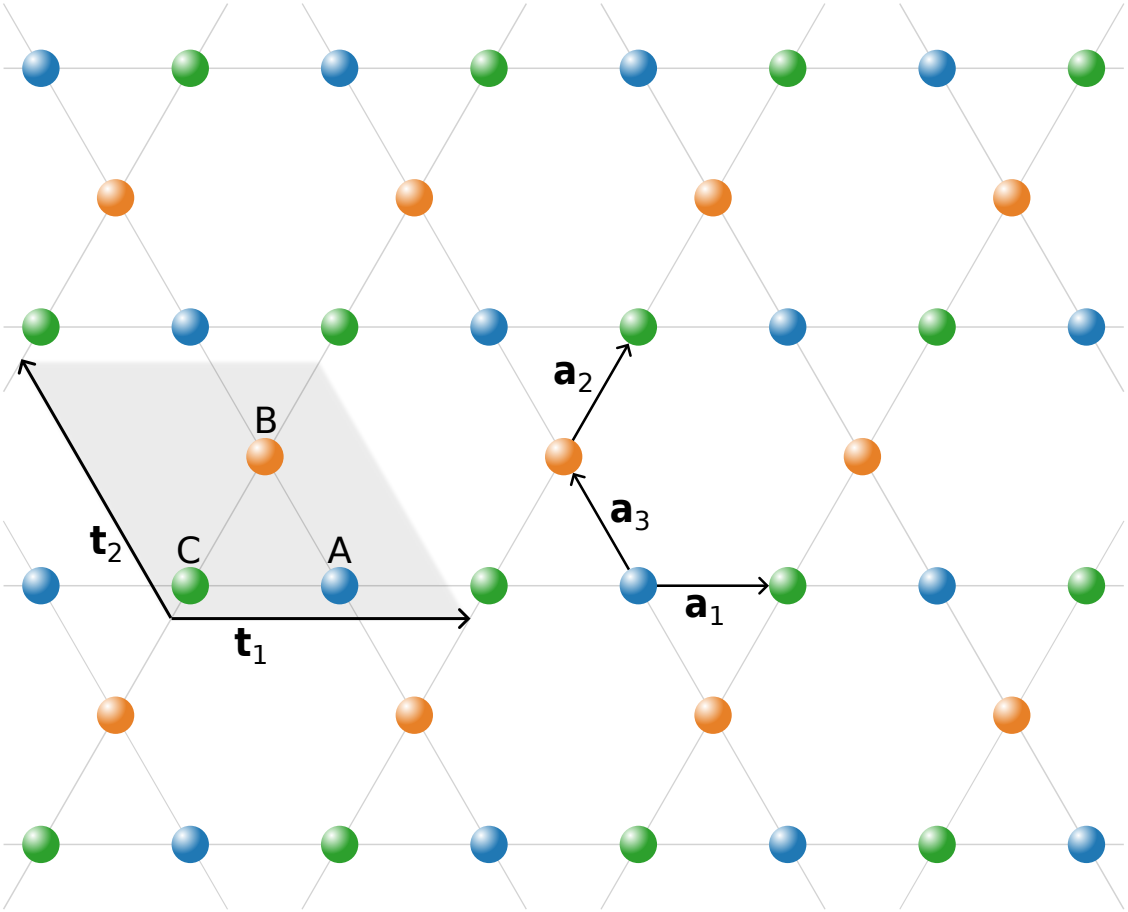

Figure 3.1: Illustration of a finite section of the kagome lattice with the primitive lattice vectors, $\mathbf{t}_1$ and $\mathbf{t}_2$, and the sublattice vectors, $\mathbf{a}_1$, $\mathbf{a}_2$ and $\mathbf{a}_3$, shown. The grey parallelogram illustrates the unit cell with the three sites denoted A (blue), B (orange) and C (green).

The unit cell of the kagome lattice contains three atomic sites which, as will be detailed in the following, give rise to three energy bands. Before writing up the TB Hamiltonian, we need to make a few definitions. The three sites within a unit cell are connected by the vectors

$$\mathbf{a}_1 \equiv \frac{1}{2}\begin{pmatrix}1 & 0\end{pmatrix}^T, \qquad \mathbf{a}_2 \equiv \frac{1}{2}\begin{pmatrix}\frac{1}{2} & \frac{\sqrt{3}}{2}\end{pmatrix}^T, \qquad \mathbf{a}_3 \equiv \frac{1}{2}\begin{pmatrix}-\frac{1}{2} & \frac{\sqrt{3}}{2}\end{pmatrix}^T, \tag{3.1}$$

The primitive lattice vectors which span the lattice in real space are given by

$$\mathbf{t}_1 \equiv \begin{pmatrix}1 & 0\end{pmatrix}^T = 2\mathbf{a}_1\,, \qquad \mathbf{t}_2 \equiv \begin{pmatrix}-\frac{1}{2} & \frac{\sqrt{3}}{2}\end{pmatrix}^T = 2\mathbf{a}_3\,. \tag{3.2}$$

With these definitions we have set the distance between unit cells to 1. An illustration of the kagome lattice, the unit cell and the lattice vectors is seen in Figure 3.1.

The primitive reciprocal lattice vectors are

$$\mathbf{g}_1 \equiv 2\pi\begin{pmatrix}1 & \frac{1}{\sqrt{3}}\end{pmatrix}^T, \qquad \mathbf{g}_2 \equiv 2\pi\begin{pmatrix}0 & \frac{2}{\sqrt{3}}\end{pmatrix}^T. \tag{3.3}$$

The reciprocal lattice vectors are defined such that $\mathbf{t}_i \cdot \mathbf{g}_j = 2\pi\delta_{i,j}$ and in turn $e^{i\mathbf{t}_i\cdot\mathbf{g}_j} = 1$. Since all distances between neighboring sites are equivalent, we set all of the hopping coefficients equal to the same value $t = 1$. This corresponds to modelling an s-orbital per site, or equivalently in the 2D

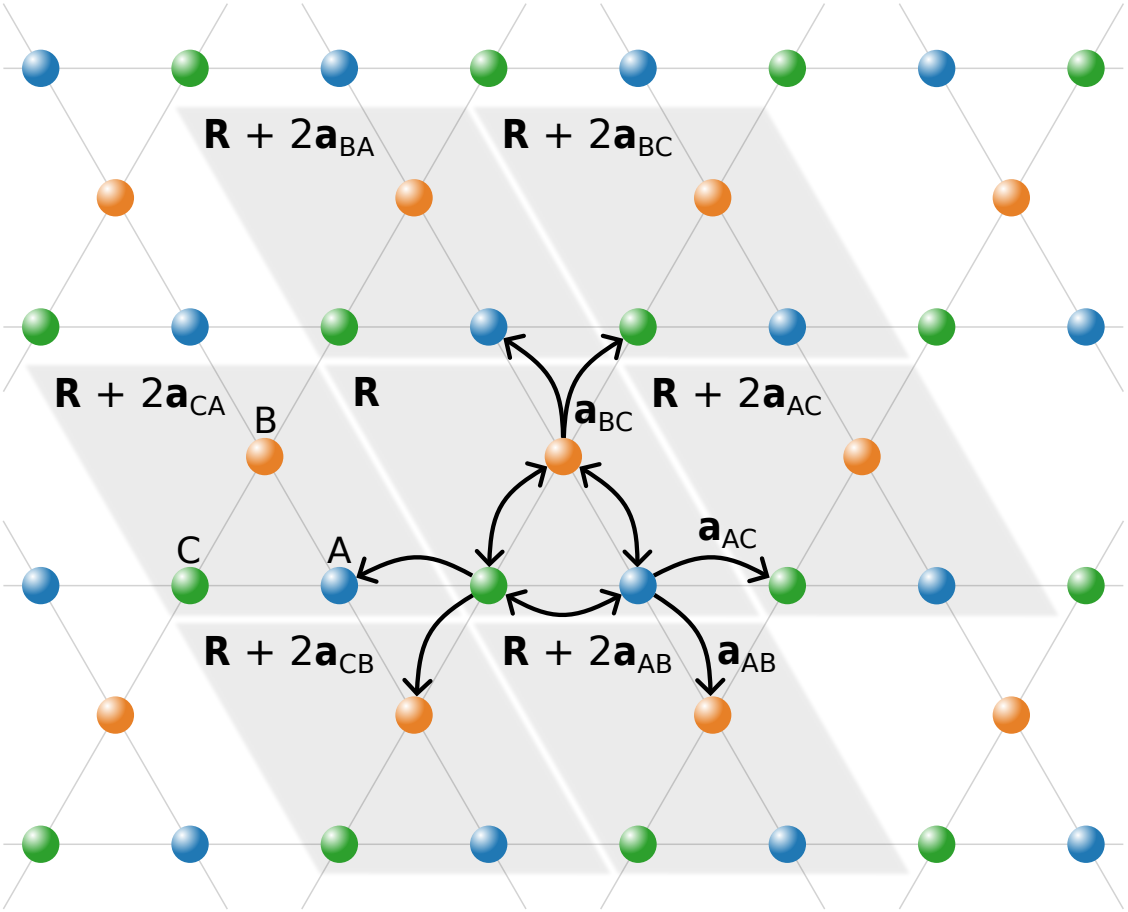

Figure 3.2: The naming convention adopted for the unit cells referred to in equation (3.4). The nearest neighbor bonds for the three atoms in the unit cell denoted by $\mathbf{R}$ are illustrated. Furthermore, the grey areas show the different unit cells.

case a d_{z^2}-orbital per site, since an s/d_{z^2}-orbital does not have any preferred direction in the plane of the lattice. This is motivated by DFT calculations, presented in Chapter 2, which show that the energy band with a van Hove singularity (vHs) closest to the Fermi energy (at the M-point) corresponds to vanadium-d_{z^2} orbitals [19], although other d-orbitals also contribute. The kinetic part of the Hamiltonian given by the TB model is then [26]

$$\mathcal{H}_{\text{TB}} = -t \sum_{\mathbf{R},s,\bar{s},\sigma} [c^{\dagger}_{\bar{s},\mathbf{R},\sigma} c_{s,\mathbf{R},\sigma} + c^{\dagger}_{\bar{s},\mathbf{R}+2\mathbf{a}_{s\bar{s}},\sigma} c_{s,\mathbf{R},\sigma}] - \mu \sum_{\mathbf{R},s,\sigma} c^{\dagger}_{s,\mathbf{R},\sigma} c_{s,\mathbf{R},\sigma} \,, \tag{3.4}$$

where the fermionic operator $c^{\dagger}_{s,\mathbf{R},\sigma}$ ($c_{s,\mathbf{R},\sigma}$) denotes the creation (annihilation) of an electron with spin $\sigma \in \{\uparrow,\downarrow\}$, located at site $s \in \{A,B,C\}$ in the unit cell denoted by $\mathbf{R}$. Furthermore, $\bar{s} \in \{A,B,C\} \setminus s$. The first and second terms describe intra- and inter-unit cell hoppings, respectively, and the third term accounts for the filling of electrons in the system, where μ is the chemical potential. With this notation we have introduced a quantum number s to account for the degrees of freedom within a unit cell, while the quantum number $\mathbf{R}$ is only sensitive to inter-unit cell degrees of freedom. We have defined the vectors $\mathbf{a}_{AC} \equiv \mathbf{a}_1$, $\mathbf{a}_{BC} \equiv \mathbf{a}_2$ and $\mathbf{a}_{AB} \equiv -\mathbf{a}_3$ to write the Hamiltonian in a compact form. The nearest neighbors for the three atomic sites in unit cell $\mathbf{R}$ are illustrated in Figure 3.2.

A Fourier transformation by $c_{s,\mathbf{R},\sigma} = \frac{1}{N} \sum_{\mathbf{k}\in BZ} e^{i\mathbf{k}\cdot\mathbf{r}} c_{s,\mathbf{k},\sigma}$, where N is the number of unit cells,

or, equivalently, the number of points in the Brillouin zone (BZ), leads to

$$\mathcal{H}_{\mathrm{TB}} = \sum_{\mathbf{k}\in BZ,\sigma} \left(c^{\dagger}_{A,\mathbf{k},\sigma}\ c^{\dagger}_{B,\mathbf{k},\sigma}\ c^{\dagger}_{C,\mathbf{k},\sigma}\right) H_{\mathrm{TB}}(\mathbf{k}) \left(c_{A,\mathbf{k},\sigma}\ c_{B,\mathbf{k},\sigma}\ c_{C,\mathbf{k},\sigma}\right)^{T} , \tag{3.5}$$

with the matrix $H_{\mathrm{TB}}(\mathbf{k})$ written in sublattice and momentum space

$$H_{\mathrm{TB}}(\mathbf{k}) = \begin{pmatrix} -\mu & -2t\cos k_3 & -2t\cos k_1 \\ -2t\cos k_3 & -\mu & -2t\cos k_2 \\ -2t\cos k_1 & -2t\cos k_2 & -\mu \end{pmatrix} , \tag{3.6}$$

where $k_n \equiv \mathbf{k}\cdot\mathbf{a}_n$. It is possible to choose a different gauge (equivalently, to make a different Fourier transform) in which the Hamiltonian is periodic in momentum space, such that $\tilde{H}_{\mathrm{TB}}(\mathbf{k}) = \tilde{H}_{\mathrm{TB}}(\mathbf{k}+\mathbf{Q})$, where $\mathbf{Q} = n\mathbf{g}_1 + m\mathbf{g}_2$ with $n, m \in \mathbb{Z}$. We determine a unitary transformation such that $\tilde{H}_{\mathrm{TB}}(\mathbf{k}) = UH_{\mathrm{TB}}(\mathbf{k})U^{\dagger}$. This momentum dependent unitary transformation is given by

$$U(\mathbf{k}) = \begin{pmatrix} e^{-ik_1} & 0 & 0 \\ 0 & e^{-ik_2} & 0 \\ 0 & 0 & 1 \end{pmatrix} , \tag{3.7}$$

which results in

$$\tilde{H}_{\mathrm{TB}}(\mathbf{k}) = \begin{pmatrix} -\mu & -t(1+e^{2ik_3}) & -t(1+e^{-2ik_1}) \\ -t(1+e^{-2ik_3}) & -\mu & -t(1+e^{-2ik_2}) \\ -t(1+e^{2ik_1}) & -t(1+e^{2ik_2}) & -\mu \end{pmatrix} . \tag{3.8}$$

Diagonalization of the 3×3 matrix gives the three eigenvalues

$$\xi_3(\mathbf{k}) = 2t - \mu\,, \tag{3.9}$$

$$\xi_2(\mathbf{k}) = t\left(-1 + \sqrt{2\left[\cos(2k_1)+\cos(2k_2)+\cos(2k_3)\right]+3}\right) - \mu\,, \tag{3.10}$$

$$\xi_1(\mathbf{k}) = t\left(-1 - \sqrt{2\left[\cos(2k_1)+\cos(2k_2)+\cos(2k_3)\right]+3}\right) - \mu\,, \tag{3.11}$$

where ξ_3 denotes the flat, upper energy band and ξ_2 and ξ_1 the middle and lower energy bands, respectively. The bands are plotted as a function of momentum, for $\mu = 0$, in Figure 3.3(a). The momentum on the x-axis traces out a path in the Brillouin zone starting from the high-symmetry point $\mathbf{\Gamma} = \begin{pmatrix}0 & 0\end{pmatrix}^T$, going to the center of an edge of the BZ given by $\mathbf{M}_1 = \left(\pi\ \frac{\pi}{\sqrt{3}}\right)^T = \frac{1}{2}\mathbf{g}_1$, where $\mathbf{g}_1$ is the reciprocal lattice vector defined in equation (3.3), then to a corner of the BZ given by $\mathbf{K} = \left(\frac{4\pi}{3}\ 0\right)^T$ and finally back to $\mathbf{\Gamma}$ (see the inset in Figure 3.3(a)). The energy bands have a few special features: the middle and lower bands, ξ_2 and ξ_1, have a van Hove singularity at the M-point, and at the K-point there is a Dirac cone. Van Hove points are saddle points in the band structure giving rise to singularities in the density of states as seen in Figure 3.3(b). For a chemical potential of $\mu = 0$ the states below the upper van Hove singularity will be filled. Around the K-point the bands have a conical shape and they meet at a Dirac point. Furthermore, the upper band is completely dispersionless throughout the entire Brillouin zone.

The density of states describes the number of electronic states the system possesses within a small energy window. The local density of states (LDOS), $\rho_{ss'}(\mathbf{R},\omega)$, is obtained by taking the imaginary part of the retarded Green function in real space basis

$$\rho_{ss'}(\mathbf{R},\omega) = -\frac{1}{\pi}\mathrm{Im}(G^{R}_{ss'}(\mathbf{R},\omega))\,. \tag{3.12}$$

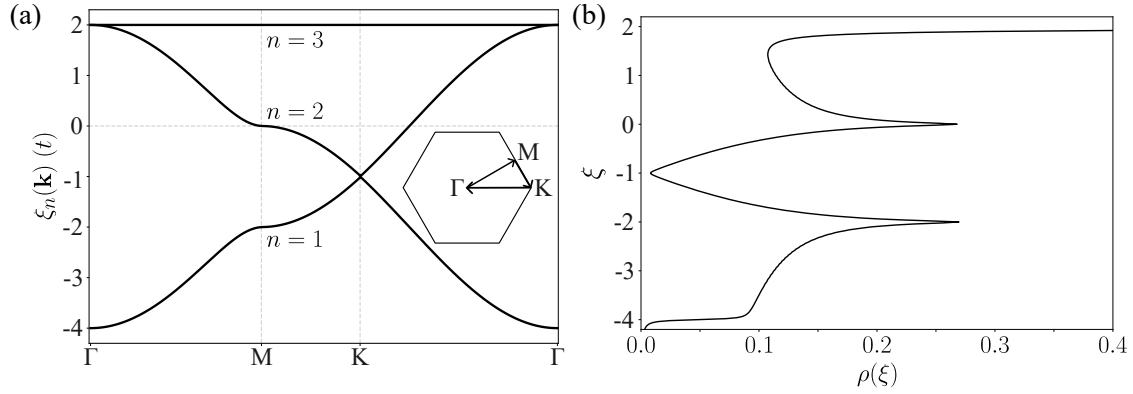

Figure 3.3: (a) Tight-binding energy bands $\xi_n(\mathbf{k})$ plotted along the path in the BZ shown in the inset. There is an upper flat band and two lower dispersive bands, both of which feature a van Hove singularity at the M-point in addition to meeting at a Dirac point at K. (b) The normal state DOS diverges at the flat band energy and at the two van Hove singularities.

In the following, we will omit the superscript R (for retarded) in the Green function. The Green function in momentum and energy basis is easily computed since the Hamiltonian is diagonal in this basis

$$G(\mathbf{k},\omega) = ((\omega + i\eta)\mathbb{1} - H^B_{\mathrm{TB}}(\mathbf{k}))^{-1} = \begin{pmatrix} \frac{1}{\omega+i\eta-\xi_3(\mathbf{k})} & 0 & 0 \\ 0 & \frac{1}{\omega+i\eta-\xi_2(\mathbf{k})} & 0 \\ 0 & 0 & \frac{1}{\omega+i\eta-\xi_1(\mathbf{k})} \end{pmatrix}, \tag{3.13}$$

where η is an infinitesimal positive number included in the transformation from time to frequency for convergence and $H^B_{\mathrm{TB}}(\mathbf{k})$ is obtained from diagonalizing $H_{\mathrm{TB}}(\mathbf{k})$, as detailed in the next section.

3.2 Sublattice interference

In the following we show that the upper van Hove singularity has a special feature known as sublattice interference. Sublattice interference is the property that electronic wave packages with certain momenta only have weight at one of the three sublattice sites. To illustrate this feature we make a unitary matrix transformation of the tight-binding matrix $H_{\mathrm{TB}}(\mathbf{k})$ from sublattice space into band space $H^B_{\mathrm{TB}}(\mathbf{k}) = UH_{\mathrm{TB}}(\mathbf{k})U^{-1}$, where $H^B_{\mathrm{TB}}(\mathbf{k})$ is a matrix containing the eigenenergies on the diagonal. Thus by insertion of $U^{-1}U = \mathbb{1}$ the Hamiltonian can be rewritten as

$$\mathcal{H}_{\mathrm{TB}} = \sum_{\mathbf{k}\in BZ,\sigma} c^\dagger_{\mathbf{k},\sigma} U^{-1} H^B_{\mathrm{TB}}(\mathbf{k}) U c_{\mathbf{k},\sigma}\,, \tag{3.14}$$

where we have defined $c^\dagger_{\mathbf{k},\sigma} = \left(c^\dagger_{A,\mathbf{k},\sigma}\ c^\dagger_{B,\mathbf{k},\sigma}\ c^\dagger_{C,\mathbf{k},\sigma}\right)$. The Hamiltonian is thus diagonal in the operators given by $\gamma_{\mathbf{k},\sigma} = Uc_{\mathbf{k},\sigma}$, and the relation between the c- and γ-operators can be written $c_{s,\mathbf{k},\sigma} = \sum_{n=1}^{3} u^*_{sn}(\mathbf{k})\gamma_{n,\mathbf{k},\sigma}$, where the sum is over the band index n. The unitary matrix that diagonalizes $H_{\mathrm{TB}}(\mathbf{k})$ consists of the eigenvectors of $H_{\mathrm{TB}}(\mathbf{k})$. In Figure 3.4(a) the absolute square of the three entries of the eigenvector corresponding to the middle band $n = 2$, $|u_{A2}(\mathbf{k})|^2$, $|u_{B2}(\mathbf{k})|^2$ and $|u_{C2}(\mathbf{k})|^2$, are plotted along the Fermi surface corresponding to $\mu = 0$ (electron filling at the upper van Hove singularity, $n_{\mathrm{el}} = 5/12$ [23]). The weight $|u_{A2}(\mathbf{k})|^2$ provides information on how much of the wavefunction occupies sublattice site A relative to sites B and C. The weights periodically alternate around the Fermi surface and the wavefunction is found to be localized at

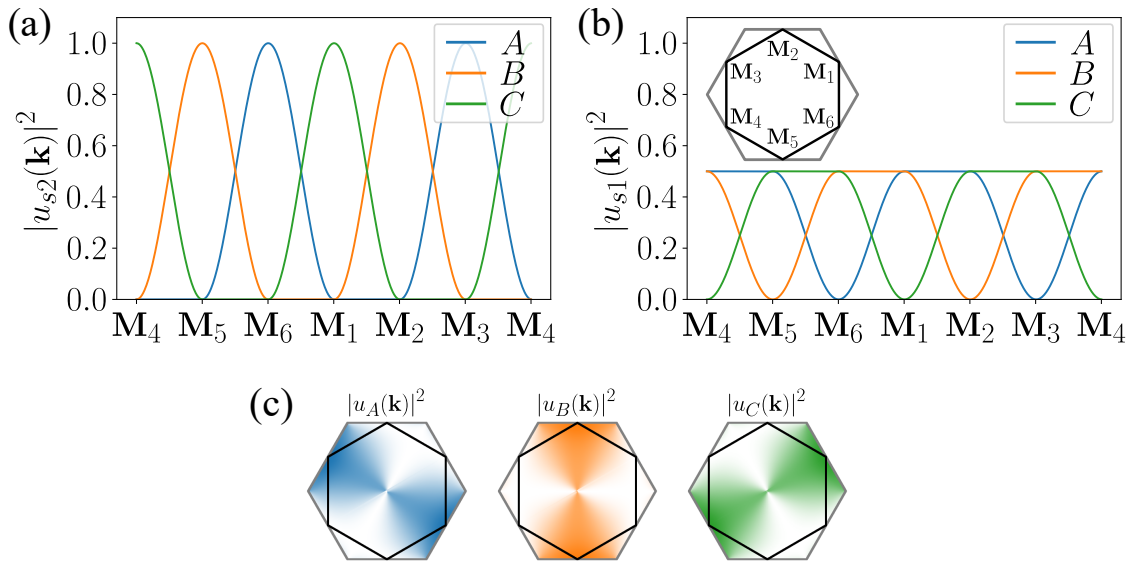

Figure 3.4: (a) The sublattice weights $|u_{s2}(\mathbf{k})|^2$ at the upper van Hove singularity, corresponding to $\mu = 0$ and a hexagonal Fermi surface as illustrated in the inset of (b). At the M-points the weight is entirely localized on a specific sublattice. (b) The sublattice weights at the lower van Hove singularity, $\mu = -2$. In this case the weight is distributed on at least two of the three sublattice sites. (c) The absolute square of the entries of the eigenvector corresponding to the middle band plotted on the first BZ (full grey line) showing the non-zero weight on only certain portions of the Fermi surface (full black line).

one type of sublattice site for momenta corresponding to M-points. The M-points are given by

$$\mathbf{M}_1 \equiv \left(\pi \ \tfrac{\pi}{\sqrt{3}}\right)^T, \quad \mathbf{M}_2 \equiv \left(0 \ \tfrac{2\pi}{\sqrt{3}}\right)^T, \quad \mathbf{M}_3 \equiv \left(-\pi \ \tfrac{\pi}{\sqrt{3}}\right)^T, \tag{3.15}$$

and $\mathbf{M_4} \equiv -\mathbf{M}_1$, $\mathbf{M}_5 \equiv -\mathbf{M}_2$ and $\mathbf{M}_6 \equiv -\mathbf{M}_3$. For comparison, the weights $|u_{s3}(\mathbf{k})|^2$ are also plotted along the Fermi surface for a chemical potential of $\mu = -2$, which corresponds to filling at the lower van Hove singularity ($n_{\text{el}} = 3/12$ [23]), see Figure 3.4(b). In this case the weight is distributed on at least two of the three sublattice sites. This difference in the two van Hove singularities (vHs) has led to the upper one being named a "pure"-type vHs while the lower one is called a "mixed"-type vHs. The "pure"- and "mixed"-type features are not only present in the kagome tight-binding model but are also revealed by ARPES experiments and DFT calculations on the AV_3Sb_5 compounds [27]. Sublattice interference has been explored in the literature ([28], [29]) as it could have an impact on the type of possible Fermi surface instabilities. The work presented in this thesis is not dependent on the more fine-tuned case of sublattice interference but rather on a general property of the kagome lattice, namely that each sublattice site s, and also the entry $u_{sn}(\mathbf{k})$, has a lower symmetry than the lattice itself. The sublattice sites have a two-fold rather than six-fold rotational symmetry which is visible in the weight $|u_{s2}(\mathbf{k})|^2$ plotted on the BZ in Figure 3.4(c) in the case of the middle band.

Chapter 4

Superconductivity

"You know
Every now and then I think you might like to hear something from us
Nice and easy
But there's just one thing, you see
We never ever do nothin'
Nice and easy
We always do it nice and rough"

Tina Turner intro to Proud Mary

In this chapter we introduce the mean-field (or effective non-interacting) Hamiltonian used to describe superconductivity on the kagome lattice. Subsequently, we use techniques from group theory to classify the symmetry-allowed order parameters. The superconducting order parameter is related to the Cooper pair wavefunction, and it is a function which can in general be complex and depend on momentum $\mathbf{k}$. The symmetry-allowed order parameters will be classified according to what is called irreducible representations, which, for our purpose, can be understood as the basis functions in which we decompose the order parameter. The allowed basis functions, or irreducible representations, are dictated by the point group of the lattice. Simply put, the point group is a set of symmetry-operations which leave the lattice sites unchanged after the transformation.

Linguistically, different superconducting states can be categorized in multiple ways. The terms "conventional" and "unconventional" superconductivity are often used when referring to the microscopic mechanism driving the superconducting instability: if it is phonon-driven it is called conventional, and if it is driven by some other mechanism it is referred to as unconventional. Phonon-mediated superconductivity, described by the framework of BCS theory, gives rise to an isotropic order parameter. Unconventional pairing states, on the other hand, have a non-trivial momentum-dependence which can lead to additional spontaneous symmetry breaking at the superconducting phase transition. For example, a two-dimensional order parameter can result in the breaking of rotational or time-reversal symmetry. Time reversal symmetry is broken when the order parameter consists of two (or more) components where one of the components has a complex coefficient [30].

In many cases the mechanism responsible for the superconducting phase is not known, and consequently it is often the symmetry properties of the order parameter which are discussed in the literature. In what follows, we do not provide any microscopic mechanism for the superconducting

instability but rather use a symmetry-based phenomenological approach, and we only refer to the symmetry properties of the order parameter. We distinguish between order parameters which transform trivially or non-trivially under the symmetry operations of the point group of the kagome lattice. The first kind is referred to as trivial superconductivity, and the latter as non-trivial or unconventional. This categorization includes higher angular momentum (not only $l = 0$, i.e. s-wave) states in the trivial group, called A_1, although these are not "BCS states" in the sense that the BCS order parameter is constant in momentum.

4.1 The model

The applied model consists of a tight-binding model outlined in Section 3.1 along with a general interaction described by

$$H = \sum_{\mu\mu'\nu\nu'} V_{\mu\mu'\nu\nu'} c^\dagger_\mu c_{\mu'} c^\dagger_\nu c_{\nu'} \,, \tag{4.1}$$

where μ, μ', ν, ν' are general quantum numbers. In order to study a system with the given interaction, it is necessary to make simplifying assumptions. By assuming that the fluctuations of a given operator are small, we can put the interaction on Gaussian form by expanding the Hamiltonian to first order in the fluctuations. This introduces an effective background potential defined by the mean of a set of field operators, and hence we obtain a mean-field theory which can be solved exactly. By this we mean that it is possible to diagonalize the Hamiltonian, since it is quadratic in the electron operators. Since we are interested in studying superconductivity, we expand the Hamiltonian in the Cooper channel, where the expansion is performed in fluctuations of two creation or two annihilation operators [26]. Before continuing with the mean-field decoupling we introduce the BCS Hamiltonian. In BCS theory it is assumed that the superconducting condensate is formed by time-reversed partners, i.e. pairs of electrons with opposite momenta and spin. The BCS Hamiltonian takes the form

$$\mathcal{H}_{\text{BCS}} = \sum_{\mathbf{k},\sigma} \xi_{\mathbf{k}} c^\dagger_{\mathbf{k},\sigma} c_{\mathbf{k},\sigma} + \sum_{\mathbf{k},\mathbf{k}'} V_{\mathbf{k}\mathbf{k}'} c^\dagger_{\mathbf{k},\uparrow} c^\dagger_{-\mathbf{k},\downarrow} c_{-\mathbf{k}',\downarrow} c_{\mathbf{k}',\uparrow} \,. \tag{4.2}$$

In BCS theory it is assumed that the interaction strength due to electron-phonon coupling, $V_{\mathbf{k}\mathbf{k}'}$, becomes attractive for electrons close to the Fermi energy, i.e. $V_{\mathbf{k}\mathbf{k}'} = -V < 0$ for states with energies $|\xi_{\mathbf{k}}|, |\xi_{\mathbf{k}'}| < \omega_D$ and zero otherwise. ω_D is the Debye frequency which sets an energy cut off for the electrons participating in the superconducting condensate [31]. The assumption that the pairing interaction is constant results in the mean-field order parameter Δ having no momentum dependence. In our model we allow for the interaction, and thus the order parameter, to be momentum dependent. The interaction in the case of a kagome lattice takes the following form, where we have introduced sublattice indices s_1, s_2, s_3, s_4:

$$\mathcal{H}_{\text{int}} = \frac{1}{N^2} \sum_{\mathbf{k},\mathbf{k}',s_1,s_2,s_3,s_4} V^{s_1,s_2,s_3,s_4}_{\mathbf{k},\mathbf{k}'} c^\dagger_{s_1,\mathbf{k},\uparrow} c^\dagger_{s_2,-\mathbf{k},\downarrow} c_{s_3,-\mathbf{k}',\downarrow} c_{s_4,\mathbf{k}',\uparrow} \,. \tag{4.3}$$

The mean-field decoupling of this interaction is shown in detail in Appendix F. Here, we sketch the approach more generally. From equation (4.1), we define the fluctuation of the operator $A^\dagger_{\mu\nu} \equiv c^\dagger_\mu c^\dagger_\nu$,

$$\delta A^\dagger_{\mu\nu} = A^\dagger_{\mu\nu} - \langle A^\dagger_{\mu\nu} \rangle \,, \tag{4.4}$$

and similarly for $A_{\mu\nu} \equiv c_\mu c_\nu$. Rearranging the operators in the interaction yields $V_{\mu\mu'\nu\nu'} c^\dagger_\mu (\delta_{\mu'\nu} c_{\nu'} + c^\dagger_\nu c_{\nu'} c_{\mu'})$. In the following, μ' and ν will correspond to quantum numbers with different spin such

that $\delta_{\mu'\nu} = 0$. An expansion of the interaction to first order in the fluctuations of $A^\dagger_{\mu\nu}$ and $A_{\nu'\mu'}$ results in

$$\sum_{\mu\mu'\nu\nu'} V_{\mu\mu'\nu\nu'} A^\dagger_{\mu\nu} A_{\nu'\mu'} \approx \sum_{\mu\nu} \Delta_{\mu\nu} A^\dagger_{\mu\nu} + \sum_{\mu'\nu'} \Delta^\dagger_{\mu'\nu'} A_{\nu'\mu'} - \sum_{\mu\mu'\nu\nu'} V_{\mu\mu'\nu\nu'} \langle A^\dagger_{\mu\nu} \rangle \langle A_{\nu'\mu'} \rangle \,, \tag{4.5}$$

where we defined the complex mean-fields

$$\Delta_{\mu\nu} \equiv \sum_{\mu'\nu'} V_{\mu\mu'\nu\nu'} \langle A_{\nu'\mu'} \rangle \,, \quad \Delta^\dagger_{\mu'\nu'} \equiv \sum_{\mu\nu} V_{\mu\mu'\nu\nu'} \langle A^\dagger_{\mu\nu} \rangle \,, \tag{4.6}$$

and where the last term will contribute to an offset in the energy. Following the same approach, a mean-field decoupling of the interaction in equation 4.3 together with the TB model leads to the Bogoliubov-de Gennes (BdG) Hamiltonian

$$\mathcal{H}_{\mathrm{BdG}} = \sum_{\mathbf{k}\in \mathrm{BZ},\sigma} c^\dagger_{\mathbf{k},\sigma} H_{\mathrm{TB}}(\mathbf{k}) c_{\mathbf{k},\sigma} - \sum_{\mathbf{k}\in \mathrm{BZ}} (c^\dagger_{\mathbf{k},\uparrow} \Delta_{\mathbf{k}} c^\dagger_{-\mathbf{k},\downarrow} + c_{-\mathbf{k},\downarrow} \Delta^\dagger_{\mathbf{k}} c_{\mathbf{k},\uparrow}) \,. \tag{4.7}$$

By introducing the so-called Nambu spinor $\Psi^\dagger_{\mathbf{k}} \equiv \begin{pmatrix} c^\dagger_{\mathbf{k},\uparrow} & c_{-\mathbf{k},\downarrow} \end{pmatrix}$, the Hamiltonian is rewritten on the form

$$\begin{aligned} \mathcal{H}_{\mathrm{BdG}} &= \sum_{\mathbf{k}\in \mathrm{BZ}} \begin{pmatrix} c^\dagger_{\mathbf{k},\uparrow} & c_{-\mathbf{k},\downarrow} \end{pmatrix} \begin{pmatrix} H_{\mathrm{TB}}(\mathbf{k}) & -\Delta_{\mathbf{k}} \\ -\Delta^\dagger_{\mathbf{k}} & -H_{\mathrm{TB}}(\mathbf{k}) \end{pmatrix} \begin{pmatrix} c_{\mathbf{k},\uparrow} \\ c^\dagger_{-\mathbf{k},\downarrow} \end{pmatrix} \\ &= \sum_{\mathbf{k}\in \mathrm{BZ}} \Psi^\dagger_{\mathbf{k}} \begin{pmatrix} H_{\mathrm{TB}}(\mathbf{k}) & -\Delta_{\mathbf{k}} \\ -\Delta^\dagger_{\mathbf{k}} & -H_{\mathrm{TB}}(\mathbf{k}) \end{pmatrix} \Psi_{\mathbf{k}} = \sum_{\mathbf{k}\in \mathrm{BZ}} \Psi^\dagger_{\mathbf{k}} H_{\mathrm{BdG}}(\mathbf{k}) \Psi_{\mathbf{k}} \,, \end{aligned} \tag{4.8}$$

where both $H_{\mathrm{TB}}(\mathbf{k})$ and $\Delta_{\mathbf{k}}$ are 3×3 matrices in sublattice space, which are momentum dependent. We can now define the Nambu Green function

$$\begin{aligned} \mathcal{G}^{(0)}(\mathbf{k},\tau) &\equiv -\langle T_\tau \Psi_{\mathbf{k}}(\tau) \Psi^\dagger_{\mathbf{k}}(0) \rangle = -\langle T_\tau \begin{pmatrix} c_{\mathbf{k},\uparrow}(\tau) \\ c^\dagger_{-\mathbf{k},\downarrow}(\tau) \end{pmatrix} \otimes \begin{pmatrix} c^\dagger_{\mathbf{k},\uparrow}(0) & c_{-\mathbf{k},\downarrow}(0) \end{pmatrix} \rangle \\ &= -\begin{pmatrix} \langle T_\tau c_{\mathbf{k},\uparrow}(\tau) c^\dagger_{\mathbf{k},\uparrow}(0) \rangle & \langle T_\tau c_{\mathbf{k},\uparrow}(\tau) c_{-\mathbf{k},\downarrow}(0) \rangle \\ \langle T_\tau c^\dagger_{-\mathbf{k},\downarrow}(\tau) c^\dagger_{\mathbf{k},\uparrow}(0) \rangle & \langle T_\tau c^\dagger_{-\mathbf{k},\downarrow}(\tau) c_{-\mathbf{k},\downarrow}(0) \rangle \end{pmatrix} \,, \end{aligned} \tag{4.9}$$

and introduce the so-called normal and anomalous Green functions. The normal Green function is defined by

$$G^{(0)}(\mathbf{k},\tau) \equiv -\langle T_\tau c_{\mathbf{k},\uparrow}(\tau) c^\dagger_{\mathbf{k},\uparrow}(0) \rangle \,, \tag{4.10}$$

while the anomalous (anomalous because it couples different spin) Green function is

$$F^{(0)}(\mathbf{k},\tau) \equiv -\langle T_\tau c_{\mathbf{k},\uparrow}(\tau) c_{-\mathbf{k},\downarrow}(0) \rangle \,. \tag{4.11}$$

The normal and anomalous Green functions, $G^{(0)}(\mathbf{k},\tau)$ and $F^{(0)}(\mathbf{k},\tau)$, are 3×3 matrices and thus the Nambu Green function, $\mathcal{G}^{(0)}(\mathbf{k},\tau)$, is a 6×6 matrix. In Chapter 5 we return to the Nambu Green function, which will be used to calculate the density of states, but the remainder of this chapter centers on the derivation of expressions for the symmetry-allowed superconducting order parameters $\Delta_{\mathbf{k}}$ on the kagome lattice.

D_6	E	$2C_6$	$2C_3$	C_2	$3C_2'$	$3C_2''$
A_1	1	1	1	1	1	1
A_2	1	1	1	1	-1	-1
B_1	1	-1	1	-1	1	-1
B_2	1	-1	1	-1	-1	1
E_1	2	1	-1	-2	0	0
E_2	2	-1	-1	2	0	0

Table 4.1: The character table of the D_6 point group [32].

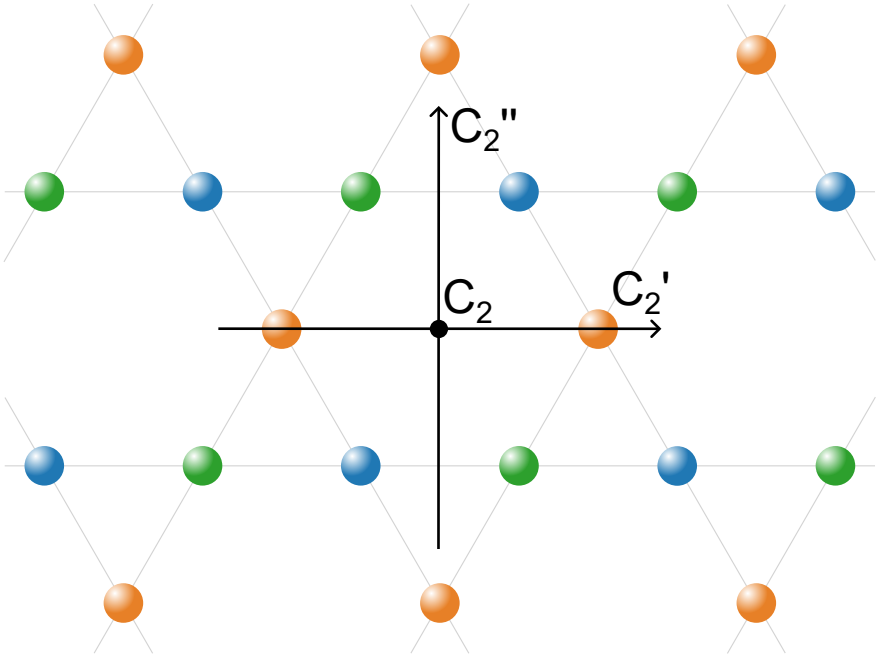

Figure 4.1: Illustration of the rotation axes denoted C_2, C_2' and C_2'' relative to the kagome lattice.

4.2 Lattice harmonics

To classify the allowed superconducting states on the kagome lattice we make use of techniques from group theory. The central point of the hexagons in the kagome lattice exhibits D_6 point group symmetry. In Table 4.1 the character table of the D_6 point group is presented [32].

The point group D_6 contains 12 elements. The set denoted by E contains the identity, $2C_6$ contains rotations by $\pm\frac{\pi}{3}$ around the principal axis (the axis perpendicular to the plane of the lattice), $2C_3$ contains rotations by $\pm\frac{2\pi}{3}$ around the principal axis, and C_2 denotes a rotation by π around the principal axis. The $3C_2'$ and $3C_2''$ sets each contain three elements which are rotations by π around the in-plane axes in each set. By convention, the $3C_2'$ set has the x-axis as a member, while the y-axis is a member of the $3C_2''$ set. There exists a degree of freedom in the orientation of the lattice with respect to the rotation axes. We align the hexagon according to the orientation shown in Figure 4.1, but an option that is equally valid would be to rotate the lattice by $\frac{\pi}{2}$ around C_2.

The D_6 point group has six irreducible representations (irreps): four of the irreps (A_1, A_2, B_1

and B_2) are one-dimensional and two of the irreps (E_1 and E_2) are two-dimensional. The A_1 irrep is referred to as trivial because it remains unchanged under a transformation by any of the elements in D_6. If no crystal symmetry is broken, the Hamiltonian should transform as the A_1 irrep, since the energy should be independent of transformations belonging to the point group of the lattice. To illustrate the irreducible representations, we use a set of basis functions $f_{\mathbf{a}}(\mathbf{k}) = e^{i\mathbf{k}\cdot\mathbf{a}}$ to generate one-dimensional functions $f^{\Gamma}_{\mathbf{a}}(\mathbf{k})_{\mu\nu}$ that transform like one of the irreducible representations Γ of D_6. Expressed alternatively, we project $e^{i\mathbf{k}\cdot\mathbf{a}}$ onto the irreps of D_6. The functions are constructed by

$$f^{\Gamma}_{\mathbf{a}}(\mathbf{k})_{\mu\nu} = \frac{d^{\Gamma}}{N_{\mathcal{G}}} \sum_{g\in\mathcal{G}} D^{\Gamma}(g)^{*}_{\mu\nu} e^{i\mathbf{k}\cdot(D(g)\mathbf{a})}\,, \tag{4.12}$$

where g denotes an element in the point group $\mathcal{G}$, $N_{\mathcal{G}}$ is the number of elements in $\mathcal{G}$ ($N_{\mathcal{G}} = 12$ for the D_6 point group), Γ is one of the irreducible representations and d^{Γ} is the dimension of the Γ irrep. The above equation is based on projecting $f_{\mathbf{a}}(\mathbf{k})$ onto $\Pi^{\Gamma}_{\mu\nu} = \frac{d^{\Gamma}}{N_{\mathcal{G}}} \sum_{g\in\mathcal{G}} D^{\Gamma}(g)^{*}_{\mu\nu} P_R$, where P_R is an operator working on functions such that $P_{D(g)} f(D(g)\mathbf{k}) = f(\mathbf{k})$ [33]. In the case of a one-dimensional irrep, $D^{\Gamma}(g)^{*}_{\mu\nu} = \chi^{\Gamma}(g)$ is the character of the element g in the Γ irrep, and in the case of a two-dimensional irrep, $D^{\Gamma}(g)^{*}_{\mu\nu}$ is the (μ,ν) entry of the two-dimensional matrix representation of the element g written in the Γ irrep. $D(g)$ is a two-dimensional matrix representation of the element g written in one of the 2D irreps, and we arbitrarily choose the E_1 irrep. The matrix representations $D(g)$ employed in equation (4.12) are provided in Appendix A. In the case of $\Gamma = A_1$, equation (4.12) becomes

$$f^{A_1}_{\mathbf{a}}(\mathbf{k}) = \frac{1}{12} \sum_{g\in D_6} \chi^{A_1}(g) e^{i\mathbf{k}\cdot(D(g)\mathbf{a})}\,, \tag{4.13}$$

where $\chi^{A_1}(g)$ is the character of the element g in the A_1 irrep. The functions $f^{\Gamma}_{\mathbf{a}}(\mathbf{k})_{\mu\nu}$ are called lattice harmonics, and the lattice vector $\mathbf{a}$ indicates the extent of the interaction/pairing necessary to generate a certain harmonic. The length of $\mathbf{a}$ then indicates the order: the shorter the vector, the lower the order. This formalism does not account for the sublattice degree of freedom, which will be included in Section 4.3. For the two-dimensional irreps we set $\nu = 1$ (selecting the first column of $D^{\Gamma}(g)$) and then calculate $f^{\Gamma}_{\mathbf{a}}(\mathbf{k})_{\mu 1}$ where μ denotes the row of the matrix $D^{\Gamma}(g)$. $f^{\Gamma}_{\mathbf{a}}(\mathbf{k})_{\mu 1}$ with $\mu = 1$ ($\mu = 2$) then transforms as the first (second) component of Γ, which we denote with subscripts Γ_{11} (Γ_{21}). The lowest-order, non-constant lattice harmonics $f^{A_1}_{\mathbf{a}}(\mathbf{k})$ are illustrated in Figure 4.2 for the A_1 irrep and in Appendix E for the remaining irreps. From Figure 4.2 it is evident that the function $f^{A_1}_{\mathbf{a}}(\mathbf{k})$ does not change sign under any of the transformations in the D_6 point group.

At lowest order, i.e. for $\mathbf{a} = \mathbf{0}$ (not shown in Figure 4.2), the A_1 irrep is constant in momentum and corresponds to an s-wave order parameter. Before proceeding, a small note on terminology is in place, since this point can be confusing for first-time learners: Referring to an order parameter as s-wave when it transforms as the A_1 irrep (as $p+ip$ when it transforms as the complex combination of the components of the 2D E_1 irrep: $(E_1)_{11}+i(E_1)_{21}$, as $d+id$ when it transforms as $(E_2)_{11}+i(E_2)_{21}$ or as f-wave when it transforms as the B_1 irrep) is common terminology in the literature, although naming according to spherical harmonics can be misleading since it is only to lowest order that the orbital component has angular momentum $l = 0$ (s) ($l = 1$ (p), $l = 2$ (d) or $l = 3$ (f)). Nevertheless, in what follows we will use the two naming conventions interchangeably. The subscript in, for example, $d_{x^2-y^2}$ denotes the momentum dependence of the order parameter, in the sense that a function transforming as the first component of the E_2 irrep, $(E_2)_{11}$, depends on $k_x^2 - k_y^2$. As is evident from the lattice harmonics, some order parameters change sign as a function of momentum. It is therefore possible to have an order parameter which changes sign and crosses zero somewhere

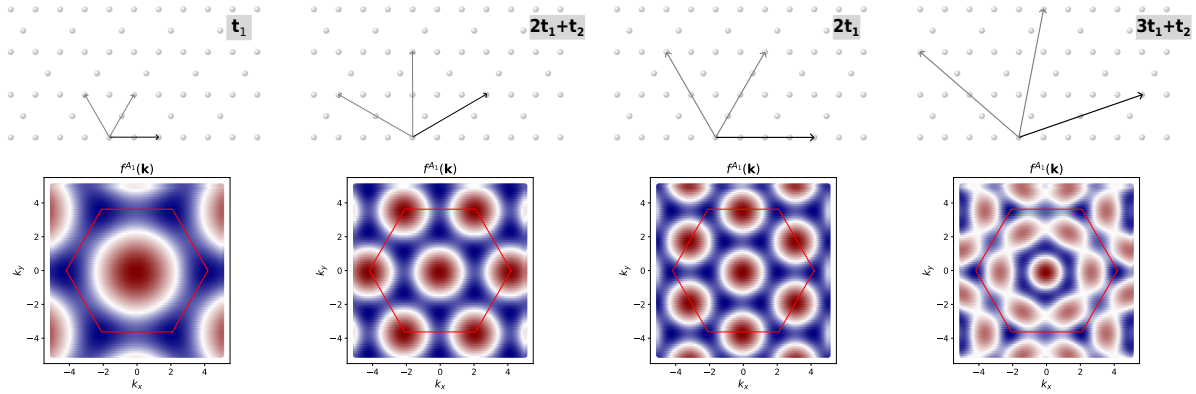

Figure 4.2: $f^{A_1}_{\mathbf{a}}(\mathbf{k})$ plotted for four different vectors, $\mathbf{a} = \mathbf{t}_1, 2\mathbf{t}_1 + \mathbf{t}_2, 2\mathbf{t}_1, 3\mathbf{t}_1 + \mathbf{t}_2$, yielding the four lowest order, non-constant lattice harmonics transforming as the A_1 irrep. There is also a contribution from $f^{A_1}_{\mathbf{a}=\mathbf{0}}(\mathbf{k})$ which is non-zero but constant over the Brillouin zone. The hexagonal Brillouin zone is superimposed in red.

on the Fermi surface, and consequently the energy gap closes at this location. An order parameter with crossings through zero is called nodal. Whether the order parameter has nodes, depends not only on the irrep it transforms as but also on the fermiology, i.e. the shape and size of the Fermi surface. The Fermi surface nodes can have different topology, i.e. either be nodal points or nodal lines. Experimentally, specific heat measurements can differentiate between different nodal topology as the low temperature dependence of the specific heat will be either $\propto T^2$ or $\propto T^3$, depending on whether the order parameter has nodal lines or nodal points, respectively [4]. As an example, the A_1 and E_2 irreps to lowest order are illustrated for the case of a circular Fermi surface in Figure 4.3. We see that while the s-wave order parameter is completely isotropic, the $d_{x^2-y^2}$ ($(E_2)_{11}$) and d_{xy} ($(E_2)_{21}$) order parameters are anisotropic and are equal to zero at four points on the Fermi surface.

The existence of nodes leaves an experimental fingerprint on the local density of states which can be measured through scanning tunneling microscopy. If there are no nodes on the Fermi surface it means that for every Fermi momentum there will always be a full gap and thus no states to occupy within the gap. This will yield a full or "U-type" gap, for which there is a finite energy range where the LDOS is zero. On the contrary, if there are nodes on the Fermi surface the gap becomes smaller and smaller close to the node until it closes and becomes zero at a certain nodal point. This will result in a soft or "V-type" gap. In terms of excitations, a finite amount of energy is always needed to create an excitation when there are no nodes, whereas it will cost an exceedingly small amount of energy to create excitations close to a node. The time-reversal symmetry breaking combinations $p_x + ip_y$ and $d_{x^2-y^2} + id_{xy}$ do not have any nodes on the Fermi surface, although the individual components do. For example, p_x and p_y individually have nodal lines (p_x along $k_x = 0$ and p_y along $k_y = 0$), but since these lines are not parallel and since the contribution from p_x cannot cancel with the contribution from p_y due to the imaginary combination, the $p_x + ip_y$ gap function will not have any nodes. Thus, the time-reversal symmetry breaking gap functions will result in a U-type gap. This will be shown in Chapter 5 where the local density of states is plotted.

4.3 Classification of superconducting states

In this section we present a systematic classification of the possible pairing symmetries on the kagome lattice. To obtain the best understanding of the pairings, our starting point will be the real space order parameter which we expand in terms of a range of interactions. Subsequently,

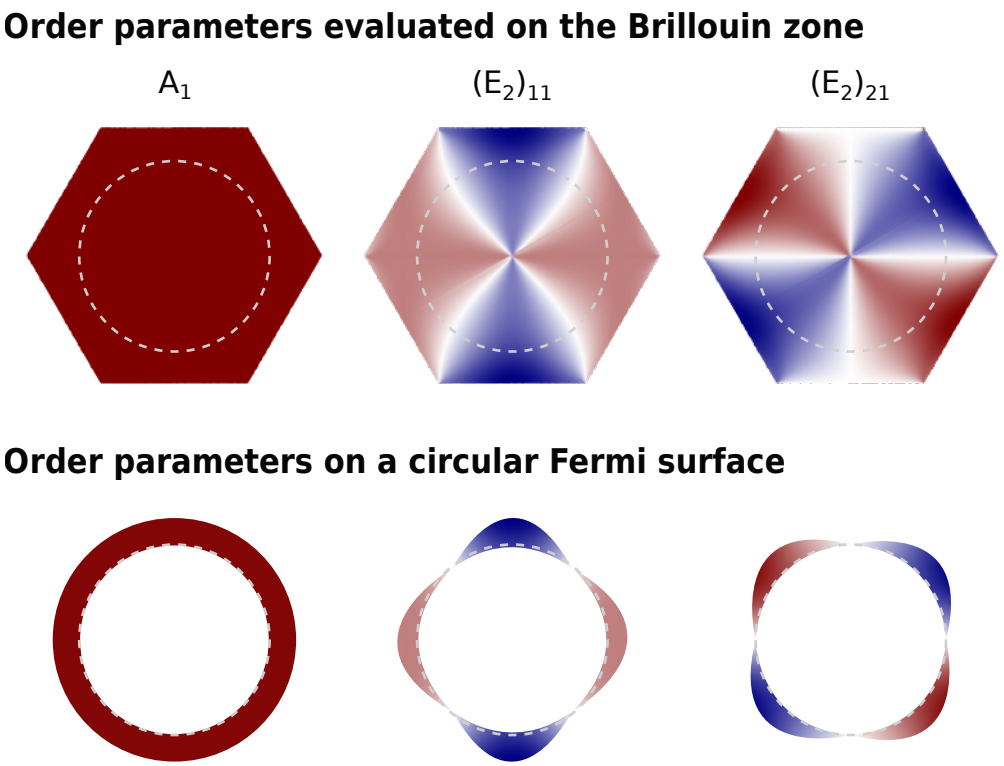

Figure 4.3: Top panel: Illustration of s-wave (left), $d_{x^2-y^2}$-wave (middle) and d_{xy}-wave (right) order parameters on the hexagonal Brillouin zone of the kagome lattice. The colour depicts the phase of the order parameter (red: +1, blue: -1). An example of a Fermi surface is imposed (grey, dashed). Bottom panel: The order parameter illustrated on the Fermi surface where the segment height represents the amplitude of the order parameter. The s-wave order parameter is isotropic in all directions, where, for example, the d_{xy}-wave order parameter is maximum (or minimum) along the diagonals and zero on the horizontal and vertical axes.

a Fourier transformation of the given expression yields the momentum dependence of the order parameter. The order parameter describes either singlet or triplet pairing and takes the general form

$$\Delta^{\Gamma}_{ss'}(\mathbf{k}) = \Delta_0 f^{\Gamma}_{\mathrm{OS}}(\mathbf{k}) + \Delta_1 f^{\Gamma}_{\mathrm{NN}}(\mathbf{k}) + \Delta_2 f^{\Gamma}_{\mathrm{NNN}}(\mathbf{k}) + \Delta_3 f^{\Gamma}_{3rd}(\mathbf{k})\,, \tag{4.14}$$

where $\Delta^{\Gamma}_{ss'}(\mathbf{k})$ transforms as the Γ irrep and depends on sublattice indices s, s' and momentum $\mathbf{k}$. The proportionality factor of each term cannot be determined from group theory, and they will be free parameters. The derived pairing matrices in sublattice space form the groundwork of our later analyses where they are used as the mean fields in our Nambu Hamiltonian used to plot the local density of states, see Chapter 5, or as an initial guess in a self-consistent algorithm which solves for the order parameter, see Chapter 6.

4.3.1 On-site pairing

To begin with, we determine the possible on-site pairing states, and then we proceed to identify the possible nearest neighbor states, next nearest neighbor states etc. There are three in-equivalent sites on the kagome lattice, the sublattice sites A, B and C. If we determine the possible pairings on these three sites, the rest will be given by translational symmetry of the lattice. As a basis for the on-site mean-field values we use $\hat{\mathbf{e}}_1 = \begin{pmatrix}1 & 0 & 0\end{pmatrix}^T$, $\hat{\mathbf{e}}_2 = \begin{pmatrix}0 & 1 & 0\end{pmatrix}^T$ and $\hat{\mathbf{e}}_3 = \begin{pmatrix}0 & 0 & 1\end{pmatrix}^T$. We name the sites A, B and C as in Section 3.1. The method we will employ is based on the idea of starting

from a general vector $\mathbf{v}_{\text{on-site}} = \begin{pmatrix} A & B & C \end{pmatrix}^T$ and projecting the vector onto the irreps, thus finding an orthogonal basis where each basis vector transforms as the μth row of the corresponding irrep. To accomplish this we define the projection matrices [33]

$$\Pi^{\Gamma}_{\mu\nu} = \frac{d^{\Gamma}}{N_{\mathcal{G}}} \sum_{g \in \mathcal{G}} D^{\Gamma}(g)^*_{\mu\nu} D(g)\,, \tag{4.15}$$

where, as before, d^{Γ} is the dimension of the irrep Γ and $N_{\mathcal{G}}$ is the number of elements in the point group $\mathcal{G}$. $D(g)$ is a matrix representation of the element g in the vector space spanned by $\hat{\mathbf{e}}_1$, $\hat{\mathbf{e}}_2$ and $\hat{\mathbf{e}}_3$, and $D^{\Gamma}(g)_{\mu\nu}$ is the (μ,ν) entry of the matrix representation of the element g in the Γ irrep. Thus, for a set of labels (Γ,μ,ν) the matrix $\Pi^{\Gamma}_{\mu\nu}$ will be of the same rank as the matrix $D(g)$ [33]. The projection matrix onto, for instance, the A_1 irrep is

$$\Pi^{A_1} = \frac{1}{12} \sum_{g \in \mathcal{G}} D(g) \tag{4.16}$$

where $D(g)$ for $g \in D_6$ is defined in Appendix B in the case of on-site pairing. The matrices in Appendix B are determined by applying the elements of D_6 to the Γ point and determining how the sublattices transform. Projecting $\mathbf{v}_{\text{on-site}}$ onto the A_1 irrep results in

$$\Pi^{A_1}\mathbf{v}_{\text{on-site}} = \frac{1}{\sqrt{3}}(A+B+C)\hat{\mathbf{e}}^{A_1}, \quad \text{where } \hat{\mathbf{e}}^{A_1} \equiv \frac{1}{\sqrt{3}}\begin{pmatrix} 1 & 1 & 1 \end{pmatrix}^T . \tag{4.17}$$

The E_1 and E_2 irreps are two-dimensional. We construct projectors $\Pi^{E_1}_{\mu\nu}$ and $\Pi^{E_2}_{\mu\nu}$ for $(\mu,\nu) = (1,1)$ and $(\mu,\nu) = (2,1)$. The projection of $\mathbf{v}_{\text{on-site}}$ onto $\Pi^{E_2}_{11}$ and $\Pi^{E_2}_{21}$ yields

$$\Pi^{E_2}_{11}\mathbf{v}_{\text{on-site}} = \frac{1}{\sqrt{6}}(A-2B+C)\hat{\mathbf{e}}^{E_2}_{11}, \quad \text{where } \hat{\mathbf{e}}^{E_2}_{11} \equiv \frac{1}{\sqrt{6}}\begin{pmatrix} 1 & -2 & 1 \end{pmatrix}^T . \tag{4.18}$$

and

$$\Pi^{E_2}_{21}\mathbf{v}_{\text{on-site}} = \frac{1}{\sqrt{6}}(-A+2B-C)\hat{\mathbf{e}}^{E_2}_{21}, \quad \text{where } \hat{\mathbf{e}}^{E_2}_{21} \equiv \frac{1}{\sqrt{2}}\begin{pmatrix} 1 & 0 & -1 \end{pmatrix}^T . \tag{4.19}$$

The rest of the projections yield zero. Thus, we have derived a set of three mutually orthogonal vectors $\{\hat{\mathbf{e}}^{A_1}, \hat{\mathbf{e}}^{E_2}_{11}, \hat{\mathbf{e}}^{E_2}_{21}\}$. The basis is illustrated in Table 4.2 on the six lattice sites making up the hexagons in the kagome lattice. Since the pairing interaction occurs on-site, the three matrices describing the form factor $f^{\Gamma}_{\text{OS}}(\mathbf{k})$ will be diagonal and hence symmetric in sublattice space. Furthermore, the form factor will be even under the transformation $\mathbf{k} \to -\mathbf{k}$. It follows from Pauli's exclusion principle that the total wavefunction of a pair of particles should change sign after their permutation [34], and we thus categorize the on-site pairings as spin-singlets. The form factor derived from on-site interactions can hence be decomposed as [8]

$$f^{s}_{\text{OS}} = A_1 \oplus E_2\,. \tag{4.20}$$

The full classification of possible on-site pairings on the kagome lattice is seen in Table 4.2 and the corresponding mathematical expressions can be found in Appendix C.

While the tight-binding Hamiltonian in band space is given by $H^B_{\text{TB}}(\mathbf{k}) = U(\mathbf{k})H_{\text{TB}}(\mathbf{k})U^{\dagger}(\mathbf{k})$, the order parameter transforms from sublattice to band space as

$$\Delta^B_{\mathbf{k}} = U(\mathbf{k})\Delta_{\mathbf{k}}U^T(-\mathbf{k})\,. \tag{4.21}$$

A derivation of the transformation is given in Appendix D. The right column of Table 4.2 is obtained by setting the chemical potential $\mu = 0$ and plotting the entry of $\Delta^B_{\mathbf{k}}$ corresponding to the middle band, $n = 2$, over the Brillouin zone. We denote this entry by $\Delta_{n=2,\mathbf{k}}$. Notice that on the kagome lattice there is an on-site contribution not only from the A_1 irrep but also from the two-dimensional E_2 irrep. In comparison, the square lattice only has an on-site contribution from the A_1 irrep.

Irrep	Spin state	Real space	Momentum space $\Delta_{n=2,\mathbf{k}}$
A_1	singlet	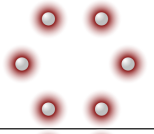	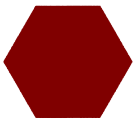
$(E_2)_{11}$	singlet	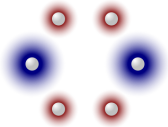	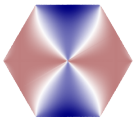
$(E_2)_{21}$	singlet	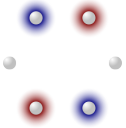	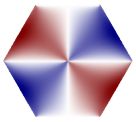

Table 4.2: Summary of the different on-site pairing states on the kagome lattice. The colour in the real space illustrations symbolizes the sign of the pairing interaction (red: 1, blue: -1), and the size symbolizes the relative strength (small: 1, big: 2). The real space pairing interactions and momentum space pairing matrices are written in Appendix C.

4.3.2 Nearest neighbor pairing

Cooper pairs between nearest neighbor sites can form as both spin-singlet and spin-triplet pairs. The general wavefunction of a pair of particles in Dirac notation is

$$|\Psi(s,\mathbf{R},;s',\mathbf{R}')\rangle \propto (|(s,\mathbf{R});(s',\mathbf{R}')\rangle \pm |(s',\mathbf{R}');(s,\mathbf{R})\rangle) \otimes (|\uparrow\downarrow\rangle \mp |\downarrow\uparrow\rangle)\,, \tag{4.22}$$

where the upper (lower) equation is for spin-singlet (spin-triplet) pairs. Rewriting equation (4.22) in second quantization leads to the following expressions for a spin-singlet pair

$$c_{s',\mathbf{R}',\uparrow}c_{s,\mathbf{R},\downarrow} + c_{s,\mathbf{R},\uparrow}c_{s',\mathbf{R}',\downarrow}\,, \tag{4.23}$$

and a spin-triplet pair

$$c_{s',\mathbf{R}',\uparrow}c_{s,\mathbf{R},\downarrow} - c_{s,\mathbf{R},\uparrow}c_{s',\mathbf{R}',\downarrow}\,, \tag{4.24}$$

between an electron located at $(s,\mathbf{R})$ and an electron located at $(s',\mathbf{R}')$. Notice that the triplet pair expression is not equal to the one where $(s,\mathbf{R}) \leftrightarrow (s',\mathbf{R}')$. This is accounted for by representing the above expression by an arrow from site $(s,\mathbf{R})$ to site $(s',\mathbf{R}')$, see e.g. the second column in Table 4.3. There are six nearest neighbor links on the kagome lattice which are not related to each other through translations by primitive lattice vectors. The links are named according to Figure 4.7(d) and the general vector takes the form $\mathbf{v}_{\mathrm{NN}} = \begin{pmatrix} a & b & c & d & e & f \end{pmatrix}^T$. The matrices $D(g)$ used to generate the projectors $(\Pi^{\Gamma}_{\mu\nu})_{s/t}$ for spin-singlet (subscript s) and spin-triplet (subscript t) are given in Appendix B. For spin-singlet pairing between nearest neighbor sites the projection

onto the irreps of D_6 yields

$$\begin{aligned}
\Pi_s^{A_1}\mathbf{v}_{\mathrm{NN}} &\propto \frac{1}{\sqrt{6}}\left(1\ 1\ 1\ 1\ 1\ 1\right)^T \equiv \hat{\mathbf{e}}^{A_1}_{\mathrm{NN,s}} \\
\Pi_s^{B_2}\mathbf{v}_{\mathrm{NN}} &\propto \frac{1}{\sqrt{6}}\left(1\ -1\ 1\ -1\ 1\ -1\right)^T \equiv \hat{\mathbf{e}}^{B_2}_{\mathrm{NN,s}} \\
(\Pi_{11}^{E_1})_s\mathbf{v}_{\mathrm{NN}} &\propto \frac{1}{\sqrt{4}}\left(0\ 1\ 1\ 0\ -1\ -1\right)^T \equiv (\hat{\mathbf{e}}^{E_1}_{11})_{\mathrm{NN,s}} \\
(\Pi_{21}^{E_1})_s\mathbf{v}_{\mathrm{NN}} &\propto \frac{1}{\sqrt{12}}\left(2\ 1\ -1\ -2\ -1\ 1\right)^T \equiv (\hat{\mathbf{e}}^{E_1}_{21})_{\mathrm{NN,s}} \\
(\Pi_{11}^{E_2})_s\mathbf{v}_{\mathrm{NN}} &\propto \frac{1}{\sqrt{12}}\left(2\ -1\ -1\ 2\ -1\ -1\right)^T \equiv (\hat{\mathbf{e}}^{E_2}_{11})_{\mathrm{NN,s}} \\
(\Pi_{21}^{E_2})_s\mathbf{v}_{\mathrm{NN}} &\propto \frac{1}{\sqrt{4}}\left(0\ 1\ -1\ 0\ 1\ -1\right)^T \equiv (\hat{\mathbf{e}}^{E_2}_{21})_{\mathrm{NN,s}}
\end{aligned} \tag{4.25}$$

whereas $\Pi_s^{A_2}\mathbf{v}_{\mathrm{NN}} = \Pi_s^{B_1}\mathbf{v}_{\mathrm{NN}} = \mathbf{0}$. We notice that, for example, $\hat{\mathbf{e}}^{A_1}_{\mathrm{NN,s}} \cdot \hat{\mathbf{e}}^{B_2}_{\mathrm{NN,s}} = 0$ because the irreps A_1 and B_2 correspond to orthogonal subspaces. Thus we have derived a set of six mutually orthogonal unit vectors, and this basis is illustrated in Table 4.3. We have established that the illustration of nearest neighbor spin-triplet pairs should include a bond direction which represents a specific order of the fermion operators. Bond directions are accounted for by multiplying all of the matrices $D(g)$ representing a reflection (or rotation by π around the C_2' or C_2'' axis) by -1. The projectors for spin-triplet pairs are constructed from these matrices, given in Appendix B, and we find six mutually orthogonal vectors illustrated in Table 4.3. In conclusion, the form factors deriving from nearest neighbor interactions are found to have the following contributions [8]

$$f^s_{\mathrm{NN}} = A_1 \oplus B_2 \oplus E_1 \oplus E_2\,, \tag{4.26}$$

$$f^t_{\mathrm{NN}} = A_2 \oplus B_1 \oplus E_1 \oplus E_2\,. \tag{4.27}$$

4.3.3 The sublattice-odd pairing states

In addition to six symmetry-allowed sublattice-even pairing states, we find six sublattice-odd pairing states. The allowed symmetry properties of a superconducting order parameter on a kagome lattice is shown in Table 4.4.

Upon plotting the nine entries of the order parameters $\Delta_n^\Gamma(\mathbf{k})$, where Γ is one of the allowed irreps, in band space (3×3 matrices), we find that while the sublattice-even states have non-zero entries on the diagonal (they might also have some off-diagonal contribution), the sublattice-odd states only have off-diagonal contributions. As the matrix is in band basis, the diagonal corresponds to intraband pairing, i.e. in quasiparticle basis a gap opens up between an electron band and its associated hole band counterpart, while the off-diagonal components correspond to interband pairing. The difference between these two notions is illustrated in Figure 4.4.

For example, the singlet A_1 order parameter (with contributions up to and including NN bonds) only has non-zero entries on the diagonal in band space, whereas the singlet B_2 order parameter only has one of the three upper off-diagonal components different from zero. As such, it was found that some of the pairing states arising at the NN level lead to interband or finite energy Cooper pairing. Intraband Cooper pairs are formed between electrons occupying states in the same energy band, and thus their energy levels will be similar. On the other hand, interband Cooper pairs form between electrons of different energy bands, and the energies of the electrons will in general differ. It is thus less energetically favorable for the interband pairs to form. Interband pairing is a type

Irrep	Real space		Momentum space $\Delta_{n=2,\mathbf{k}}$	
	Singlet	**Triplet**	**Singlet**	**Triplet**
A_1			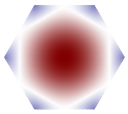	
A_2		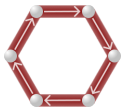		Interband pairing
B_1		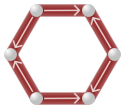		
B_2	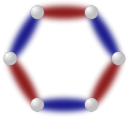		Interband pairing	
$(E_1)_{11}$	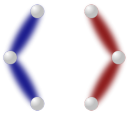	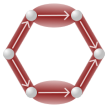	Interband pairing	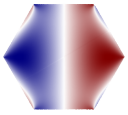
$(E_1)_{21}$		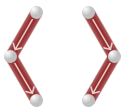	Interband pairing	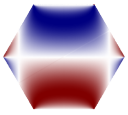
$(E_2)_{11}$	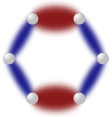	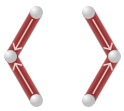	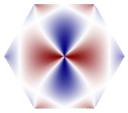	Interband pairing
$(E_2)_{21}$	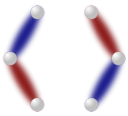	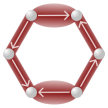	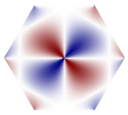	Interband pairing

Table 4.3: Summary of the different nearest neighbor pairing states on the kagome lattice. For the singlet states the colour in the real space illustrations symbolizes the sign of the pairing interaction (red: 1, blue: -1), and the size symbolizes the relative strength (small: 1, big: 2). The real space pairing interactions and momentum space pairing matrices are written in Appendix C. Notice that A_1 and the components of E_2 have a hexagonal node corresponding to the shape of the Fermi surface for $\mu = 0$. This is a plausible explanation of the small gaps observed in [35], where only nearest neighbor contributions were included. The chemical potential in [35] was set to $\mu = 0.4$, thus moving away from the upper van Hove singularity.

	Singlet		**Triplet**	
σ	-1		$+1$	
k	$+1$	-1	$+1$	-1
Sublattice	$+1$	-1	-1	$+1$
Total	-1	-1	-1	-1

Table 4.4: Allowed symmetry properties of the superconducting order parameter $\Delta_{\sigma\sigma',ss'}(\mathbf{k})$. The symmetry property is symbolized by $+1$ (-1) for symmetric (anti-symmetric) under spin permutation, sublattice permutation or a parity transformation. In two dimensions, a parity transformation, $\mathbf{k} \to -\mathbf{k}$, is equivalent to a rotation by π around the principal axis (a C_2 operation).

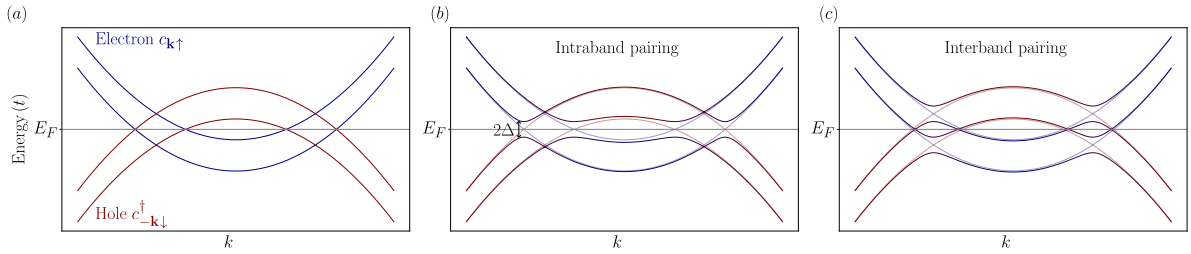

Figure 4.4: The distinction between intra- and interband pairing. For illustrative purposes two parabolic electron bands are considered. (a) The bands in Nambu space: two electron bands (blue) and their associated hole band counterparts (red). (b) An intraband order parameter opens a gap between an electron band and its hole band counterpart while (c) an interband order parameter opens a gap between an electron band and a hole band different from its counterpart.

of pairing that happens away from the Fermi surface. This more exotic type of pairing arises from the sublattice degree of freedom of the kagome lattice: the exact origin is detailed below.

The quasiparticle bands for a system with superconductivity are plotted (black) on top of the tight-binding bands (grey) for different pairing states up to NN order: see Figures 4.5 and 4.6 for intra- and interband results, respectively. The chemical potential $\mu = 0$, which corresponds to a hexagonal Fermi surface that touches the Brillouin zone boundary at the M-points. To make the effects more clear, the proportionality factors in equation (4.14) have been set to $\Delta_0 = 0.5t$ and $\Delta_1 = \frac{\Delta_0}{2}$ for the states with both on-site and NN contributions, and $\Delta_1 = 0.5t$ for the states with only NN contributions.

We now turn our attention to the question of why these interband states from NN pairing appear on the kagome lattice, and whether they would appear on other familiar lattices such as the square, triangular or honeycomb lattice. The honeycomb lattice, for one, also contains multiple (two) sites in a single unit cell and therefore also has a sublattice degree of freedom. We will argue that there is a subtle feature of the kagome lattice which results in additionally allowed pairing states, which would not be allowed on the aforementioned lattices. This feature leads to the possibility of having superconducting order parameters that are, for instance, even-parity, spin-triplet, sublattice-odd. In two dimensions a parity transformation is equivalent to a rotation by π around the principal axis (a C_2 operation). Focusing on nearest-neighbor pairing, the special feature of the kagome lattice does not originate from the fact that it is a non-Bravais lattice (i.e. has lattice sites which are non-equivalent and thus the unit cell contains multiple lattice sites, introducing a sublattice index), which is also the case for the honeycomb lattice. Rather, it originates from the fact that on the kagome lattice the nearest-neighbor bonds connected by a C_2 transformation are *not* connected

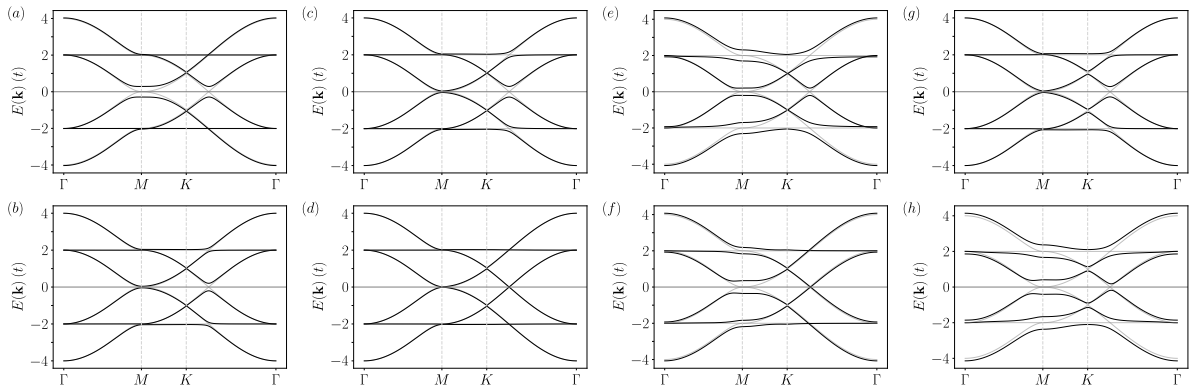

Figure 4.5: The quasiparticle energy bands for the intraband pairing states, namely the (a) singlet A_1 state, (b) triplet B_1 state, (c) triplet $(E_1)_{11}$, (d) triplet $(E_1)_{21}$, (e) singlet $(E_2)_{11}$, (f) singlet $(E_2)_{21}$, (g) complex $(E_1)_{11}+i(E_1)_{21}$ and (h) complex $(E_2)_{11}+i(E_2)_{21}$ state. The chemical potential $\mu = 0$.

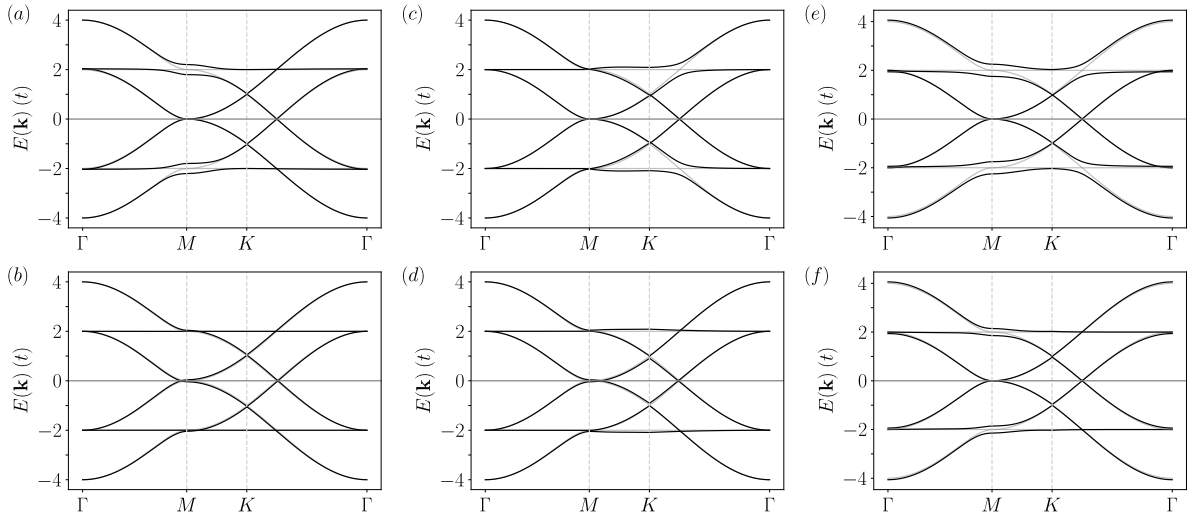

Figure 4.6: The quasiparticle energy bands for the interband pairing states, namely the (a) triplet A_2 state, (b) singlet B_2 state, (c) singlet $(E_1)_{11}$ state, (d) singlet $(E_1)_{21}$ state, (e) triplet $(E_2)_{11}$ state and (f) triplet $(E_2)_{21}$ state. The chemical potential $\mu = 0$.

by a translation by a primitive lattice vector. This is contrary to the square, triangular and honeycomb lattices where the bonds connected by a C_2 transformation are *also* connected by a lattice translation. The latter restricts the possible pairing states and leads to the connection between the character of the C_2 transformation and the spin-singlet/-triplet nature of the pairing well-known from the square lattice.

On the square lattice (with one site per unit cell) it is sufficient to fix the sign of only two bonds: then the rest are given by translations. Thus the square lattice has two independent bonds. More importantly, the C_2 bond partners (the bonds connected by a C_2 transformation) are *not* independent, since these are restricted to be equal to the initial bonds (pre-rotation) through lattice translations. On the triangular lattice (with one atom per unit cell) one needs to fix the sign of three bonds. The remainder of the bonds are given by translations. The bonds obtained by a C_2 transformation of the three independent bonds are not independent from the initial ones since these are also connected by translations. On the honeycomb lattice (with two atoms per

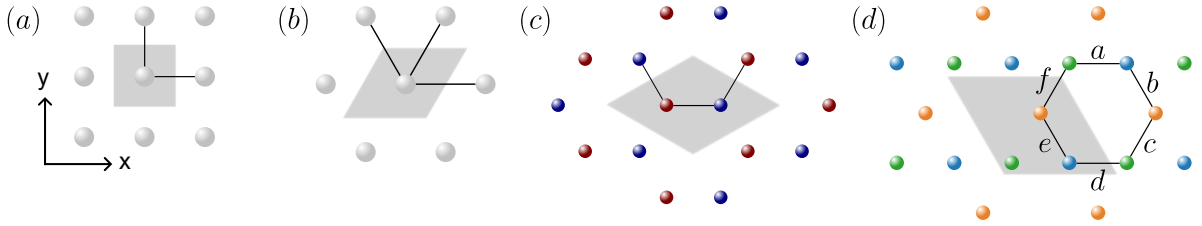

Figure 4.7: The (a) square, (b) triangular, (c) honeycomb and (d) kagome lattice. The independent nearest neighbor bonds are illustrated with a full black line.

unit cell) one needs to fix the sign of three bonds. In this case, the C_2 bond partners are also *not* independent for the same reason as the preceding instances. Finally, on the kagome lattice one needs to fix the sign of six bonds and the C_2 bond partners cannot be obtained through translations by one of the primitive lattice vectors. Figure 4.7 illustrates the independent nearest neighbor bonds on the square, triangular, honeycomb and kagome lattices. If another lattice has the same feature as the kagome lattice, then it is expected that pairing states which are more complex than the traditional even-parity spin-singlet and odd-parity spin-triplet would be allowed. Although it would be interesting to study under which conditions (if any) it would be possible to stabilize an interband pairing state on the kagome lattice, the physically relevant states for the AV_3Sb_5 compounds are most likely the more conventional intraband pairing states. We study impurity effects on those in Chapters 5 and 6.

4.3.4 *2nd* and *3rd* nearest neighbor pairing

For completeness, we also provide the pairing matrices for next nearest neighbor (NNN) and third nearest neighbor (3rd) pairing states, see Tables 4.5 and 4.6. In the case of third nearest neighbor pairings, there are not six but nine bonds in total: there are bonds that couple sites across the hexagon (denoted in-hexagon) and bonds that couple sites along the lattice links (denoted out-of-hexagon). Since these two bond categories do not transform into each other under any of the elements of the D_6 point group, the problem can be decomposed into two separate problems of dimension three and six.

In the following chapters we will only include interactions up to and including nearest neighbors. The proportionality factors are chosen to be $\Delta_0 = 0.2t$ and $\Delta_1 = 0.1t$ in the cases where the order parameter has an on-site contribution, and $\Delta_1 = 0.2t$ otherwise.

Irrep	Real space		Momentum space $\Delta_{n=2,\mathbf{k}}$	
	Singlet	**Triplet**	**Singlet**	**Triplet**
A_1	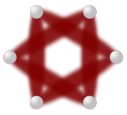			
A_2				Interband pairing
B_1	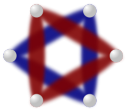		Interband pairing	
B_2				
$(E_1)_{11}$	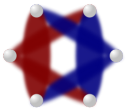	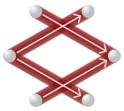	Interband pairing	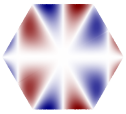
$(E_1)_{21}$			Interband pairing	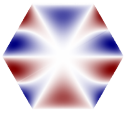
$(E_2)_{11}$	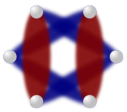		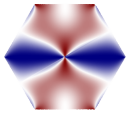	Interband pairing
$(E_2)_{21}$			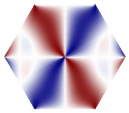	Interband pairing

Table 4.5: Summary of the different next nearest neighbor pairing states on the kagome lattice. For the singlet states the colour in the real space illustrations symbolizes the sign of the pairing interaction (red: 1, blue: -1), and the size symbolizes the relative strength (small: 1, big: 2). The real space pairing interactions and momentum space pairing matrices are written in Appendix C.

Irrep	Real space		Momentum space $\Delta_{n=2,\mathbf{k}}$	
	Singlet	Triplet	Singlet	Triplet
A_1	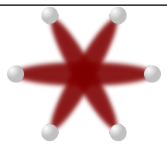		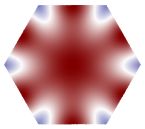	
B_1				
$(E_1)_{11}$				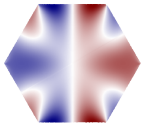
$(E_1)_{21}$				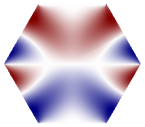
$(E_2)_{11}$	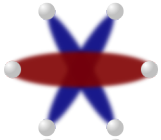		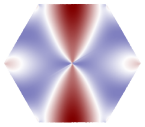	
$(E_2)_{21}$	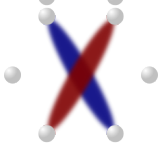		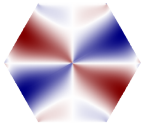	

Table 4.6: Summary of the different 3rd nearest neighbor in-hexagon pairing states on the kagome lattice. For the singlet states the colour in the real space illustrations symbolizes the sign of the pairing interaction (red: 1, blue: -1), and the size symbolizes the relative strength (small: 1, big: 2). The real space pairing interactions and momentum space pairing matrices are written in Appendix C.

Irrep	Real space	
	Singlet	Triplet
A_1	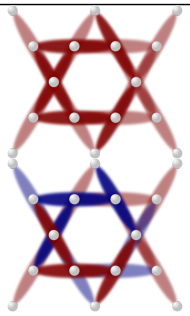	
A_2		
B_1	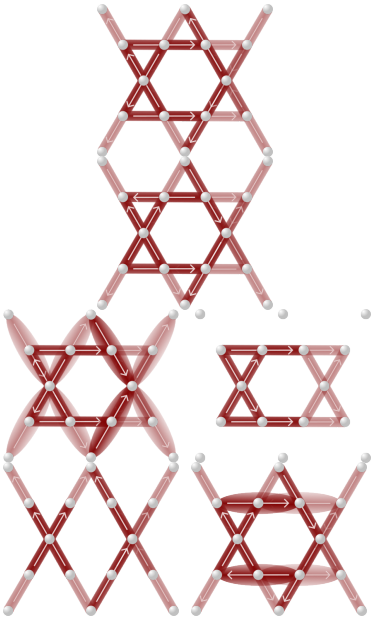	
B_2		
$(E_1)_{11}$		
$(E_1)_{21}$		
$(E_2)_{11}$	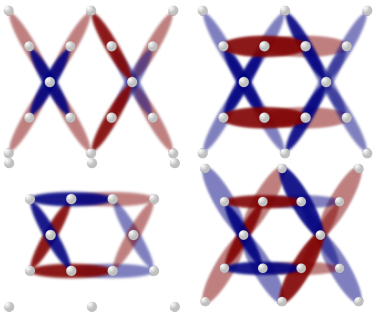	
$(E_2)_{21}$		

Table 4.7: Summary of the different 3rd nearest neighbor out-of-hexagon pairing states on the kagome lattice. For the singlet states the colour in the real space illustration symbolizes the sign of the pairing interaction (red: 1, blue: -1), and the size symbolizes the relative strength (small: 1, big: 2). The six bonds that are independent have an opaque colour as compared to the more transparent colours of the remaining bonds obtained from translations of the original six. In this case only the real space illustrations are provided.

Chapter 5

Adding an impurity: The T-matrix approximation

"...lined by resonant states like cypress trees along a Tuscan driveway."

Brian M. Andersen

In this chapter we examine the effect of impurities on different superconducting states on the kagome lattice. We introduce two types of impurity potentials: one modelling a potential impurity, and one modelling a magnetic impurity which interacts differently with different spin. The local density of states (LDOS) is obtained through the T-matrix method. The LDOS is an interesting property since it can be probed experimentally by scanning tunneling microscopy experiments. We furthermore model the suppression of the critical temperature T_c as a function of the rate of scattering on potential impurities, another property which can be measured experimentally.

In Chapter 4 we introduced different superconducting orders on the kagome lattice, some of which feature sign changes on the Fermi surface and others which do not. Sign-changing and non-sign-changing superconducting states are both sensitive to the presence of magnetic impurities. This is evidenced by the appearance of low-energy impurity bound states in the LDOS and a strong suppression of the critical temperature. Magnetic impurities have local magnetic moments which interact with and perturb the paired electrons. An electron, constituting one-half of a Cooper pair, can occupy the bound state introduced by the magnetic impurity, and as a result the Cooper pair breaks. Due to the similar behaviour of sign-changing and non-sign-changing states to magnetic impurities, this type of impurity is not well-suited to distinguish between different types of superconductivity in real materials. On the other hand, it is a well-known result that s-wave superconductivity is not as sensitive to potential impurities as the sign-changing states are. Here, we thus mainly focus on the effect of potential impurities. The main result of this chapter is the discovery of a mechanism on the kagome lattice which renders a d-wave order parameter effectively behaving as an s-wave order parameter, in the sense that it is more robust to potential impurities than expected. We calculate an approximate Green function to understand and explain the effect with simple calculations.

5.1 The T-matrix method

The T-matrix method is used to determine the full Green function of a system with an impurity as described by a full Hamiltonian on the generic form $H = H^{(0)} + H_{\text{imp}}$, where $H^{(0)}$ is the Hamiltonian

of the system without an impurity and H_{imp} is the Hamiltonian of the impurity. The operators of the system depend on a set of quantum numbers which we arbitrarily denote by indices $\{a, b, c, ...\}$ in the following derivation. We denote the Green function of the system without an impurity by $G^{(0)}(a, b)$ and of the full system by $G(a, b)$. With the introduced notation, the equations of motion of the two Green functions $G^{(0)}(a, b) \equiv -\langle T_\tau c_a c_b^\dagger \rangle_0$ and $G(a, b) \equiv -\langle T_\tau c_a c_b^\dagger \rangle$ are given by [36]

$$(-\partial_{\tau_a} - H^{(0)}(a))G^{(0)}(a, b) = \delta_{a,b}\,, \tag{5.1}$$

$$(-\partial_{\tau_a} - H(a))G(a, b) = \delta_{a,b}\,. \tag{5.2}$$

Setting the two equations equal to each other yields

$$\begin{aligned}
&(-\partial_{\tau_a} - H(a))G(a, b) = \\
&(-\partial_{\tau_a} - H(a) + H_{\text{imp}}(a))G^{(0)}(a, b) = \\
&(-\partial_{\tau_a} - H(a))G^{(0)}(a, b) + H_{\text{imp}}(a)G^{(0)}(a, b) = \\
&(-\partial_{\tau_a} - H(a))G^{(0)}(a, b) + \sum_c \delta_{a,c} H_{\text{imp}}(c)G^{(0)}(c, b)\,.
\end{aligned} \tag{5.3}$$

We obtain the so-called Dyson integral equation for the full Green function by multiplying with the matrix $(-\partial_{\tau_a} - H(a))^{-1}$ on the left and using equation (5.2)

$$G(a, b) = G^{(0)}(a, b) + \sum_c G(a, c)H_{\text{imp}}(c)G^{(0)}(c, b)\,. \tag{5.4}$$

In Nambu formalism $G(a, b)$ and $H_{\text{imp}}(c)$ denote 6×6 (2×2) matrices for the kagome (square) lattice. Choosing a position and energy basis, $(\mathbf{r}, \omega)$, and setting the location of the impurity at the origin, $c = \mathbf{0}$, we obtain

$$G(\mathbf{r}, \mathbf{r}', \omega) = G^{(0)}(\mathbf{r} - \mathbf{r}', \omega) + G(\mathbf{r}, \mathbf{0}, \omega)H_{\text{imp}}(\mathbf{0})G^{(0)}(\mathbf{0} - \mathbf{r}', \omega)\,, \tag{5.5}$$

where it was used that the system without the impurity is translationally invariant and thus the Green function only depends the difference in positions. Evaluating $G(\mathbf{r}, \mathbf{r}', \omega)$ at $\mathbf{r}' = \mathbf{0}$ yields

$$G(\mathbf{r}, \mathbf{0}, \omega) = G^{(0)}(\mathbf{r}, \omega) + G(\mathbf{r}, \mathbf{0}, \omega)H_{\text{imp}}(\mathbf{0})G^{(0)}(\mathbf{0}, \omega)\,. \tag{5.6}$$

We can thus iterate to obtain

$$G(\mathbf{r}, \mathbf{0}, \omega) = G^{(0)}(\mathbf{r}, \omega)\sum_{n=0}^{\infty}(H_{\text{imp}}(\mathbf{0})G^{(0)}(\mathbf{0}, \omega))^n = G^{(0)}(\mathbf{r}, \omega)(1 - H_{\text{imp}}(\mathbf{0})G^{(0)}(\mathbf{0}, \omega))^{-1}\,, \tag{5.7}$$

where convergence of the geometric series is assumed. The exact solution of the full Green function is thus

$$G(\mathbf{r}, \mathbf{r}', \omega) = G^{(0)}(\mathbf{r} - \mathbf{r}', \omega) + G^{(0)}(\mathbf{r}, \omega)(1 - H_{\text{imp}}(\mathbf{0})G^{(0)}(\mathbf{0}, \omega))^{-1}H_{\text{imp}}(\mathbf{0})G^{(0)}(-\mathbf{r}', \omega)\,, \tag{5.8}$$

which is only dependent on the Green function of the clean system. We can define a matrix, called the T-matrix, as

$$T(\mathbf{0}, \omega) \equiv (1 - H_{\text{imp}}(\mathbf{0})G^{(0)}(\mathbf{0}, \omega))^{-1}H_{\text{imp}}(\mathbf{0}) \equiv D(\omega)^{-1}H_{\text{imp}}(\mathbf{0})\,. \tag{5.9}$$

where we have also defined $D(\omega) \equiv 1 - H_{\text{imp}}(\mathbf{0})G^{(0)}(\mathbf{0}, \omega)$ for later convenience. This definition simplifies the expression for the full Green function which becomes

$$G(\mathbf{r}, \mathbf{r}', \omega) = G^{(0)}(\mathbf{r} - \mathbf{r}', \omega) + G^{(0)}(\mathbf{r}, \omega)T(\mathbf{0}, \omega)G^{(0)}(-\mathbf{r}', \omega)\,. \tag{5.10}$$

This equation describes the propagation of a particle from site $\mathbf{r}'$ to site $\mathbf{r}$ containing contributions from the free propagation from $\mathbf{r}'$ to $\mathbf{r}$ in addition to scatterings off the impurity located at the origin. It follows that the study of a single impurity in a system simplifies to the study of the properties (or poles) of the T-matrix [36].

In equation (4.7) of Chapter 4 we introduced the BdG Hamiltonian from which we can calculate the retarded Nambu Green function

$$\mathcal{G}^{(0)}(\mathbf{k},\omega) = ((\omega + i\eta)\mathbb{1} - H_{BdG}(\mathbf{k}))^{-1}\,. \tag{5.11}$$

This is the Green function of our system without an impurity and it is referred to as the free Green function. As was also mentioned before, it is a 6×6 matrix in the case of the kagome lattice and the constituents are denoted

$$\mathcal{G}^{(0)} = \begin{pmatrix} G^{(0)} & F^{(0)} \\ \bar{F}^{(0)} & \bar{G}^{(0)} \end{pmatrix}\,, \tag{5.12}$$

where the function dependencies have been suppressed. In the case of the square lattice, $\mathcal{G}^{(0)}$ is a 2×2 matrix. The spin-summed electronic local density of states of the clean system is calculated from the free Green function in the following manner

$$\rho_{ss'}(\mathbf{r},\omega) = \frac{-1}{\pi}\mathrm{Im}(G^{(0)}_{ss'}(\mathbf{r},\omega) + \bar{G}^{(0)}_{ss'}(\mathbf{r},-\omega))\,, \tag{5.13}$$

where $G^{(0)}_{ss'}(\mathbf{r},\omega) = \frac{1}{N}\sum_{\mathbf{k}} G^{(0)}(\mathbf{k},\omega)e^{i\mathbf{k}\cdot\mathbf{r}}$. The local density of states of the full system with an impurity is similarly found from

$$\rho_{ss'}(\mathbf{r},\omega) = \frac{-1}{\pi}\mathrm{Im}(G_{ss'}(\mathbf{r},\mathbf{r},\omega) + \bar{G}_{ss'}(\mathbf{r},\mathbf{r},-\omega))\,. \tag{5.14}$$

A peak in the LDOS will appear if either $G(\mathbf{r},\mathbf{r},\omega)$ or $\bar{G}(\mathbf{r},\mathbf{r},-\omega)$ diverges [37].

5.2 The local density of states of the clean system

The local density of states at sublattice site $s = s' = A$ and $\mathbf{r} = 0$, corresponding to $\rho_{AA}(\mathbf{0},\omega)$, for the intraband order parameters found in Chapter 4 is plotted in figure 5.1. In all figures, the x-axis has been scaled by Δ_c, where c stands for coherence peak. Δ_c is obtained from $\Delta_c = \max(\Delta_{\mathbf{k}\in\mathbf{k}_\mathrm{F}})$ where $\mathbf{k}_F$ denotes the set of momenta corresponding to the two-dimensional Fermi surface. An explanation of this equation is as follows: a momentum-dependent superconducting order parameter $\Delta_{\mathbf{k}}$ opens up a momentum-dependent gap on the Fermi surface. If we locate the momentum at which the order parameter is maximum, then moving away from that momentum along the Fermi surface will lead to a decrease in the gap and thus the energy band will decrease along this direction. On the other hand, perpendicular to the Fermi surface the energy band will increase and this saddle point behaviour of the energy band will lead to a coherence peak.

Figure 5.1(a) depicts the full, U-type gap in the LDOS from the singlet s-wave order parameter, and Figure 5.1(b) shows the gap obtained from different singlet d-wave order parameters. The time-reversal breaking combination $d + id$ (black) leads to a full gap, while the individual components, $d_{x^2-y^2}$ (light green) and d_{xy} (blue), lead to V-type gaps. Since the individual components break rotational symmetry, which is visible from the real space depictions of the order parameters in Chapter 4, the LDOS obtained from these order parameters will depend on the sublattice site. More specifically, the LDOS on sites A and C will be the same while it will change on sublattice site B. To understand this one can compare the weights in Figure 3.4(c) of Chapter 3 with the order

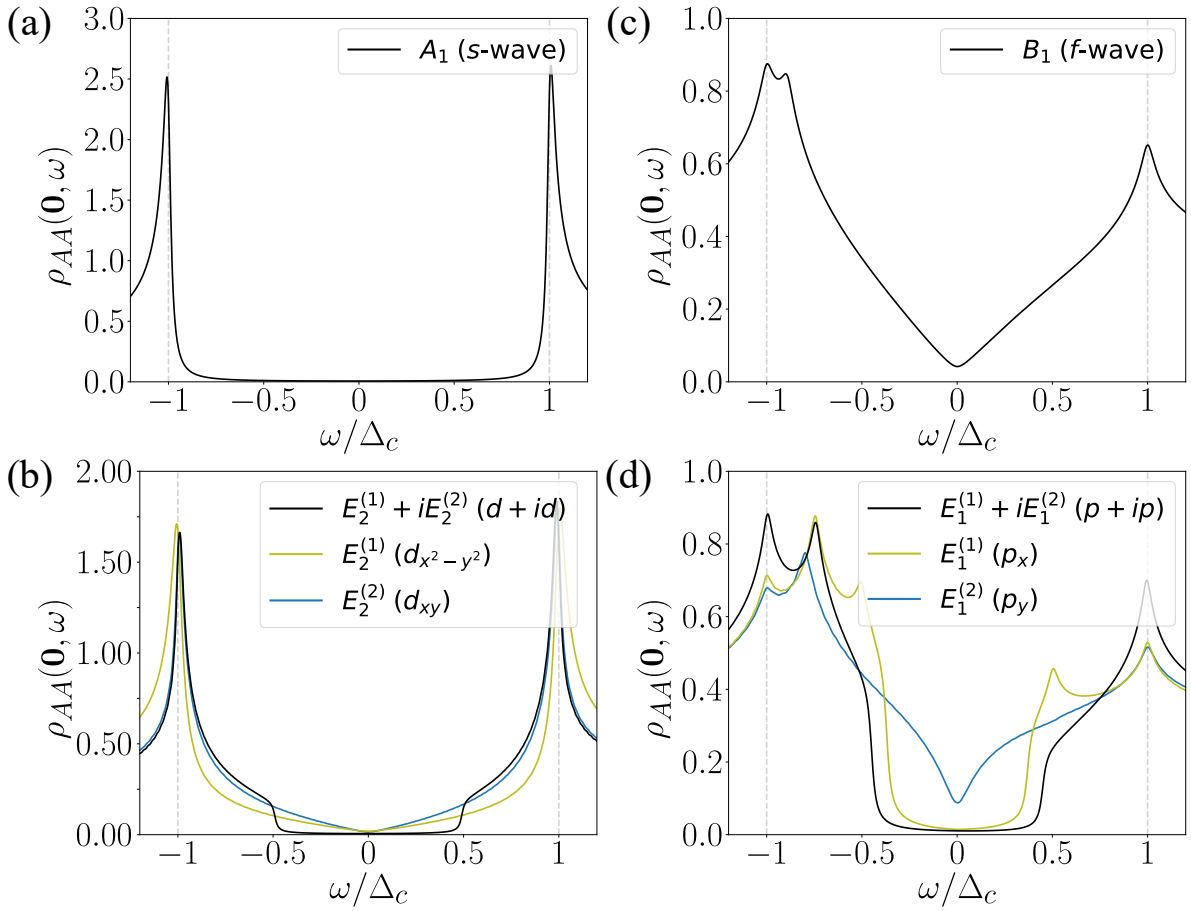

Figure 5.1: The local density of states on site A, $\rho_{AA}(\mathbf{0},\omega)$, at energies close to the Fermi energy $\omega = 0$ for a clean system with different superconducting order parameters. (a) An s-wave order parameter leads to a full, U-type gap. (b) The TRSB order parameter $d+id$ has a full gap (black), and the individual components, $d_{x^2-y^2}$ (light green) and d_{xy} (blue), have a V-type gap. (c) A nodal f-wave order parameter leading to a V-type gap. (d) The TRSB order parameter $p+ip$ (black) and the individual components p_x (light green) and p_y (blue). $p+ip$ features a full gap while the p_y gap is of the V-type. Sublattice A has zero weight on the location of the Fermi surface where p_x has a node, and thus it has more of a U-type gap. For the singlet order parameters the chemical potential was set to $\mu = 0.0$, and for the triplet order parameters it was set to $\mu = 0.08$. The plots are made with 1500^2 momentum values in the first BZ and a smearing of $\eta = 0.002$, except for the p_y order parameter which was run with $\eta = 0.0025$ for smoothness of the curve.

parameters in momentum and energy space depicted in Section 4.3 of Chapter 4. The chemical potential for the singlet order parameters was set to $\mu = 0$.

Figure 5.1(c) depicts the gap from an f-wave order parameter which is of the V-type. Next to the coherence peaks, remnants of the van Hove singularity are visible. Figure 5.1(d) shows the LDOS of a system with a p-wave gap. The $p + ip$ combination leads to a full gap (black) and the individual components, p_x (light green) and p_y (blue), are superimposed. The p_y component has a V-type gap, but the p_x component is more similar to a U-type gap. This is due to the fact that we are plotting the LDOS at site A, and it has zero weight on the part of the Fermi surface which is nodal for the p_x component. Instead, if the LDOS on site B was plotted, the gap would appear more V-shaped since the majority of the weight would now be located exactly on top of the node. The LDOS for the p_x component has two coherence peaks since it has two local maxima on the parts of the Fermi surface which have weight: one close to the $\mathbf{M}_3$ point and another between the $\mathbf{M}_3$ and $\mathbf{M}_4$ point. The chemical potential for the triplet order parameters was set to $\mu = 0.08$ (just above the upper van Hove singularity), since the triplet order parameters only have nearest neighbor contributions and these contributions have a node along the hexagonal Fermi surface corresponding to $\mu = 0$, as seen in Section 4.3.

5.3 Single-impurity study on the square lattice

To fully appreciate the results obtained on the kagome lattice we briefly go through the results of a single-impurity study on the square lattice. The mean-field BdG Hamiltonian on the square lattice in Nambu formalism is

$$\mathcal{H}_{\text{BdG}}^{\text{square}} = \sum_{\mathbf{k}\in BZ} \begin{pmatrix} c_{\mathbf{k},\uparrow}^\dagger & c_{-\mathbf{k},\downarrow} \end{pmatrix} \begin{pmatrix} \xi_{\mathbf{k}} & -\Delta_{\mathbf{k}} \\ -\Delta_{\mathbf{k}}^* & -\xi_{\mathbf{k}} \end{pmatrix} \begin{pmatrix} c_{\mathbf{k},\uparrow} \\ c_{-\mathbf{k},\downarrow}^\dagger \end{pmatrix}, \tag{5.15}$$

and the Nambu Green function is given by

$$\mathcal{G}^{(0)}(\mathbf{k}, i\omega_n) = \frac{i\omega_n \tau_0 + \xi_{\mathbf{k}}\tau_z - \Delta_{\mathbf{k}}\frac{\tau_+}{2} - \Delta_{\mathbf{k}}^*\frac{\tau_-}{2}}{(i\omega_n)^2 - E_{\mathbf{k}}^2}, \tag{5.16}$$

where $\tau_+ = \tau_x + i\tau_y = \begin{pmatrix} 0 & 2 \\ 0 & 0 \end{pmatrix}$ and $\tau_- = \tau_x - i\tau_y = \begin{pmatrix} 0 & 0 \\ 2 & 0 \end{pmatrix}$ with τ_x, τ_y, τ_z being Pauli matrices representing Nambu space, and $\tau_0 = \mathbb{1}_{2\times 2}$. Furthermore, $E_{\mathbf{k}} = \sqrt{\xi_{\mathbf{k}}^2 + |\Delta_{\mathbf{k}}|^2}$ where

$$\xi_{\mathbf{k}} = -2t(\cos(\mathbf{k}\cdot\mathbf{t}_1) + \cos(\mathbf{k}\cdot\mathbf{t}_2)) - \mu \tag{5.17}$$

is the energy band derived from a tight-binding model on the square lattice with the intersite distance set to $a = 1$, such that the primitive lattice vectors are $\mathbf{t}_1 = \begin{pmatrix} 1 & 0 \end{pmatrix}^T$ and $\mathbf{t}_2 = \begin{pmatrix} 0 & 1 \end{pmatrix}^T$. As shown in Chapter 4 for the kagome lattice, one can decompose the mean-field superconducting order parameter in terms of the point group form factors. The point group of the two-dimensional square lattice is D_4. From interactions up until nearest neighbor distance the superconducting order parameter can transform as the one-dimensional A_1 irrep (s-wave at lowest order), the one-dimensional B_1 irrep ($d_{x^2-y^2}$-wave at lowest order) or the two-dimensional E irrep (components are p_x- and p_y-wave at lowest order). Here, the A_1 and B_1 irreps are even under parity, $\mathbf{k} \to -\mathbf{k}$, while the E irrep is odd. Assuming that the interaction potential is translationally invariant, the order parameter can take the following forms [38]

$$\Delta_{\mathbf{k}}^{A_1} = \Delta_0 + \Delta_1(\cos(k_x) + \cos(k_y)), \tag{5.18}$$

$$\Delta_{\mathbf{k}}^{B_1} = \Delta_1(\cos(k_x) - \cos(k_y))\,, \tag{5.19}$$

or

$$\Delta_{\mathbf{k}}^{E_x+iE_y} = \Delta_1(\sin(k_x) + i\sin(k_y))\,, \tag{5.20}$$

where the two-dimensional order parameter is written in the time-reversal symmetry breaking complex combination. At an interaction distance of $\sqrt{2}$, i.e. second neighbor pairing, it is possible to form a singlet B_2 (or d_{xy}-wave) pairing state which has an order parameter of the form [38]

$$\Delta^{B_2} = \Delta_2 \sin(k_x)\sin(k_y)\,. \tag{5.21}$$

Although the B_1 and B_2 pairing states are in general not degenerate in energy, we can construct the time-reversal symmetry breaking complex combination of the two irreps in order to be able to compare with our kagome results. The $d_{x^2-y^2} + id_{xy}$-wave order parameter is

$$\Delta^{B_1+iB_2} = \Delta(\cos(k_x) - \cos(k_y) + i\sin(k_x)\sin(k_y))\,. \tag{5.22}$$

The retarded Green function is found by analytical continuation of equation (5.16) letting $i\omega_n \to \omega + i\eta$, and the full Green function in the T-matrix approach is found by equation (5.10). Finally, the homogeneous LDOS is calculated from equation (5.13), where, in the case of the square lattice, the constituents of the Nambu Green function do not have any sublattice dependence. The local density of states at $\mathbf{r} = \mathbf{0}$ for some of the different order parameters is seen in Figure 5.2. As expected, the s-wave, $d + id$ and $p + ip$ order parameters feature a full, U-type gap whereas the $d_{x^2-y^2}$-wave order parameter is of the V-type.

The impurity Hamiltonian for a non-magnetic impurity is

$$H_{\text{imp}}^{p} = V\tau_z\,, \tag{5.23}$$

while the Hamiltonian for a magnetic impurity takes the form

$$H_{\text{imp}}^{m} = V\tau_0\,. \tag{5.24}$$

We wish to study for which energies $\text{Det}(T^{-1}) = 0$, since this would correspond to a pole in the T-matrix. The T-matrix is not well-defined if T^{-1} is singular (i.e. has a determinant equal to zero). In the case where $V \neq 0$ and H_{imp}^{-1} is well-defined, we can calculate $T^{-1}(\mathbf{0},\omega) = H_{\text{imp}}^{-1}(\mathbf{0}) - \mathcal{G}^{(0)}(\mathbf{0},\omega)$ [37]. Calculating the determinant for a potential/magnetic (p/m) impurity, $H_{\text{imp}}^{p/m}$, and setting it equal to zero yields the following quadratic equation in V

$$\pm V^{-2} + V^{-1}(-\bar{G}^{(0)} \mp G^{(0)}) + G^{(0)}\bar{G}^{(0)} - F^{(0)}\bar{F}^{(0)} = 0\,, \tag{5.25}$$

where $\pm$ and $\mp$ is for a magnetic/potential impurity, and position and energy dependencies have been suppressed. The two solutions for a potential impurity are

$$(V_{\pm}^{p})^{-1} = \frac{1}{2}\left(G^{(0)} - \bar{G}^{(0)} \pm \sqrt{\left(G^{(0)} + \bar{G}^{(0)}\right)^2 - 4F^{(0)}\bar{F}^{(0)}}\right)\,. \tag{5.26}$$

For a magnetic impurity they are

$$(V_{\pm}^{m})^{-1} = \frac{1}{2}\left(G^{(0)} + \bar{G}^{(0)} \pm \sqrt{\left(G^{(0)} - \bar{G}^{(0)}\right)^2 + 4F^{(0)}\bar{F}^{(0)}}\right)\,. \tag{5.27}$$

The right-hand side of these equations can be calculated numerically for both $\mathcal{G}^{(0)}(\mathbf{0},\omega)$ and $\mathcal{G}^{(0)}(\mathbf{0},-\omega)$ and plotted as a function of ω. Furthermore, superimposing horizontal lines corresponding to V^{-1} and determining the intersections with the right-hand side yields energy values where bound states can appear.

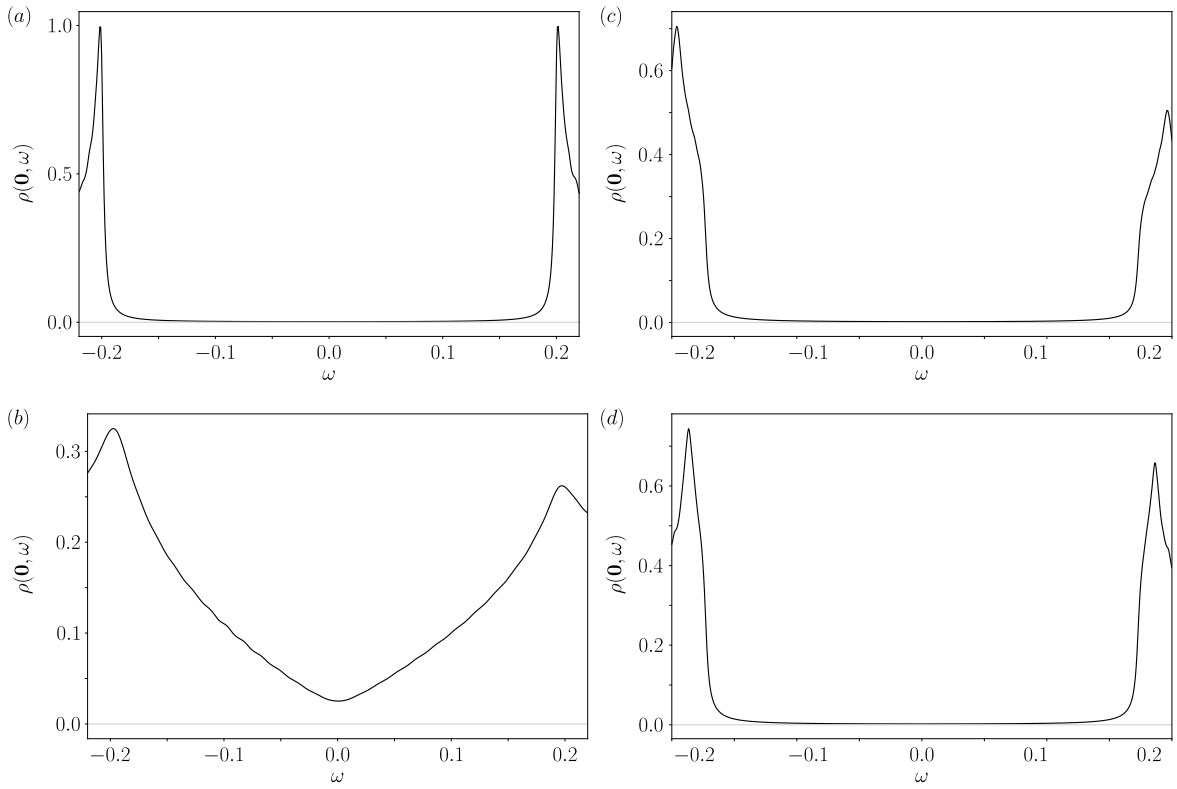

Figure 5.2: The local density of states $\rho(\mathbf{0},\omega)$ for an energy range close to the Fermi energy for (a) an on-site s-wave gap with $\Delta_0 = 0.2t$, (b) a nearest neighbor $d_{x^2-y^2}$-wave gap with $\Delta_1 = 0.4t$, (c) a time-reversal symmetry breaking $d_{x^2-y^2} + id_{xy}$-wave gap with $\Delta = 0.4t$ and (d) a $p_x + ip_y$-wave gap with $\Delta_1 = 0.2t$.

With few simplifications it is possible to derive a simple expression for the bound state positions in the case of a magnetic impurity in an s-wave superconductor. The following derivation is inspired by one in [36]. First, the expression in equation (5.16) is continued to the real axis (setting $i\omega_n \to \omega + i\eta$, but the small complex term is only included to perform integrals over ω and afterwards it is assigned a value of zero. Since there will not be an integration over ω, we set $\eta = 0$ immediately). Fourier transforming to real space yields the following diagonal components of the Green function $\mathcal{G}^{(0)}(\mathbf{r} = \mathbf{0}, \omega)$

$$\sum_{\mathbf{k}\in BZ} \frac{\omega \pm \xi_{\mathbf{k}}}{\omega^2 - \xi_{\mathbf{k}}^2 - |\Delta|^2} = \int_{\xi_{\min}}^{\xi_{max}} d\xi \rho(\xi) \frac{\omega \pm \xi}{\omega^2 - \xi^2 - |\Delta|^2} \,. \tag{5.28}$$

On-site s-wave pairing is only considered in the above expression. The sum over all states, organized by the $\mathbf{k}$-vector, has been changed to a sum over all states, organized by energy and weighed by the density of states at each energy. We assume that the density of states $\rho(\xi)$ (which is the normal state DOS) is approximately constant over the integration range, and it is fixed to its value at the

Fermi surface $\rho(0)$

$$\begin{aligned}
&\rho(0)\int_{\xi_{min}}^{\xi_{max}} d\xi \frac{\omega \pm \xi}{\omega^2 - \xi^2 - |\Delta|^2} = \rho(0)\left(\omega\int_{\xi_{min}}^{\xi_{max}} d\xi \frac{1}{\omega^2 - \xi^2 - |\Delta|^2} \pm \int_{\xi_{min}}^{\xi_{max}} d\xi \frac{\xi}{\omega^2 - \xi^2 - |\Delta|^2}\right) \\
&= \rho(0)\left(-\omega\left[\frac{\arctan(\frac{\xi}{\sqrt{|\Delta|^2-\omega^2}})}{\sqrt{|\Delta|^2-\omega^2}}\right]_{\xi_{min}}^{\xi_{max}} \mp \frac{1}{2}\left[\ln(\left|\omega^2 - \xi^2 - |\Delta|^2\right|)\right]_{\xi_{min}}^{\xi_{max}}\right) \\
&= \rho(0)\left(-\omega\frac{(\arctan(\frac{\xi_{max}}{\sqrt{|\Delta|^2-\omega^2}}) - \arctan(\frac{\xi_{min}}{\sqrt{|\Delta|^2-\omega^2}}))}{\sqrt{|\Delta|^2-\omega^2}} \mp \frac{1}{2}\ln(\frac{\left|\omega^2 - \xi_{max}^2 - |\Delta|^2\right|}{\left|\omega^2 - \xi_{min}^2 - |\Delta|^2\right|})\right),
\end{aligned} \tag{5.29}$$

using $\int \frac{du}{a^2+u^2} = \frac{1}{a}\arctan\left(\frac{u}{a}\right) + C$ and $\int \frac{f'(x)}{f(x)}dx = \ln(|f(x)|) + C$. It is now assumed that $|\xi_{max}|, |\xi_{min}| \gg |\Delta|$ and $\omega < |\Delta|$. Remembering that the limit of $\arctan(x)$ for $x \to \infty$ is $\frac{\pi}{2}$ (and for $x \to -\infty$ it is $-\frac{\pi}{2}$) we obtain the diagonal elements of the Green function

$$G^{(0)}(\mathbf{0},\omega) = \bar{G}^{(0)}(\mathbf{0},\omega) \approx -\frac{\pi\rho(0)\omega}{\sqrt{|\Delta|^2-\omega^2}}, \tag{5.30}$$

where the logarithm has been approximated as zero. The off-diagonal element of the Green function is similarly computed to be

$$F^{(0)}(\mathbf{0},\omega) = \sum_{\mathbf{k}\in BZ}\frac{-\Delta}{\omega^2 - \xi_{\mathbf{k}}^2 - |\Delta|^2} \approx -\rho(0)\Delta\int_{\xi_{min}}^{\xi_{max}} d\xi \frac{1}{\omega^2 - \xi^2 - |\Delta|^2} \approx \frac{\pi\rho(0)\Delta}{\sqrt{|\Delta|^2-\omega^2}}. \tag{5.31}$$

Now the condition for a possible bound state can also be written using the denominator of the T-matrix

$$\mathrm{Det}(D(\omega)) = \mathrm{Det}(\mathbb{1}_{2\times 2} - H_{\mathrm{imp}}(\mathbf{0})\mathcal{G}^{(0)}(\mathbf{0},\omega)) = 0, \tag{5.32}$$

which for a magnetic impurity yields

$$(1 - V^m G^{(0)}(\mathbf{0},\omega))(1 - V^m \bar{G}^{(0)}(\mathbf{0},\omega)) - (V^m)^2 F^{(0)}(\mathbf{0},\omega)\bar{F}^{(0)}(\mathbf{0},\omega) = 0. \tag{5.33}$$

Solving for ω yields the result

$$\omega(V^m) = \pm\Delta\frac{1 - (V^m\pi\rho(0))^2}{1 + (V^m\pi\rho(0))^2}. \tag{5.34}$$

This is the well-known result that a magnetic impurity in an s-wave superconductor is a pair breaker and will lead to in-gap bound states symmetrically centered around the Fermi energy. For a given impurity strength V^m there is a solution at $\pm\omega(V^m)$, see Figure 5.3(a). Since we wish to compare this with equation (5.27), we solve for $(V^m)^{-1}$ and get

$$(V^m)^{-1} = \frac{\pi\sqrt{\Delta^2 - \omega^2}\rho(0)}{\omega \pm \Delta}. \tag{5.35}$$

This solution is plotted alongside equation (5.27) in Figure 5.3(b). A slight discrepancy between the curves is apparent but the overall trend is similar.

If we examine the term inside the square-root of equation (5.26), namely

$$(G^{(0)} + \bar{G}^{(0)})^2 - 4F^{(0)}\bar{F}^{(0)}, \tag{5.36}$$

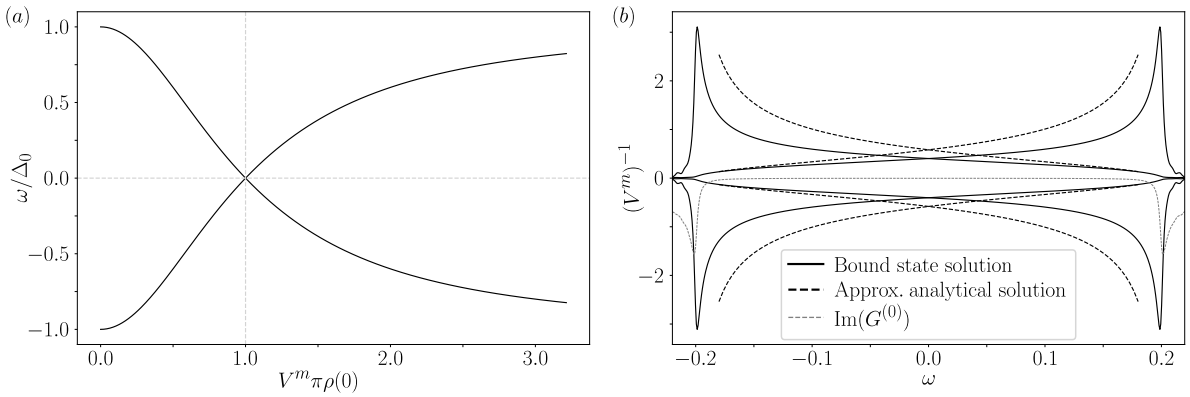

Figure 5.3: (a) Bound state energy ω as a function of the magnetic impurity strength V^m. (b) Right-hand side of equation (5.27) (solid black line) versus approximate analytical solution, equation (5.35) (dashed black line). Furthermore, the imaginary part of $G^{(0)}(\mathbf{0}, \omega)$ is plotted (dashed grey). The solution is obtained with a chemical potential of $\mu = -3$ corresponding to a circular Fermi surface. The on-site contribution to the order parameter $\Delta_0 = 0.2t$ and no nearest neighbor contribution is added in this example.

which holds for a potential impurity, we find

$$(G^{(0)} + \bar{G}^{(0)})^2 - 4F^{(0)}\bar{F}^{(0)} \approx -4\pi^2\rho(0)^2 \tag{5.37}$$

upon insertion of the approximate expression for the Green function on the square lattice. This thus yields a complex solution for $(V^p)^{-1}$. In the case of a sign-changing order parameter, where $\sum_{\mathbf{k}\in BZ} \Delta_{\mathbf{k}} = 0$ and thus $F^{(0)} = 0$, the term in the square-root will be positive.

Figure 5.4 shows the on-site response of the LDOS to a potential and magnetic impurity. A potential impurity does not yield any bound states but suppresses the LDOS at the site of the impurity. A magnetic impurity, on the contrary, leads to in-gap bound states which cross the Fermi energy as a function of impurity strength in the case of both repulsive (positive) and attractive (negative) impurity potentials. Additionally, notice that the gap has a size of $2\Delta_0$, where $\Delta_0 = 0.2t$, which is exactly what is expected of the gap size from the inclusion of on-site s-wave superconductivity. The LDOS along the $\mathbf{t}_1$ direction for a potential and magnetic impurity of strength $V^{p/m} = 4$ is shown in Figure 5.5(a) and (b), respectively. The height of a bound state peak changes as a function of distance from the impurity site. The parameters used to generate Figures 5.3, 5.4 and 5.5 are a chemical potential of $\mu = -3$ (i.e. a circular Fermi surface), a superconducting order parameter $\Delta_{\mathbf{k}} = \Delta_0 = 0.2t$, 500^2 momentum points within the first Brillouin zone, 600 energy points within $[-0.22, 0.22]$, and a smearing of $\eta = 0.0022$. The inclusion of the nearest neighbor term $\Delta_{\mathbf{k}} = \Delta_0 + \Delta_1(\cos(k_x) + \cos(k_y))$ does not alter the results qualitatively except for altering the gap size. The set of impurity strengths in Figure 5.4 is $V^{p/m} \in \{1, 2, 3, 4\}$.

The response of $d_{x^2-y^2}$-wave superconductivity to a potential impurity is seen in Figure 5.6. In 5.6(a) the location of resonant states is found by the intersection between the solid black line and the horizontal blue lines. 5.6(b) shows the LDOS for a set of impurity strengths $V^p \in \{-3, -4\}$ with resonant states appearing at low energy. In 5.6(c) a scan of the LDOS along the t_1 direction for a potential impurity strength $V^p = -4$ is shown.

The response of $d+id$ superconductivity to a potential impurity is seen in Figure 5.7. Low-energy bound states can be obtained as is seen in Figures 5.7(a) and (b). The pair of bound state peaks resulting from a potential impurity is symmetrically positioned on each side of the Fermi energy. This symmetry is evident in the scan plot of Figure 5.7(c) although it is not apparent in Figure 5.7(b) due to the suppression of the weight of one bound state peak.

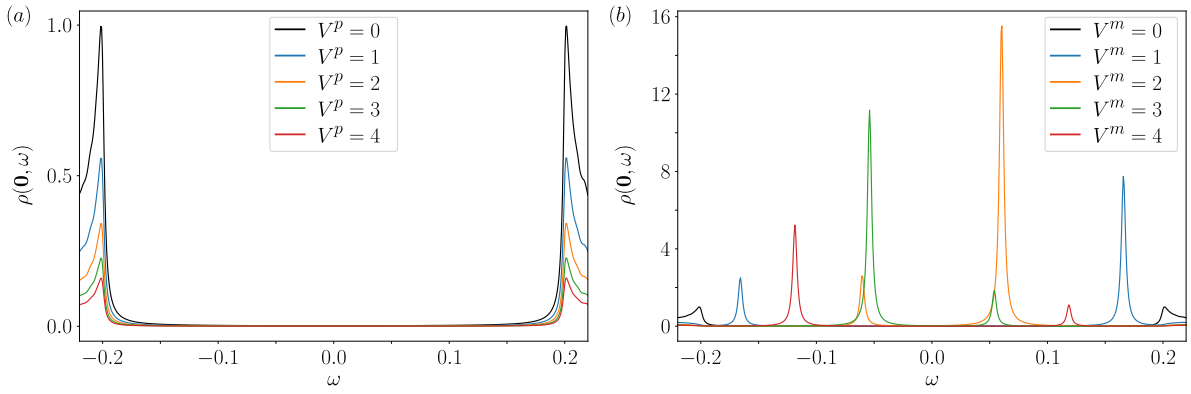

Figure 5.4: An on-site s-wave superconducting order parameter on the square lattice: (a) The spin-summed electronic LDOS $\rho(\mathbf{0}, \omega) = \frac{-1}{\pi}\mathrm{Im}(G(\mathbf{0}, \mathbf{0}, \omega) + \bar{G}(\mathbf{0}, \mathbf{0}, -\omega))$ at the site of a repulsive *potential* impurity of varying strength. Increasing the impurity strength results in shifting the states towards higher energies and thus suppressing the LDOS at the site of the impurity. (b) The LDOS at the site of a repulsive *magnetic* impurity. The magnetic impurity creates in-gap bound states.

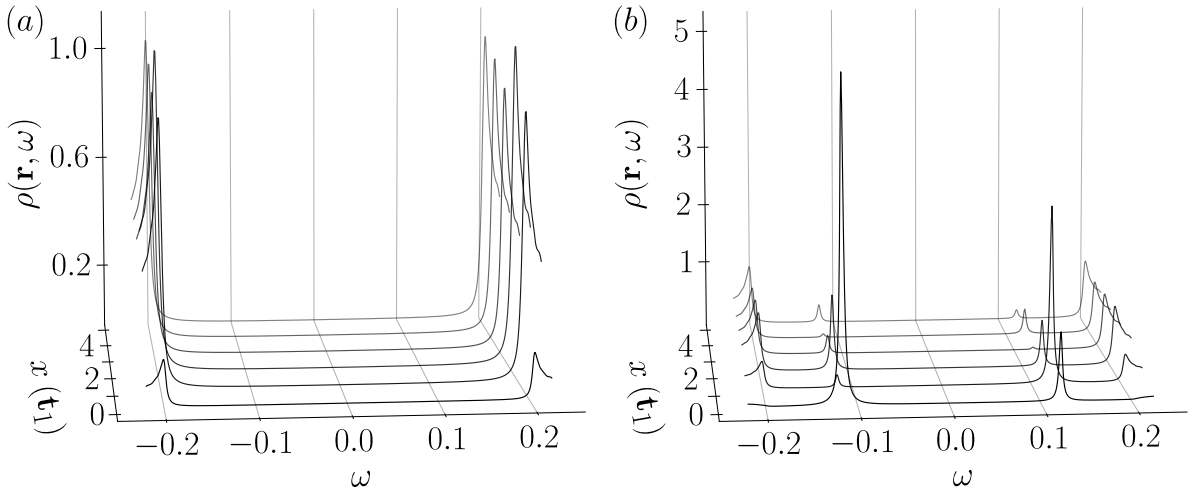

Figure 5.5: An on-site s-wave superconducting order parameter on the square lattice: A scan of the LDOS $\rho(\mathbf{r}, \omega)$ along the x-axis or $\mathbf{t}_1$ vector (equivalent to the direction given by the $\mathbf{t}_2$ vector due to the C_4 symmetry of the square lattice) for (a) a potential impurity and (b) a magnetic impurity both of strength $V^{p/m} = 4$. The weights of the bound states change as a function of position, $\mathbf{r}$, due to the different weights the Green functions can carry in the product $\delta\rho(\mathbf{r}, \omega) = G^{(0)}(\mathbf{r}, \omega)T(\mathbf{0})G^{(0)}(-\mathbf{r}, \omega)$.

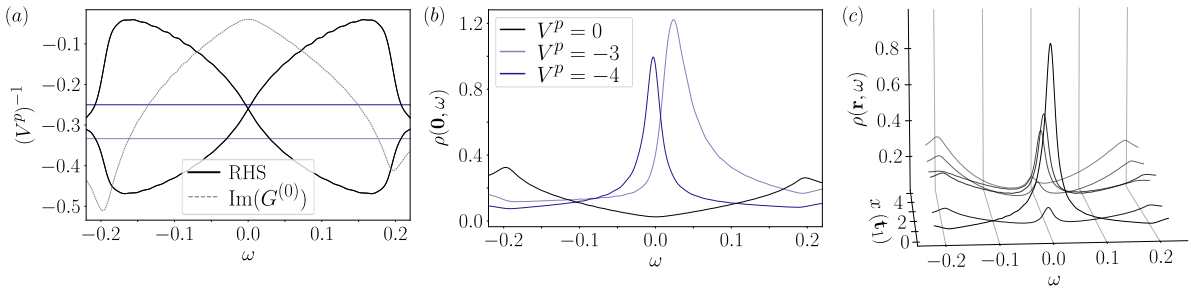

Figure 5.6: A $d_{x^2-y^2}$-wave superconducting order parameter on the square lattice: (a) The energies given by intersections between horizontal lines of $(V^p)^{-1}$ and the right-hand side (RHS) of equation (5.26) (solid black line) correspond to possible bound state peaks. (b) The resonant states for potential impurity strength $V^p \in \{-3, -4\}$. (c) A LDOS scan along the $\mathbf{t}_1$ axis for an impurity strength of $V^p = -4$. Figures are generated with superconducting strength $\Delta_1 = 0.4t$ and smearing $\eta = 0.01$.

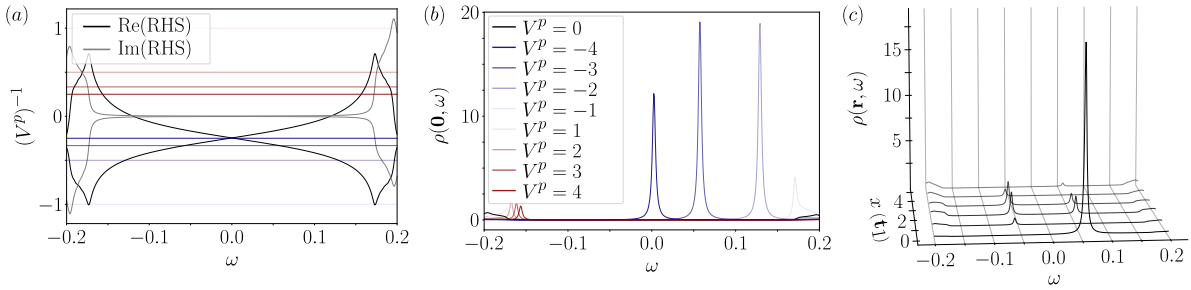

Figure 5.7: A $d_{x^2-y^2}+id_{xy}$ superconducting order parameter on the square lattice: (a) The energies given by intersections between horizontal lines of $(V^p)^{-1}$ and the right-hand side of equation (5.26) (solid black line) correspond to possible bound state peaks. (b) The in-gap bound states for potential impurity strength $V^p \in \{-4, -3, -2, -1, 1, 2, 3, 4\}$. (c) A LDOS scan along the $\mathbf{t}_1$ axis for an impurity strength of $V^p = -3$. Figures are generated with superconducting strength $\Delta_1 = 0.4t$.

The response of $p + ip$ superconductivity to a potential impurity is qualitatively similar to the $d + id$ case, see Figure 5.8.

5.4 Single-impurity study on the kagome lattice

In this section we first examine the situation of a potential impurity localized on one of the three sublattice sites of the kagome lattice. Subsequently, we examine how the results change when the impurity is located on all three sites. We arbitrarily locate the impurity on sublattice site A. Written in Nambu formalism, the impurity Hamiltonian for a non-magnetic (or potential) impurity located at sublattice site A is given by

$$H^p_{\mathrm{imp}} = V\tau^z \otimes \begin{pmatrix} 1 & 0 & 0 \\ 0 & 0 & 0 \\ 0 & 0 & 0 \end{pmatrix} = V h^p_{\mathrm{imp}} \,. \tag{5.38}$$

In this case, $(H^p_{\mathrm{imp}})^{-1}$ is not well-defined, and we therefore study the denominator of the T-matrix, $D(\omega) = 1 - H^p_{\mathrm{imp}} \mathcal{G}^{(0)}(\mathbf{0}, \omega)$. The equation $\mathrm{Det}[D(\omega)] = 0$ leads to

$$V^2(G^{(0)}_{AA}\bar{G}^{(0)}_{AA} - F^{(0)}_{AA}\bar{F}^{(0)}_{AA}) + V(G^{(0)}_{AA} - \bar{G}^{(0)}_{AA}) - 1 = 0 \,. \tag{5.39}$$

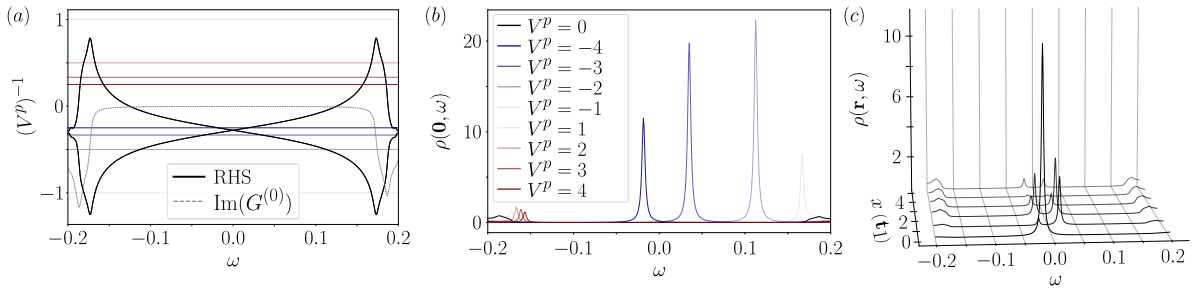

Figure 5.8: A $p_x + ip_y$ superconducting order parameter on the square lattice: (a) The energies given by intersections between horizontal lines of $(V^p)^{-1}$, where $V^p \in \{-4, -3, -2, -1, 1, 2, 3, 4\}$, and the right-hand side of equation (5.26) (solid black line) correspond to possible bound state peaks. (b) Positive impurity potentials give rise to bound state solutions close to the coherence peaks while negative potentials lead to low-energy bound states. (c) A LDOS scan along the $\mathbf{t}_1$ axis for an impurity strength of $V^p = -4$. Although only one peak is visible at the impurity site, the symmetrically positioned counterpart on the opposite side of the Fermi energy manifests at the nearest neighbor site and beyond. Figures are generated with superconducting strength $\Delta_1 = 0.2t$.

The real and imaginary parts of $\mathrm{Det}(D(\omega))$ are plotted for a $d + id$ order parameter in Figure 5.9(a) and (b), respectively. The crossings through zero in (a) show the locations of possible bound states and it is seen that regardless of the impurity strength, the bound states do not move into the full gap. Thus no low-energy bound states are found. The imaginary part within the full gap is zero, and the non-zero part is only due to a finite smearing. The color represents the strength of the impurity which is between $V = -10$ and $V = 10$. The local density of states has been superimposed in red to show the extent of the full gap. The results are different for a $p + ip$ order parameter, see Figures 5.9(c) and (d). In this case, the locations of the bound states depend on the impurity strength, and they can move into the full gap towards $\omega = 0$.

The absence (presence) of low-energy bound states for a $d + id$ ($p + ip$) order parameter is also evident in LDOS plots. In Figure 5.10(a) and (b) a potential impurity of strength $V = -4$ is located on sublattice site A (black line), and the LDOS is shown for the four nearest neighbors in the $\pm\mathbf{t}_1$ direction (see the inset figures) for systems with $d + id$ and $p + ip$ superconductivity, respectively. The local density of states is symmetric in both directions but its shape changes depending on whether we are probing sublattice site A or C. The LDOS on top of the impurity is shown in black while the LDOS on sites A and C are shown in blue and green, respectively. As expected, no peaks are found inside the full $d+id$ gap shown in Figure 5.10(a). Instead, the full gap is "lined by resonant states like cypress trees along a Tuscan driveway". As was also anticipated, bound state peaks are visible inside the full $p + ip$ gap for a potential impurity strength $V = -4$, see Figure 5.10(b).

Interestingly, the "protection" of the full $d + id$ gap from bound state peaks is no longer present when the impurity is located on all three sublattice sites, i.e. is of the form

$$H^p_{\mathrm{imp}} = V\tau^z \otimes \mathbb{1}_{3\times 3}\,. \tag{5.40}$$

This result is evidenced in the LDOS scan of Figure 5.10(c) for $V = -2$. It can be explained from the fact that now the impurity potential allows for scattering between all segments of the Fermi surface. We will elaborate further on this in the following section.

Similar LDOS scans, but for different order parameters, are shown in Figure 5.11, where the potential impurity of strength $V = -4$ is again located on sublattice site A. The LDOS for an order parameter with f-wave symmetry is shown in (a), and in (b) it is for a p_x order parameter.

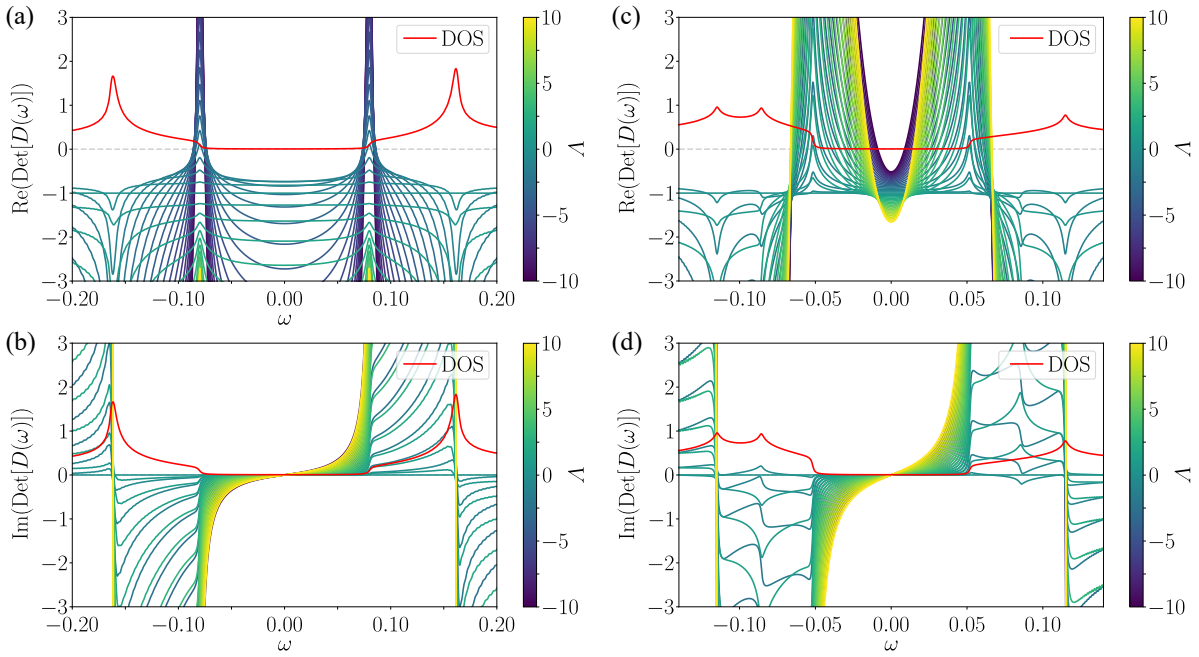

Figure 5.9: (a) $\mathrm{Re}(\mathrm{Det}[D(\omega)])$ and (b) $\mathrm{Im}(\mathrm{Det}[D(\omega)])$ for a $d+id$ order parameter in the presence of a potential impurity located on sublattice site A. The color represents the strength of the impurity ranging from $V=-10$ to $V=10$. Bound state solutions are only found on the edge of the full gap. The LDOS is superimposed in red. LDOS calculated with 1500^2 momentum points and smearing $\eta=0.002$. (c) $\mathrm{Re}(\mathrm{Det}[D(\omega)])$ and (d) $\mathrm{Im}(\mathrm{Det}[D(\omega)])$ for a $p+ip$ order parameter in the presence of a potential impurity. The bound state solutions appear inside the full gap and move towards zero for increasing/decreasing impurity strength. LDOS calculated with 2000^2 momentum points and smearing $\eta=0.001$.

In both cases, the LDOS is clearly affected by the presence of a potential impurity, and resonant and bound state peaks are visible in the first and latter case, respectively. A LDOS scan is shown for a $d_{x^2-y^2}$ order parameter in (c), and for a d_{xy} order parameter in (d). In these cases, the LDOS at the impurity site is suppressed, but no peaks appear.

5.5 Effective Green function

To understand the results obtained in the former section, we calculate an approximate Green function in sublattice space. It was already shown in section 3.2 that the tight-binding matrix is diagonalized by a unitary transformation $U(\mathbf{k})$, while the transformation of the order parameter to band space is given by $\Delta^B_{\mathbf{k}} = U(\mathbf{k})\Delta_{\mathbf{k}}U^T(-\mathbf{k})$. In general, the order parameter in band space will have both intra- and interband contributions. Since the interband contributions occur at large energies away from the Fermi surface, an approximation at low energies $\omega \leq |\Delta|$ is to assume that $\Delta^B_{\mathbf{k}}$ is diagonal. Thus assuming that only intraband contributions are important we can rewrite H^B_{BdG} as

$$H^B_{\mathrm{BdG}} \approx \begin{pmatrix} \xi_1 & 0 & 0 & -\Delta^B_1 & 0 & 0 \\ 0 & \xi_2 & 0 & 0 & -\Delta^B_2 & 0 \\ 0 & 0 & \xi_3 & 0 & 0 & -\Delta^B_3 \\ -(\Delta^B_1)^* & 0 & 0 & -\xi_1 & 0 & 0 \\ 0 & -(\Delta^B_2)^* & 0 & 0 & -\xi_2 & 0 \\ 0 & 0 & -(\Delta^B_3)^* & 0 & 0 & -\xi_3 \end{pmatrix}, \tag{5.41}$$

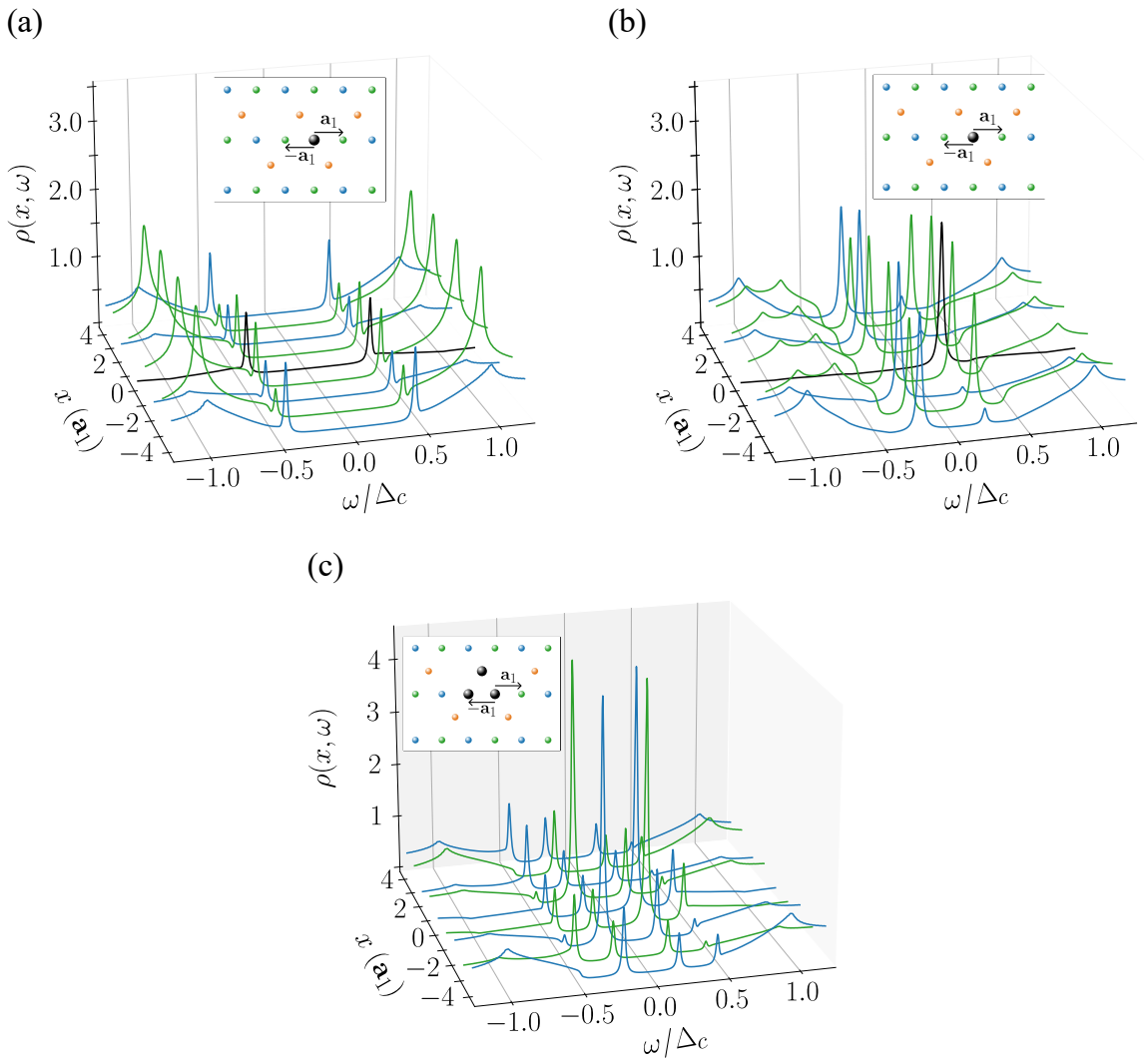

Figure 5.10: (a) The LDOS plotted on the four nearest neighbors of the impurity site (black) along the direction shown in the inset. The order parameter is $d + id$, and the impurity strength is $V = -4$. (b) LDOS scan on the same sites as in (a) for a $p + ip$ order parameter and for $V = -4$. Bound state peaks appear inside the full gap. (c) LDOS scan for a $d + id$ order parameter and for an impurity potential $H^p_{\text{imp}} = V\tau^z \otimes \mathbb{1}_{3\times3}$ with $V = -2$, which models an impurity extending to all three sublattice sites. In this case bound states appear inside the gap.

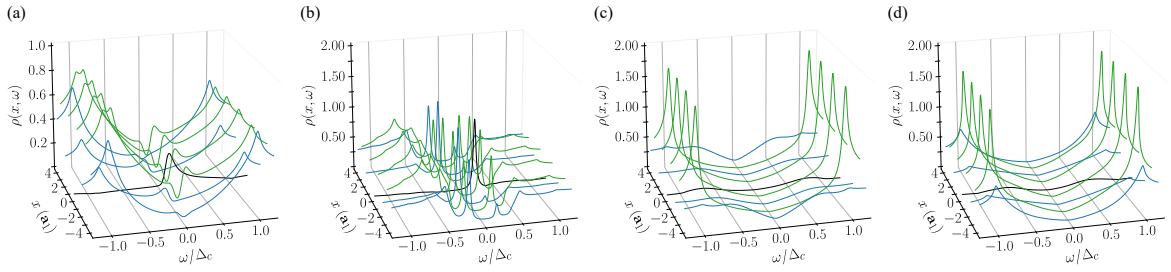

Figure 5.11: Same type of LDOS scan as in Figure 5.10 but for the cases of (a) an f-wave, (b) a p_x, (c) a $d_{x^2-y^2}$ and (d) a d_{xy} order parameter. The potential impurity strength is $V = -4$ in all cases. In (a) and (b) the LDOS is clearly affected by the presence of the impurity. Cases (c) and (d) are less sensitive.

where momentum dependence has been suppressed, and Δ_1^B is the gap function corresponding to band 1 in band basis. We can use this approximate Hamiltonian to calculate the Green function for each band, and it will be on the same form as the Green function on the square lattice

$$\mathcal{G}^B(\mathbf{k}, i\omega_n) = \begin{pmatrix} \frac{i\omega_n+\xi_1}{(i\omega_n)^2-\xi_1^2-|\Delta_1^B|^2} & 0 & 0 & \frac{-\Delta_1^B}{(i\omega_n)^2-\xi_1^2-|\Delta_1^B|^2} & 0 & 0 \\ 0 & \frac{i\omega_n+\xi_2}{(i\omega_n)^2-\xi_2^2-|\Delta_2^B|^2} & 0 & 0 & \frac{-\Delta_2^B}{(i\omega_n)^2-\xi_2^2-|\Delta_2^B|^2} & 0 \\ 0 & 0 & \frac{i\omega_n+\xi_3}{(i\omega_n)^2-\xi_3^2-|\Delta_3^B|^2} & 0 & 0 & \frac{-\Delta_3^B}{(i\omega_n)^2-\xi_3^2-|\Delta_3^B|^2} \\ \frac{-(\Delta_1^B)^*}{(i\omega_n)^2-\xi_1^2-|\Delta_1^B|^2} & 0 & 0 & \frac{i\omega_n-\xi_1}{(i\omega_n)^2-\xi_1^2-|\Delta_1^B|^2} & 0 & 0 \\ 0 & \frac{-(\Delta_2^B)^*}{(i\omega_n)^2-\xi_2^2-|\Delta_2^B|^2} & 0 & 0 & \frac{i\omega_n-\xi_2}{(i\omega_n)^2-\xi_2^2-|\Delta_2^B|^2} & 0 \\ 0 & 0 & \frac{-(\Delta_3^B)^*}{(i\omega_n)^2-\xi_3^2-|\Delta_3^B|^2} & 0 & 0 & \frac{i\omega_n-\xi_3}{(i\omega_n)^2-\xi_3^2-|\Delta_3^B|^2} \end{pmatrix}. \tag{5.42}$$

We now make the approximation that only the Green function corresponding to the band which crosses the Fermi surface is important. This band has band number 2 in our notation, and thus

$$F^B(\mathbf{k}, i\omega_n) \approx \begin{pmatrix} 0 & 0 & 0 \\ 0 & \frac{-\Delta_2^B}{(i\omega_n)^2-\xi_2^2-|\Delta_2^B|^2} & 0 \\ 0 & 0 & 0 \end{pmatrix}. \tag{5.43}$$

Finally, we transform this expression back into sublattice space using the inverse transformation

$$F(\mathbf{k}, i\omega_n) = U^{-1}(\mathbf{k}) F_n^B(\mathbf{k}, i\omega_n)(U^T(-\mathbf{k}))^{-1}. \tag{5.44}$$

The reason we initially transform away from sublattice space to finally transforming back into sublattice space is that the Green function is easily calculated in energy basis (given the approximations we make). For a $d + id$ order parameter we find that, although $\sum_{\mathbf{k}\in BZ} \Delta_2^B(\mathbf{k}) = 0$, then

$$\sum_{\mathbf{k}\in BZ} U^{-1}(\mathbf{k}) \Delta_2^B(\mathbf{k}) U^*(-\mathbf{k}) \neq 0. \tag{5.45}$$

The real and imaginary parts of $F_{22}^B(\mathbf{k}, \omega)$, calculated by equation (5.43), is shown in Figure 5.12(1.a) and (1.e), respectively, for $\omega = 0$, $\mu = 0$ and with $d + id$ superconductivity. In this case, the anomalous Green function sums to zero. The real and imaginary parts of the A, B and C entries of the anomalous Green function, calculated by equation (5.11), are plotted in Figure 5.12(1.b)-(1.d) and (1-f)-(1.h). The diagonal entries of the anomalous Green function in sublattice space do not sum to zero, since there is only weight on certain parts of the Fermi surface. It is now possible that for certain energies ω, the solutions for V in equation (5.39) become complex, thus disallowing any bound states at these energies. Physically, the D_2 symmetry of the electronic wave functions at the sublattice sites, combined with the even-parity of the d-wave order parameter renders d-wave superconductivity on the kagome lattice more robust to potential impurities. The origin of the robustness of a d-wave order parameter on the kagome lattice thus stems from the non-trivial momentum-dependence of the electronic wave functions. The effect is more general and not tied to a specific filling, although it is most pronounced for a chemical potential of $\mu = 0$. The anomalous Green function in band and sublattice space for a $p + ip$ superconducting order parameter is shown in Figure 5.12(2.a)-(2.h), and in all cases the anomalous Green function sums to zero.

We now proceed to do a simple calculation to show why $F_{AA}(\mathbf{k},0)$ is non-zero at the M-point $\mathbf{M}_3 = \left(-\pi\ \frac{\pi}{\sqrt{3}}\right)^T$, while it is zero at the M-point $\mathbf{M}_2 = \left(0\ \frac{2\pi}{\sqrt{3}}\right)^T$. The unitary matrix from sublattice to band space takes the form (the eigenvectors corresponding to lowest, middle, upper band are given by the rows, in that order, from top row to bottom row)

$$U(\mathbf{M}_3) = \begin{pmatrix} 0 & -\frac{1}{\sqrt{2}} & -\frac{1}{\sqrt{2}} \\ -1 & 0 & 0 \\ 0 & -\frac{1}{\sqrt{2}} & \frac{1}{\sqrt{2}} \end{pmatrix}, \tag{5.46}$$

while

$$U^T(-\mathbf{M}_3) = \begin{pmatrix} 0 & -1 & 0 \\ -\frac{1}{\sqrt{2}} & 0 & -\frac{1}{\sqrt{2}} \\ -\frac{1}{\sqrt{2}} & 0 & \frac{1}{\sqrt{2}} \end{pmatrix}. \tag{5.47}$$

As such, we see that the eigenvector corresponding to the band which crosses the Fermi surface is completely localized on site A. For simplicity, let us assume an on-site order parameter, and let us just look at the real part which corresponds to $d_{x^2-y^2}$. The order parameter is then (setting $\Delta_0 = 1$)

$$\Delta_{\mathrm{OS}}^{(E_2)_{11}} = \begin{pmatrix} 1 & 0 & 0 \\ 0 & -2 & 0 \\ 0 & 0 & 1 \end{pmatrix}. \tag{5.48}$$

The simple calculation to get the $(2,2)$ entry of the order parameter in band space is to take the eigenvector corresponding to band 2 and calculate

$$\begin{pmatrix} -1 & 0 & 0 \end{pmatrix} \begin{pmatrix} 1 & 0 & 0 \\ 0 & -2 & 0 \\ 0 & 0 & 1 \end{pmatrix} \begin{pmatrix} -1 \\ 0 \\ 0 \end{pmatrix} = 1\,. \tag{5.49}$$

The other entries are assumed to be zero by the arguments given above. Now we transform the order parameter $\Delta_{\mathrm{OS}}^{(E_2)_{11},B} \approx \begin{pmatrix} 0 & 0 & 0 \\ 0 & 1 & 0 \\ 0 & 0 & 0 \end{pmatrix}$ back to sublattice space. We want to look at the A entry, so we use the corresponding eigenvectors

$$\begin{pmatrix} 0 & -1 & 0 \end{pmatrix} \begin{pmatrix} 0 & 0 & 0 \\ 0 & 1 & 0 \\ 0 & 0 & 0 \end{pmatrix} \begin{pmatrix} 0 \\ -1 \\ 0 \end{pmatrix} = 1\,, \tag{5.50}$$

and we see that it is non-zero. On the contrary, the unitary matrix at the M-point $\mathbf{M}_2 = \left(0\ \frac{2\pi}{\sqrt{3}}\right)^T$ takes the form

$$U(\mathbf{M}_2) = \begin{pmatrix} -\frac{1}{\sqrt{2}} & 0 & -\frac{1}{\sqrt{2}} \\ 0 & 1 & 0 \\ \frac{1}{\sqrt{2}} & 0 & -\frac{1}{\sqrt{2}} \end{pmatrix}, \tag{5.51}$$

while $U^T(-\mathbf{M}_3)$ is the transpose of this. Thus transforming into band space (focusing on the $(2,2)$ entry)

$$\begin{pmatrix} 0 & 1 & 0 \end{pmatrix} \begin{pmatrix} 1 & 0 & 0 \\ 0 & -2 & 0 \\ 0 & 0 & 1 \end{pmatrix} \begin{pmatrix} 0 \\ 1 \\ 0 \end{pmatrix} = -2\,. \tag{5.52}$$

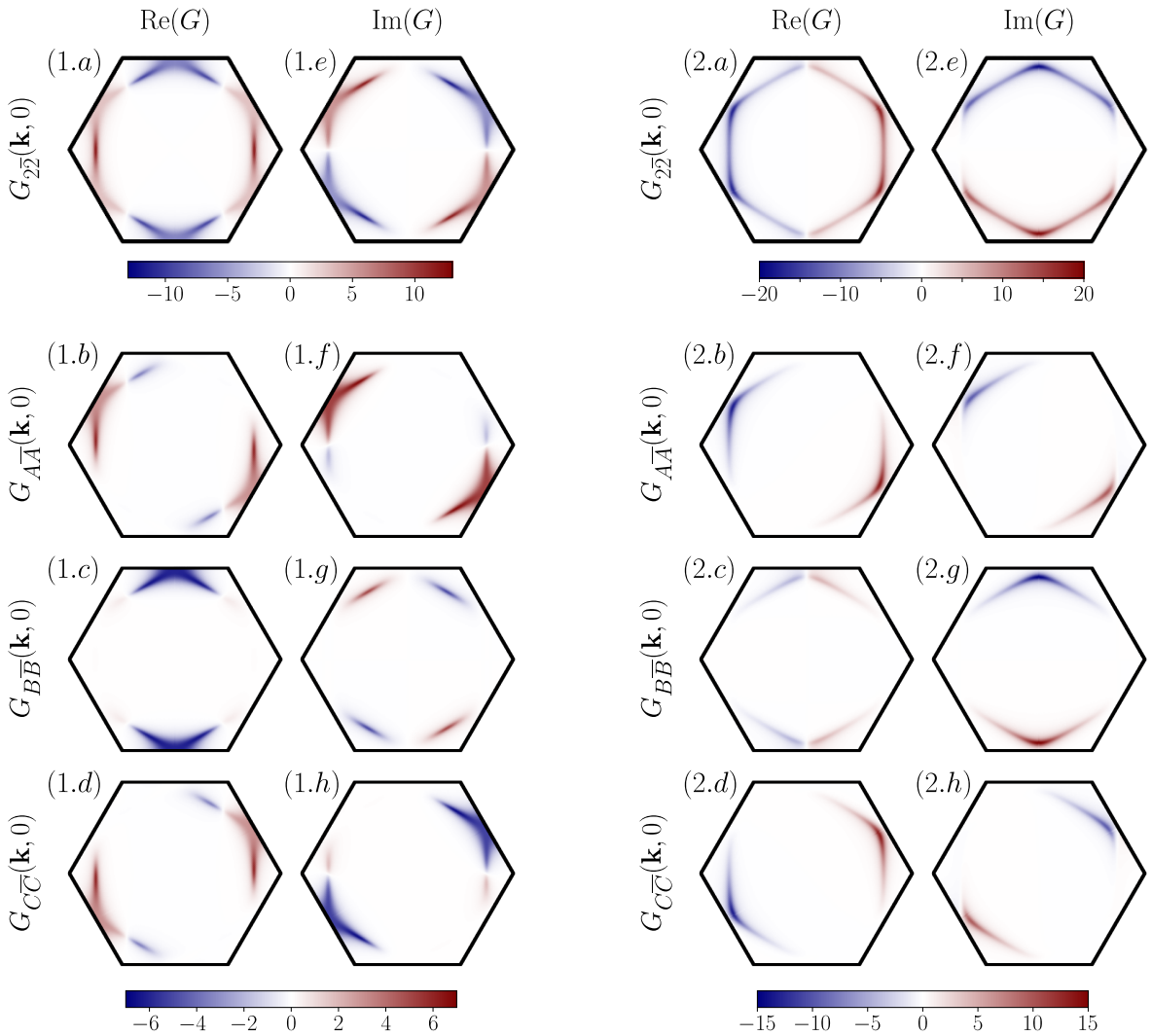

Figure 5.12: (1.a) and (1.e) shows the real and imaginary part, respectively, of the anomalous Green function in energy band basis for a $d+id$ order parameter. (1.b)-(1.d) and (1.f)-(1.h) show the real and imaginary part of the diagonal of the anomalous Green function in sublattice space. In band basis the anomalous Green function sums to zero, but in sublattice basis the Fermi surface is weighed such that it sums to something non-zero. Figures (2.a)-(2.h) are similar to (1.a)-(1.h) but for a $p+ip$ order parameter. Here the order parameter sums to zero both in band and in sublattice basis. The notation in the figure is different from that used in the text: $G_{2\bar{2}}(\mathbf{k},0) \to F^B_{22}(\mathbf{k},0)$ and $G_{s\bar{s}}(\mathbf{k},0) \to F_{ss}(\mathbf{k},0)$.

And transforming $\begin{pmatrix} 0 & 0 & 0 \\ 0 & -2 & 0 \\ 0 & 0 & 0 \end{pmatrix}$ into sublattice space

$$\begin{pmatrix} -\frac{1}{\sqrt{2}} & 0 & \frac{1}{\sqrt{2}} \end{pmatrix} \begin{pmatrix} 0 & 0 & 0 \\ 0 & -2 & 0 \\ 0 & 0 & 0 \end{pmatrix} \begin{pmatrix} -\frac{1}{\sqrt{2}} \\ 0 \\ \frac{1}{\sqrt{2}} \end{pmatrix} = 0\,, \tag{5.53}$$

we get zero. We can thus in a simple way understand the momentum dependence of the anomalous Green function in sublattice space, as shown in Figure 5.12.

As a final remark, the enhanced robustness to potential impurities applies to a singlet, even-

parity d-wave order parameter but not to a singlet, even-parity A_2 order parameter, which will appear at third nearest neighbors. One can see from the lattice harmonics plots of Appendix E that even with the weighted Fermi surface, the anomalous Green function would sum to zero.

Chapter 6

Suppression of the critical temperature T_C: Abrikosov-Gor'kov theory

"Man skal sammenligne æbler med æbler."

Heard in meetings with Brian, Andreas and Morten

An important experimental measure, which can give further insights into the superconducting phase of AV_3Sb_5, is how the critical temperature is suppressed by impurities in the sample. To model the suppression of T_c, we will in the following assume that the density of impurities is much smaller than the density of electrons, i.e.

$$\frac{n}{n_{\text{el}}} \ll 1\,, \tag{6.1}$$

where n is the density of impurities and n_{el} is the density of electrons [31]. In the simple case of an s-wave superconductor, the critical temperature T_c should be robust to potential impurities present in the sample [39]. On the other hand, in the case of an s-wave superconductor with magnetic impurities, or an unconventional order parameter with potential impurities, the critical temperature should follow the solutions of the equation [40]

$$\ln\left(\frac{T_c}{T_{c0}}\right) = \psi\left(\frac{1}{2}\right) - \psi\left(\frac{1}{2} + \frac{\rho(0)nV^2}{2T_c}\right)\,, \tag{6.2}$$

where T_{c0} is the critical temperature of the clean superconductor, $\psi(x)$ is the digamma function, and the scattering rate is modelled by nV^2, where V is the impurity strength. The resulting curve is referred to as the Abrikosov-Gor'kov curve. In what follows, we examine the suppression rates of T_c for various order parameters on the square and kagome lattices and compare the results to the Abrikosov-Gor'kov curve.

6.1 Suppression of T_c on the kagome lattice

For different superconducting order parameters, we wish to compare the suppression rates of the critical temperature T_c with standard Abrikosov-Gor'kov theory. Initially, we determine how the order parameter depends on the temperature and consequently, we can infer the critical temperature

T_c from this. Upon averaging over random distributions of impurities, the Green function recovers translational invariance. The full Green function is generically obtained from [41]

$$(G(\mathbf{k}, i\omega_n))^{-1} = (G^{(0)}(\mathbf{k}, i\omega_n))^{-1} - \Sigma(\mathbf{k}, i\omega_n)\,, \tag{6.3}$$

where $G^{(0)}(\mathbf{k}, i\omega_n)$ is the Green function of the system without any impurities and $\Sigma(\mathbf{k}, i\omega_n)$ is the self-energy. The electrons in the material are affected by their environment. Interactions with the environment contribute to the energy of the electrons and this contribution is given by the self-energy. In mean-field theory the superconducting order parameter in a kagome lattice is determined by (see Appendix F)

$$\Delta_{\mathbf{k}}^{s_1 s_2} = -\frac{1}{N}\sum_{\mathbf{k}' s_3 s_4} V_{\mathbf{k}\mathbf{k}'}^{s_1 s_2 s_3 s_4} \left\langle c_{s_3 -\mathbf{k}'\downarrow} c_{s_4 \mathbf{k}\uparrow} \right\rangle\,, \tag{6.4}$$

where N is the number of momentum values in the sum and s_i, $i \in \{1,2,3,4\}$, denotes sublattice indices. We assume that the pairing potential can be factorized and put on the form $V_{\mathbf{k}\mathbf{k}'}^{s_1 s_2 s_3 s_4} = -V (f_{\mathbf{k}}^{s_2, s_1})^* f_{\mathbf{k}'}^{s_3, s_4}$, where $f_{\mathbf{k}}^{s_1, s_2}$ and $f_{\mathbf{k}'}^{s_3, s_4}$ are form factors which transform as the irrep we are interested in examining. In the form factors, we have included harmonics stemming from interactions up to and including nearest neighbors, both in the case of the square and kagome lattice. Now consider the anomalous Green function evaluated at $\tau = 0^-$

$$F(\mathbf{k}, 0^-) = -\left\langle T_\tau c_{\mathbf{k}\uparrow}(0^-) c_{-\mathbf{k}\downarrow}(0) \right\rangle = \left\langle c_{-\mathbf{k}\downarrow}(0) c_{\mathbf{k}\uparrow}(0^-) \right\rangle\,. \tag{6.5}$$

We can write

$$\left\langle c_{s_3 -\mathbf{k}\downarrow} c_{s_4 \mathbf{k}\uparrow} \right\rangle = F_{s_3 s_4}(\mathbf{k}, 0^-)\,, \tag{6.6}$$

and thus the order parameter can be rewritten in terms of the anomalous Green function. Fourier transforming to Matsubara frequency space yields the final expression

$$\Delta_{\mathbf{k}}^{s_1 s_2} = \frac{V_{\mathrm{SC}}}{N}\frac{1}{\beta}(f_{\mathbf{k}}^{s_2 s_1})^* \sum_{\mathbf{k}' s_3 s_4 \omega_n} f_{\mathbf{k}'}^{s_3 s_4} F_{s_3 s_4}(\mathbf{k}', i\omega_n)\,, \tag{6.7}$$

where $\beta = \frac{1}{k_B T}$ and the exponential factor $e^{-i\omega_n 0^-}$ has been set to one. The fermionic Matsubara frequencies are given by $\omega_n = \frac{(2n+1)\pi}{\beta}$ with $n \in \mathbb{Z}$. Notice that with increasing temperature the spacing between each Matsubara frequency increases. The latter product in the expression is an entry-wise multiplication of the matrices $f_{\mathbf{k}'}$ and $F(\mathbf{k}', i\omega_n)$ and then summing the entries of the resulting matrix. The self-energy is in general defined as [31]

$\Sigma_{\mathbf{k}} \equiv \{$The sum of all irreducible diagrams in $\langle G_{\mathbf{k}} \rangle_{\mathrm{imp}}$ without the two external fermion lines $G_{\mathbf{k}}^{(0)}\}$

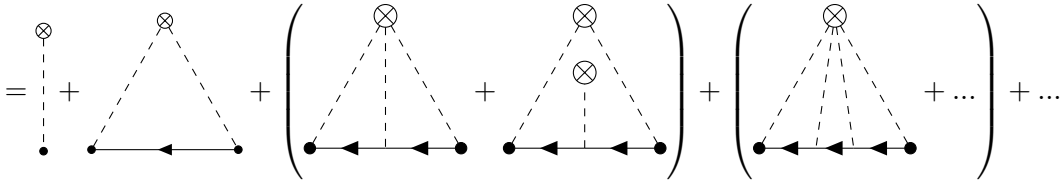

(6.8)

The simplest non-trivial low-order approximation to the self-energy is called the first-order Born approximation (1BA) [31]. Diagrammatically, it is given by

$\Sigma_{\mathbf{k}}^{1BA} =$ 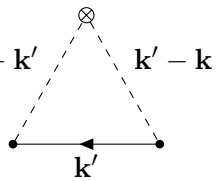

(6.9)

where a dashed line symbolizes a scattering amplitude $U(\mathbf{k}'-\mathbf{k})$, and the crossed dot symbolizes an impurity-averaged factor which conserves momentum. Thus, in the first-order Born approximation the self-energy is calculated including only a specific type of diagram. The approximation is valid in the limit given by equation (6.1). In mathematical notation, the self-energy in the first-order Born approximation is

$$\Sigma^{1BA}(\mathbf{k}, i\omega_n) = n \int \frac{d^2\mathbf{k}'}{(2\pi)^2} U(\mathbf{k}-\mathbf{k}') G^{(0)}(\mathbf{k}', i\omega_n) U(\mathbf{k}'-\mathbf{k}) \,, \tag{6.10}$$

where n denotes the density of impurities. The impurity Hamiltonians are the same as given in Chapter 5. Replacing the integral with a sum over momenta we obtain

$$\Sigma^{1BA}_{p/m}(i\omega_n) = \frac{nV^2}{N} \sum_{\mathbf{k}'} h^{p/m}_{\text{imp}} G^{(0)}(\mathbf{k}', i\omega_n) h^{p/m}_{\text{imp}} \,. \tag{6.11}$$

It is now clear that we have two interdependent equations: the full Green function $G(\mathbf{k}, i\omega_n)$ given by equation (6.3) depends on the superconducting order parameter $\Delta_{\mathbf{k}}$, in turn, $\Delta_{\mathbf{k}}$ depends on the anomalous Green function $F(\mathbf{k}, i\omega_n)$ which is part of the full Green function. The numerical procedure employed to solve both equations self-consistently, referred to as the AG algorithm, is as follows

1. Assume an initial $\Delta^i_{\mathbf{k}}$.
2. Compute $G^{(0)}(\mathbf{k}, i\omega_n) = U(\mathbf{k})^{-1} \frac{1}{i\omega_n \mathbb{1}_{6\times 6} - H^B_{\text{BdG}}(\mathbf{k})} U(\mathbf{k})$.
3. Compute the self-energy from equation (6.11).
4. Compute the full Green function from equation (6.3).
5. Select the element corresponding to $F(\mathbf{k}, i\omega_n)$ and use this to determine a new value for the order parameter $\Delta^f_{\mathbf{k}}$ through equation (6.7).
6. Set $\Delta^i_{\mathbf{k}} = \Delta^f_{\mathbf{k}}$.
7. Repeat the procedure until a predefined convergence criteria is satisfied.

In the above, $H^B_{\text{BdG}}(\mathbf{k})$ denotes the Hamiltonian in band space and $i(f)$ in $\Delta^{i(f)}_{\mathbf{k}}$ stands for initial (final). The algorithm solves for the order parameter given a temperature T and an impurity density times impurity strength squared nV^2. We benchmark the result of our algorithm for $nV^2 = 0$ against a self-consistent solution of the gap equation using a Bogoliubov-de Gennes (BdG) transformation (the details of which are found in Appendix F), which should yield the same result given that the parameters are the same. The only difference between the BdG curve and the result of the AG algorithm is that, in order to obtain the order parameter in the AG algorithm, a numerical Matsubara sum is carried out. If there are not enough values in the Matsubara sum, i.e. if n in $\omega_n = (2n+1)\pi T$ (with $k_B = 1$) is not large enough, the AG result will deviate from the BdG curve at small temperatures since, as noted before, the distance between each Matsubara frequency scales with T. To be able to compare results between the square and the kagome lattice, we have visually aligned the critical temperatures of the BdG results by altering the superconducting coupling strengths V_{SC} of each order parameter. The BdG results for the square and kagome lattices are seen in Figures 6.1(a) and (b), respectively. In these plots, we have plotted the value $|\Delta|$, where

$$\Delta \equiv \frac{V_{\text{SC}}}{N} \frac{1}{\beta} \sum_{\mathbf{k}' s_3 s_4 \omega_n} f^{s_3 s_4}_{\mathbf{k}'} F_{s_3 s_4}(\mathbf{k}', i\omega_n) \,, \tag{6.12}$$

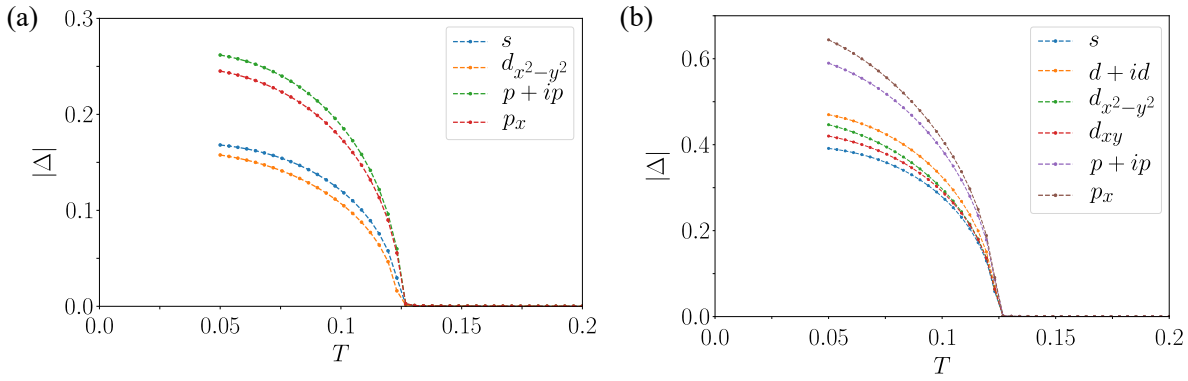

Figure 6.1: (a) The solution of the BdG gap equation for different irreps on the square lattice to show the matching of the critical temperatures of each irrep. (b) Same as (a), but for different irreps on the kagome lattice.

A high number of iterations of the algorithm is needed to capture the sharp transition between $\Delta = 0$ and $\Delta \neq 0$. More details on the convergence of the BdG (and AG) algorithm is found in Appendix F. The AG algorithm has been solved for a $d_{x^2-y^2} + id_{xy}$ order parameter on the kagome lattice, and the result is seen in Figure 6.2(a) where the color denotes the value of nV^2. To determine the critical temperature the data has been fitted, and the fit curves are shown in full lines. Initially, the data was fitted with a function $y = A\sqrt{|T - T_c|}$. This function is a good approximation close to the critical temperature, but an even better fitting function, which is the one used in Figure 6.2(a), is obtained by numerically finding solutions of the mean field equation $y = \tanh(y/T)$ for a set of temperatures T. The data from the AG algorithm is then interpolated to obtain values of Δ at the same set of temperatures. Finally, the difference between the mean-field equation and the AG data is minimized to yield the initial order parameter $\Delta_0 = \Delta(T = 0)$ and the critical temperature T_c. For transparency: The code for the fitting procedure was originally made by A. Kreisel in Matlab. Subsequently, S.C. Holbæk adjusted it to Python and used it to fit the AG data.

In Figure 6.2(b) the critical temperatures of an s-wave (blue), a $d_{x^2-y^2}$ (red) and a p_x (light green) order parameter are depicted, both for the square lattice (symbolized by a square) and kagome lattice (symbolized by a triangle). Furthermore, T_c for a $d+id$ (purple) and a $p+ip$ (light green) order parameter on the kagome lattice is plotted. We obtained curves on the kagome lattice for a set of nV^2 values, but in the comparison to the square lattice we had to take into account that (setting $V = 1$ for simplicity) $n = 1$ in the kagome algorithm corresponds to one impurity on every A site, which means that 1/3 of the total sites of the lattice are occupied by impurities. Whereas on the square lattice $n = 1$ corresponds to all sites occupied by impurities. Thus, in order to compare the two results we should scale the nV^2 values of the kagome lattice by 1/3 when plotting them together with the square lattice results.

Since the order parameters that correspond to one component of a two-dimensional irrep, such as $d_{x^2-y^2}$ and p_x, break rotational symmetry, they do not yield the same result on each sublattice, and therefore we have run the algorithm with impurities located on each of the sublattice sites, and taken an average of the resulting critical temperatures.

Importantly, we notice that the suppression of T_c for a $d_{x^2-y^2}$ order parameter on the square lattice follows the universal AG curve, while on the kagome lattice it is less sensitive. The $d + id$ order parameter on the kagome lattice follows the same trend as the $d_{x^2-y^2}$ one. While they are not as robust to potential impurities as an s-wave order parameter, they are also not as sensitive as usually expected. The curves for the s-wave order parameter on the square and kagome lattices

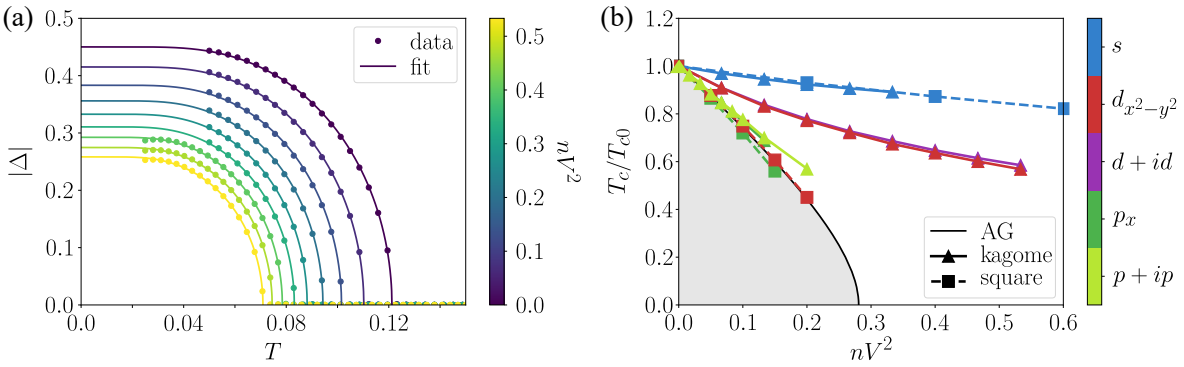

Figure 6.2: (a) The temperature dependence of the $d_{x^2-y^2} + id_{xy}$ order parameter on the kagome lattice in the presence of potential impurities. The color denotes the value of nV^2. (b) The suppression of T_c of an order parameter with s-wave (blue), $d_{x^2-y^2}$ (red), $d + id$ (purple), p_x (dark green) and $p + ip$ (light green) symmetry from scattering on potential impurities with density n and strength V. The squares symbolize results on the square lattice and triangles results on the kagome lattice.

follow each other and only decrease slightly with increasing nV^2. The $p + ip$ order parameter on the kagome lattice is sensitive to impurities and lies closer to the AG curve.

Chapter 7

Conclusion and outlook

> "So at the age of thirty-three and with an h-index of 1 (latest papers not yet published), I entered the Western job market for postdocs."
>
> *Nobel lecture by Andre K. Geim, one of the discoverers of graphene*

The aim of this thesis was to examine superconductivity on a kagome lattice with a focus on modelling impurity effects. Impurity effects have been studied thoroughly in the literature, especially on the square, triangular and honeycomb lattices which are relevant to many materials. The latter, for example, to twisted bilayer graphene. It was not clear from the outset whether any of the properties special to the kagome lattice, sublattice interference for instance, would have any influence on the impurity results, but it was more likely that we would obtain qualitatively similar results to the well-known results on the square lattice.

Luckily, it turned out that there was still new knowledge to be gained from studying superconductivity on the kagome lattice. First, different from the square lattice, we found that on-site interactions on the kagome lattice can lead to a gap with d-wave symmetry. Secondly, additional to intraband states we found that interband pairing states are possible from nearest neighbor interactions.

The main finding of this thesis is the robustness of a sign-changing d-wave superconducting condensate to highly localized impurities on the kagome lattice. Due to the non-trivial momentum dependence of the electronic wave functions on the kagome lattice, the order parameters only have weight on certain subsets of the Fermi surface. This results in the sign-changing d-wave order parameter summing to a non-zero value, rendering it more robust to scattering off of potential impurities. The robustness of the d-wave order parameter was shown by the absence of low-energy bound states in the local density of states and by a smaller than expected suppression of the critical temperature. This result is valid in the idealized case of an impurity localized on only one sublattice site. Impurities in real materials presumably extend to more lattice sites, which would ruin the mechanism described here. Nevertheless, it could have some relevance on the interpretation of STM results on the kagome lattice.

There are many questions which would be interesting for further studies. Relevant to the AV_3Sb_5 compounds, this work omitted the interplay between superconductivity and the charge density wave phase. At ambient pressure, the charge density wave probably has a relevance to the superconducting phase, and including it in our model would be an interesting further study. Furthermore,

generalizing the concepts of this thesis to other systems would also be an interesting study. A cousin of the kagome lattice is called the Lieb lattice. This lattice also has three atoms in the unit cell and features a flat energy band and van Hove singularities, and two of the three sublattices have a D_2 symmetry. An example of atoms arranged in a Lieb lattice is the CuO_2 planes of cuprate superconductors. It would be interesting to see if similar results apply to the Lieb lattice.

After this work was concluded, we became aware of some fairly new literature of relevance to our study. Specifically, one paper experimentally shows the robustness of the anisotropic pairing in the polar phase of superfluid ^3He to oriented columnar defects [42]. Although the system is quite different from the one examined in this thesis, the underlying mechanism of the robustness, namely scattering which only mixes subsystems of the Fermi surface, is similar. This indicates that the mechanism described in this thesis has a relevance for experiments. Other studies examining robustness of unconventional order parameters are [43], [44] and [45]. In these, a "generalized Anderson's theorem" is introduced, and they discuss scattering which does or does not mix extra internal degrees of freedom, such as orbitals or, as in our case, sublattice index. Our study has a different perspective, and the intraband d-wave order parameter examined in this thesis also has non-zero interband contributions.

In conclusion, this thesis work has brought a new outlook on impurity effects in kagome superconductors with possible importance for other systems as well, and it opened up many new questions for further studies.

Appendix A

2×2 matrix representations of the E_1 and E_2 irreps of the D_6 point group

The two-dimensional matrix representations corresponding to the E_1 irrep are

$$D^{E_1}(E) = \begin{pmatrix} 1 & 0 \\ 0 & 1 \end{pmatrix}, \tag{A.1}$$

$$D^{E_1}(C_6^+) = \begin{pmatrix} \frac{1}{2} & -\frac{\sqrt{3}}{2} \\ \frac{\sqrt{3}}{2} & \frac{1}{2} \end{pmatrix}, \quad D^{E_1}(C_6^-) = \begin{pmatrix} \frac{1}{2} & \frac{\sqrt{3}}{2} \\ -\frac{\sqrt{3}}{2} & \frac{1}{2} \end{pmatrix}, \tag{A.2}$$

$$D^{E_1}(C_3^+) = \begin{pmatrix} -\frac{1}{2} & -\frac{\sqrt{3}}{2} \\ \frac{\sqrt{3}}{2} & -\frac{1}{2} \end{pmatrix}, \quad D^{E_1}(C_3^-) = \begin{pmatrix} -\frac{1}{2} & \frac{\sqrt{3}}{2} \\ -\frac{\sqrt{3}}{2} & -\frac{1}{2} \end{pmatrix}, \tag{A.3}$$

$$D^{E_1}(C_2) = \begin{pmatrix} -1 & 0 \\ 0 & -1 \end{pmatrix}, \tag{A.4}$$

$$D^{E_1}(\sigma_v^1) = \begin{pmatrix} \frac{1}{2} & -\frac{\sqrt{3}}{2} \\ -\frac{\sqrt{3}}{2} & -\frac{1}{2} \end{pmatrix}, \quad D^{E_1}(\sigma_v^2) = \begin{pmatrix} \frac{1}{2} & \frac{\sqrt{3}}{2} \\ \frac{\sqrt{3}}{2} & -\frac{1}{2} \end{pmatrix}, \quad D^{E_1}(\sigma_v^3) = \begin{pmatrix} -1 & 0 \\ 0 & 1 \end{pmatrix}, \tag{A.5}$$

$$D^{E_1}(\sigma_d^1) = \begin{pmatrix} -\frac{1}{2} & -\frac{\sqrt{3}}{2} \\ -\frac{\sqrt{3}}{2} & \frac{1}{2} \end{pmatrix}, \quad D^{E_1}(\sigma_d^2) = \begin{pmatrix} 1 & 0 \\ 0 & -1 \end{pmatrix}, \quad D^{E_1}(\sigma_d^3) = \begin{pmatrix} -\frac{1}{2} & \frac{\sqrt{3}}{2} \\ \frac{\sqrt{3}}{2} & \frac{1}{2} \end{pmatrix}. \tag{A.6}$$

The trace of a matrix $D^{E_1}(g)$ yields the character of the element g in the E_1 irrep. The two-dimensional matrix representations corresponding to the E_2 irrep are

$$D^{E_2}(E) = \begin{pmatrix} 1 & 0 \\ 0 & 1 \end{pmatrix}, \tag{A.7}$$

$$D^{E_2}(C_6^+) = \begin{pmatrix} -\frac{1}{2} & -\frac{\sqrt{3}}{2} \\ \frac{\sqrt{3}}{2} & -\frac{1}{2} \end{pmatrix}, \quad D^{E_2}(C_6^-) = \begin{pmatrix} -\frac{1}{2} & \frac{\sqrt{3}}{2} \\ -\frac{\sqrt{3}}{2} & -\frac{1}{2} \end{pmatrix}, \tag{A.8}$$

$$D^{E_2}(C_3^+) = \begin{pmatrix} -\frac{1}{2} & \frac{\sqrt{3}}{2} \\ -\frac{\sqrt{3}}{2} & -\frac{1}{2} \end{pmatrix}, \quad D^{E_2}(C_3^-) = \begin{pmatrix} -\frac{1}{2} & -\frac{\sqrt{3}}{2} \\ \frac{\sqrt{3}}{2} & -\frac{1}{2} \end{pmatrix}, \tag{A.9}$$

$$D^{E_2}(C_2) = \begin{pmatrix} 1 & 0 \\ 0 & 1 \end{pmatrix}, \tag{A.10}$$

$$D^{E_2}(\sigma_v^1) = \begin{pmatrix} -\frac{1}{2} & -\frac{\sqrt{3}}{2} \\ -\frac{\sqrt{3}}{2} & \frac{1}{2} \end{pmatrix}, \quad D^{E_2}(\sigma_v^2) = \begin{pmatrix} -\frac{1}{2} & \frac{\sqrt{3}}{2} \\ \frac{\sqrt{3}}{2} & \frac{1}{2} \end{pmatrix}, \quad D^{E_2}(\sigma_v^3) = \begin{pmatrix} 1 & 0 \\ 0 & -1 \end{pmatrix}, \tag{A.11}$$

$$D^{E_2}(\sigma_d^1) = \begin{pmatrix} -\frac{1}{2} & \frac{\sqrt{3}}{2} \\ \frac{\sqrt{3}}{2} & \frac{1}{2} \end{pmatrix}, \quad D^{E_2}(\sigma_d^2) = \begin{pmatrix} 1 & 0 \\ 0 & -1 \end{pmatrix}, \quad D^{E_2}(\sigma_d^3) = \begin{pmatrix} -\frac{1}{2} & -\frac{\sqrt{3}}{2} \\ -\frac{\sqrt{3}}{2} & \frac{1}{2} \end{pmatrix}. \tag{A.12}$$

We know that E_1 transforms as $\{x, y\}$ and E_2 as $\{x^2 - y^2, 2xy\}$ [32].

Appendix B

Matrix representations of the elements in the D_6 point group

B.1 3×3 matrices for on-site pairing

3×3 matrices representing the elements of the D_6 point group (the identity matrix is omitted). The matrices are written in a basis where $\hat{\mathbf{e}}_1 = \begin{pmatrix} 1 & 0 & 0 \end{pmatrix}^T$ represents site A, $\hat{\mathbf{e}}_2 = \begin{pmatrix} 0 & 1 & 0 \end{pmatrix}^T$ represents site B and $\hat{\mathbf{e}}_3 = \begin{pmatrix} 0 & 0 & 1 \end{pmatrix}^T$ represents site C, see Figure 3.1.

$$D(C_6^+) = \begin{pmatrix} 0 & 1 & 0 \\ 0 & 0 & 1 \\ 1 & 0 & 0 \end{pmatrix}, \quad D(C_6^-) = D(C_6^+)^T, \tag{B.1}$$

$$D(C_3^+) = \begin{pmatrix} 0 & 0 & 1 \\ 1 & 0 & 0 \\ 0 & 1 & 0 \end{pmatrix}, \quad D(C_3^-) = D(C_3^+)^T, \tag{B.2}$$

$$D(C_2) = \begin{pmatrix} 1 & 0 & 0 \\ 0 & 1 & 0 \\ 0 & 0 & 1 \end{pmatrix}, \tag{B.3}$$

$$D(\sigma_v^1) = \begin{pmatrix} 1 & 0 & 0 \\ 0 & 0 & 1 \\ 0 & 1 & 0 \end{pmatrix}, \quad D(\sigma_v^2) = \begin{pmatrix} 0 & 1 & 0 \\ 1 & 0 & 0 \\ 0 & 0 & 1 \end{pmatrix}, \quad D(\sigma_v^3) = \begin{pmatrix} 0 & 0 & 1 \\ 0 & 1 & 0 \\ 1 & 0 & 0 \end{pmatrix}, \tag{B.4}$$

$$D(\sigma_d^1) = \begin{pmatrix} 0 & 1 & 0 \\ 1 & 0 & 0 \\ 0 & 0 & 1 \end{pmatrix}, \quad D(\sigma_d^2) = \begin{pmatrix} 0 & 0 & 1 \\ 0 & 1 & 0 \\ 1 & 0 & 0 \end{pmatrix}, \quad D(\sigma_d^3) = \begin{pmatrix} 1 & 0 & 0 \\ 0 & 0 & 1 \\ 0 & 1 & 0 \end{pmatrix}. \tag{B.5}$$

B.2 6×6 matrices for nearest neighbor pairing

6×6 matrices representing the elements of the D_6 point group (the identity is omitted). The matrices are written in a basis where $\hat{\mathbf{e}}_1 = \begin{pmatrix} 1 & 0 & 0 & 0 & 0 & 0 \end{pmatrix}^T$ represents spin-singlet link a in Figure

4.7(d) of Chapter 4, $\hat{\mathbf{e}}_2 = \begin{pmatrix} 0 & 1 & 0 & 0 & 0 & 0 \end{pmatrix}^T$ represents spin-singlet link b etc.

$$D(C_6^+) = \begin{pmatrix} 0&1&0&0&0&0 \\ 0&0&1&0&0&0 \\ 0&0&0&1&0&0 \\ 0&0&0&0&1&0 \\ 0&0&0&0&0&1 \\ 1&0&0&0&0&0 \end{pmatrix}, \quad D(C_6^-) = D(C_6^+)^T, \tag{B.6}$$

$$D(C_3^+) = \begin{pmatrix} 0&0&1&0&0&0 \\ 0&0&0&1&0&0 \\ 0&0&0&0&1&0 \\ 0&0&0&0&0&1 \\ 1&0&0&0&0&0 \\ 0&1&0&0&0&0 \end{pmatrix}, \quad D(C_3^-) = D(C_3^+)^T, \tag{B.7}$$

$$D(C_2) = \begin{pmatrix} 0&0&0&1&0&0 \\ 0&0&0&0&1&0 \\ 0&0&0&0&0&1 \\ 1&0&0&0&0&0 \\ 0&1&0&0&0&0 \\ 0&0&1&0&0&0 \end{pmatrix}, \tag{B.8}$$

$$D(\sigma_v^1) = \begin{pmatrix} 0&0&0&0&1&0 \\ 0&0&0&1&0&0 \\ 0&0&1&0&0&0 \\ 0&1&0&0&0&0 \\ 1&0&0&0&0&0 \\ 0&0&0&0&0&1 \end{pmatrix}, \quad D(\sigma_v^2) = \begin{pmatrix} 0&0&1&0&0&0 \\ 0&1&0&0&0&0 \\ 1&0&0&0&0&0 \\ 0&0&0&0&0&1 \\ 0&0&0&0&1&0 \\ 0&0&0&1&0&0 \end{pmatrix}, \quad D(\sigma_v^3) = \begin{pmatrix} 1&0&0&0&0&0 \\ 0&0&0&0&0&1 \\ 0&0&0&0&1&0 \\ 0&0&0&1&0&0 \\ 0&0&1&0&0&0 \\ 0&1&0&0&0&0 \end{pmatrix}, \tag{B.9}$$

$$D(\sigma_d^1) = \begin{pmatrix} 0&0&0&0&0&1 \\ 0&0&0&0&1&0 \\ 0&0&0&1&0&0 \\ 0&0&1&0&0&0 \\ 0&1&0&0&0&0 \\ 1&0&0&0&0&0 \end{pmatrix}, \quad D(\sigma_d^2) = \begin{pmatrix} 0&0&0&1&0&0 \\ 0&0&1&0&0&0 \\ 0&1&0&0&0&0 \\ 1&0&0&0&0&0 \\ 0&0&0&0&0&1 \\ 0&0&0&0&1&0 \end{pmatrix}, \quad D(\sigma_d^3) = \begin{pmatrix} 0&1&0&0&0&0 \\ 1&0&0&0&0&0 \\ 0&0&0&0&0&1 \\ 0&0&0&0&1&0 \\ 0&0&0&1&0&0 \\ 0&0&1&0&0&0 \end{pmatrix}. \tag{B.10}$$

The matrices used to generate the projectors for spin-triplet pairing are obtained by multiplying all of the reflection matrices by -1.

Appendix C

Pairing expressions

Irrep	Spin state	Real space interaction	Momentum space pairing matrix
A_1	singlet	$\frac{2}{\sqrt{3}}\sum_{\mathbf{R}}[c_{B,\mathbf{R}-\mathbf{a}_1,\uparrow}c_{B,\mathbf{R}-\mathbf{a}_1,\downarrow}$ $+c_{A,\mathbf{R}-\mathbf{a}_2,\uparrow}c_{A,\mathbf{R}-\mathbf{a}_2,\downarrow}$ $+c_{C,\mathbf{R}-\mathbf{a}_3,\uparrow}c_{C,\mathbf{R}-\mathbf{a}_3,\downarrow}]$	$(f^{A_1}_{\mathrm{OS}})^\dagger_s \propto \frac{1}{\sqrt{3}}\begin{pmatrix}1&0&0\\0&1&0\\0&0&1\end{pmatrix}$
$(E_2)_{11}$	singlet	$\frac{2}{\sqrt{6}}\sum_{\mathbf{R}}[-2c_{B,\mathbf{R}-\mathbf{a}_1,\uparrow}c_{B,\mathbf{R}-\mathbf{a}_1,\downarrow}$ $+c_{A,\mathbf{R}-\mathbf{a}_2,\uparrow}c_{A,\mathbf{R}-\mathbf{a}_2,\downarrow}$ $+c_{C,\mathbf{R}-\mathbf{a}_3,\uparrow}c_{C,\mathbf{R}-\mathbf{a}_3,\downarrow}]$	$(f^{E_2}_{11,\mathrm{OS}})^\dagger_s \propto \frac{1}{\sqrt{6}}\begin{pmatrix}1&0&0\\0&-2&0\\0&0&1\end{pmatrix}$
$(E_2)_{21}$	singlet	$\frac{2}{\sqrt{2}}\sum_{\mathbf{R}}[c_{A,\mathbf{R}-\mathbf{a}_2,\uparrow}c_{A,\mathbf{R}-\mathbf{a}_2,\downarrow}$ $-c_{C,\mathbf{R}-\mathbf{a}_3,\uparrow}c_{C,\mathbf{R}-\mathbf{a}_3,\downarrow}]$	$(f^{E_2}_{21,\mathrm{OS}})^\dagger_s \propto \frac{1}{\sqrt{2}}\begin{pmatrix}1&0&0\\0&0&0\\0&0&-1\end{pmatrix}$

Table C.1: Summary of the different on-site pairing states on the kagome lattice. The pairing matrix is written in Nambu formalism $\left(c_{A,-\mathbf{k},\downarrow}\ c_{B,-\mathbf{k},\downarrow}\ c_{C,-\mathbf{k},\downarrow}\right)(\Delta^\Gamma)^\dagger_{s/t}\left(c_{A,\mathbf{k},\uparrow}\ c_{B,\mathbf{k},\uparrow}\ c_{C,\mathbf{k},\uparrow}\right)^T$, where subscript s/t refers to singlet/triplet pairs. The matrices are written in a gauge which is non-periodic in momentum space.

Irrep	Spin state	Real space interaction	Momentum space pairing matrix
A_1	singlet	$\frac{1}{\sqrt{6}}\sum_{\mathbf{R}}[(c_{C,\mathbf{R}-\mathbf{a}_3,\uparrow}c_{B,\mathbf{R}+\mathbf{a}_1,\downarrow}+c_{B,\mathbf{R}+\mathbf{a}_1,\uparrow}c_{C,\mathbf{R}-\mathbf{a}_3,\downarrow})$ $+(c_{C,\mathbf{R}+\mathbf{a}_3,\uparrow}c_{B,\mathbf{R}-\mathbf{a}_1,\downarrow}+c_{B,\mathbf{R}-\mathbf{a}_1,\uparrow}c_{C,\mathbf{R}+\mathbf{a}_3,\downarrow})$ $+(c_{A,\mathbf{R}-\mathbf{a}_2,\uparrow}c_{C,\mathbf{R}-\mathbf{a}_3,\downarrow}+c_{C,\mathbf{R}-\mathbf{a}_3,\uparrow}c_{A,\mathbf{R}-\mathbf{a}_2,\downarrow})$ $+(c_{A,\mathbf{R}+\mathbf{a}_2,\uparrow}c_{C,\mathbf{R}+\mathbf{a}_3,\downarrow}+c_{C,\mathbf{R}+\mathbf{a}_3,\uparrow}c_{A,\mathbf{R}+\mathbf{a}_2,\downarrow})$ $+(c_{B,\mathbf{R}-\mathbf{a}_1,\uparrow}c_{A,\mathbf{R}-\mathbf{a}_2,\downarrow}+c_{A,\mathbf{R}-\mathbf{a}_2,\uparrow}c_{B,\mathbf{R}-\mathbf{a}_1,\downarrow})$ $+(c_{B,\mathbf{R}+\mathbf{a}_1,\uparrow}c_{A,\mathbf{R}+\mathbf{a}_2,\downarrow}+c_{A,\mathbf{R}+\mathbf{a}_2,\uparrow}c_{B,\mathbf{R}+\mathbf{a}_1,\downarrow})]$	$(f^{A_1}_{\mathrm{NN}})^\dagger_s \propto \frac{1}{\sqrt{6}}\begin{pmatrix}0 & \cos(k_3) & \cos(k_1)\\ \cos(k_3) & 0 & \cos(k_2)\\ \cos(k_1) & \cos(k_2) & 0\end{pmatrix}$
B_2	singlet	$\frac{1}{\sqrt{6}}\sum_{\mathbf{R}}[(c_{C,\mathbf{R}-\mathbf{a}_3,\uparrow}c_{B,\mathbf{R}+\mathbf{a}_1,\downarrow}+c_{B,\mathbf{R}+\mathbf{a}_1,\uparrow}c_{C,\mathbf{R}-\mathbf{a}_3,\downarrow})$ $-(c_{C,\mathbf{R}+\mathbf{a}_3,\uparrow}c_{B,\mathbf{R}-\mathbf{a}_1,\downarrow}+c_{B,\mathbf{R}-\mathbf{a}_1,\uparrow}c_{C,\mathbf{R}+\mathbf{a}_3,\downarrow})$ $-(c_{A,\mathbf{R}-\mathbf{a}_2,\uparrow}c_{C,\mathbf{R}-\mathbf{a}_3,\downarrow}+c_{C,\mathbf{R}-\mathbf{a}_3,\uparrow}c_{A,\mathbf{R}-\mathbf{a}_2,\downarrow})$ $+(c_{A,\mathbf{R}+\mathbf{a}_2,\uparrow}c_{C,\mathbf{R}+\mathbf{a}_3,\downarrow}+c_{C,\mathbf{R}+\mathbf{a}_3,\uparrow}c_{A,\mathbf{R}+\mathbf{a}_2,\downarrow})$ $+(c_{B,\mathbf{R}-\mathbf{a}_1,\uparrow}c_{A,\mathbf{R}-\mathbf{a}_2,\downarrow}+c_{A,\mathbf{R}-\mathbf{a}_2,\uparrow}c_{B,\mathbf{R}-\mathbf{a}_1,\downarrow})$ $-(c_{B,\mathbf{R}+\mathbf{a}_1,\uparrow}c_{A,\mathbf{R}+\mathbf{a}_2,\downarrow}+c_{A,\mathbf{R}+\mathbf{a}_2,\uparrow}c_{B,\mathbf{R}+\mathbf{a}_1,\downarrow})]$	$(f^{B_2}_{\mathrm{NN}})^\dagger_s \propto \frac{i}{\sqrt{6}}\begin{pmatrix}0 & -\sin(k_3) & \sin(k_1)\\ \sin(k_3) & 0 & \sin(k_2)\\ -\sin(k_1) & -\sin(k_2) & 0\end{pmatrix}$
$(E_1)_{11}$	singlet	$\frac{1}{2}\sum_{\mathbf{R}}[(c_{C,\mathbf{R}-\mathbf{a}_3,\uparrow}c_{B,\mathbf{R}+\mathbf{a}_1,\downarrow}+c_{B,\mathbf{R}+\mathbf{a}_1,\uparrow}c_{C,\mathbf{R}-\mathbf{a}_3,\downarrow})$ $-(c_{C,\mathbf{R}+\mathbf{a}_3,\uparrow}c_{B,\mathbf{R}-\mathbf{a}_1,\downarrow}+c_{B,\mathbf{R}-\mathbf{a}_1,\uparrow}c_{C,\mathbf{R}+\mathbf{a}_3,\downarrow})$ $-(c_{B,\mathbf{R}-\mathbf{a}_1,\uparrow}c_{A,\mathbf{R}-\mathbf{a}_2,\downarrow}+c_{A,\mathbf{R}-\mathbf{a}_2,\uparrow}c_{B,\mathbf{R}-\mathbf{a}_1,\downarrow})$ $+(c_{B,\mathbf{R}+\mathbf{a}_1,\uparrow}c_{A,\mathbf{R}+\mathbf{a}_2,\downarrow}+c_{A,\mathbf{R}+\mathbf{a}_2,\uparrow}c_{B,\mathbf{R}+\mathbf{a}_1,\downarrow})]$	$(f^{E_1}_{11,\mathrm{NN}})^\dagger_s \propto \frac{i}{2}\begin{pmatrix}0 & \sin(k_3) & 0\\ -\sin(k_3) & 0 & \sin(k_2)\\ 0 & -\sin(k_2) & 0\end{pmatrix}$
$(E_1)_{21}$	singlet	$\frac{1}{\sqrt{12}}\sum_{\mathbf{R}}[-(c_{C,\mathbf{R}-\mathbf{a}_3,\uparrow}c_{\mathbf{R}+\mathbf{a}_1,B,\downarrow}+c_{B,\mathbf{R}+\mathbf{a}_1,\uparrow}c_{\mathbf{R}-\mathbf{a}_3,C,\downarrow})$ $+(c_{C,\mathbf{R}+\mathbf{a}_3,\uparrow}c_{B,\mathbf{R}-\mathbf{a}_1,\downarrow}+c_{B,\mathbf{R}-\mathbf{a}_1,\uparrow}c_{C,\mathbf{R}+\mathbf{a}_3,\downarrow})$ $-2(c_{A,\mathbf{R}-\mathbf{a}_2,\uparrow}c_{C,\mathbf{R}-\mathbf{a}_3,\downarrow}+c_{C,\mathbf{R}-\mathbf{a}_3,\uparrow}c_{A,\mathbf{R}-\mathbf{a}_2,\downarrow})$ $+2(c_{A,\mathbf{R}+\mathbf{a}_2,\uparrow}c_{C,\mathbf{R}+\mathbf{a}_3,\downarrow}+c_{C,\mathbf{R}+\mathbf{a}_3,\uparrow}c_{A,\mathbf{R}+\mathbf{a}_2,\downarrow})$ $-(c_{B,\mathbf{R}-\mathbf{a}_1,\uparrow}c_{A,\mathbf{R}-\mathbf{a}_2,\downarrow}+c_{A,\mathbf{R}-\mathbf{a}_2,\uparrow}c_{B,\mathbf{R}-\mathbf{a}_1,\downarrow})$ $+(c_{B,\mathbf{R}+\mathbf{a}_1,\uparrow}c_{A,\mathbf{R}+\mathbf{a}_2,\downarrow}+c_{A,\mathbf{R}+\mathbf{a}_2,\uparrow}c_{B,\mathbf{R}+\mathbf{a}_1,\downarrow})]$	$(f^{E_1}_{21,\mathrm{NN}})^\dagger_s \propto \frac{i}{\sqrt{12}}\begin{pmatrix}0 & \sin(k_3) & 2\sin(k_1)\\ -\sin(k_3) & 0 & -\sin(k_2)\\ -2\sin(k_1) & \sin(k_2) & 0\end{pmatrix}$
$(E_2)_{11}$	singlet	$\frac{1}{\sqrt{12}}\sum_{\mathbf{R}}[-(c_{C,\mathbf{R}-\mathbf{a}_3,\uparrow}c_{B,\mathbf{R}+\mathbf{a}_1,\downarrow}+c_{B,\mathbf{R}+\mathbf{a}_1,\uparrow}c_{C,\mathbf{R}-\mathbf{a}_3,\downarrow})$ $-(c_{C,\mathbf{R}+\mathbf{a}_3,\uparrow}c_{B,\mathbf{R}-\mathbf{a}_1,\downarrow}+c_{B,\mathbf{R}-\mathbf{a}_1,\uparrow}c_{C,\mathbf{R}+\mathbf{a}_3,\downarrow})$ $+2(c_{A,\mathbf{R}-\mathbf{a}_2,\uparrow}c_{C,\mathbf{R}-\mathbf{a}_3,\downarrow}+c_{C,\mathbf{R}-\mathbf{a}_3,\uparrow}c_{A,\mathbf{R}-\mathbf{a}_2,\downarrow})$ $+2(c_{A,\mathbf{R}+\mathbf{a}_2,\uparrow}c_{C,\mathbf{R}+\mathbf{a}_3,\downarrow}+c_{C,\mathbf{R}+\mathbf{a}_3,\uparrow}c_{A,\mathbf{R}+\mathbf{a}_2,\downarrow})$ $-(c_{B,\mathbf{R}-\mathbf{a}_1,\uparrow}c_{A,\mathbf{R}-\mathbf{a}_2,\downarrow}+c_{A,\mathbf{R}-\mathbf{a}_2,\uparrow}c_{B,\mathbf{R}-\mathbf{a}_1,\downarrow})$ $-(c_{B,\mathbf{R}+\mathbf{a}_1,\uparrow}c_{A,\mathbf{R}+\mathbf{a}_2,\downarrow}+c_{A,\mathbf{R}+\mathbf{a}_2,\uparrow}c_{B,\mathbf{R}+\mathbf{a}_1,\downarrow})]$	$(f^{E_2}_{11,\mathrm{NN}})^\dagger_s \propto \frac{1}{\sqrt{12}}\begin{pmatrix}0 & -\cos(k_3) & 2\cos(k_1)\\ -\cos(k_3) & 0 & -\cos(k_2)\\ 2\cos(k_1) & -\cos(k_2) & 0\end{pmatrix}$
$(E_2)_{21}$	singlet	$\frac{1}{2}\sum_{\mathbf{R}}[-(c_{C,\mathbf{R}-\mathbf{a}_3,\uparrow}c_{B,\mathbf{R}+\mathbf{a}_1,\downarrow}+c_{B,\mathbf{R}+\mathbf{a}_1,\uparrow}c_{C,\mathbf{R}-\mathbf{a}_3,\downarrow})$ $-(c_{C,\mathbf{R}+\mathbf{a}_3,\uparrow}c_{B,\mathbf{R}-\mathbf{a}_1,\downarrow}+c_{B,\mathbf{R}-\mathbf{a}_1,\uparrow}c_{C,\mathbf{R}+\mathbf{a}_3,\downarrow})$ $+(c_{B,\mathbf{R}-\mathbf{a}_1,\uparrow}c_{A,\mathbf{R}-\mathbf{a}_2,\downarrow}+c_{A,\mathbf{R}-\mathbf{a}_2,\uparrow}c_{B,\mathbf{R}-\mathbf{a}_1,\downarrow})$ $+(c_{B,\mathbf{R}+\mathbf{a}_1,\uparrow}c_{A,\mathbf{R}+\mathbf{a}_2,\downarrow}+c_{A,\mathbf{R}+\mathbf{a}_2,\uparrow}c_{B,\mathbf{R}+\mathbf{a}_1,\downarrow})]$	$(f^{E_2}_{21,\mathrm{NN}})^\dagger_s \propto \frac{1}{2}\begin{pmatrix}0 & \cos(k_3) & 0\\ \cos(k_3) & 0 & -\cos(k_2)\\ 0 & -\cos(k_2) & 0\end{pmatrix}$
A_2	triplet	$\frac{1}{\sqrt{6}}\sum_{\mathbf{R}}[(c_{C,\mathbf{R}-\mathbf{a}_3,\uparrow}c_{B,\mathbf{R}+\mathbf{a}_1,\downarrow}-c_{B,\mathbf{R}+\mathbf{a}_1,\uparrow}c_{C,\mathbf{R}-\mathbf{a}_3,\downarrow})$ $+(c_{C,\mathbf{R}+\mathbf{a}_3,\uparrow}c_{B,\mathbf{R}-\mathbf{a}_1,\downarrow}-c_{B,\mathbf{R}-\mathbf{a}_1,\uparrow}c_{C,\mathbf{R}+\mathbf{a}_3,\downarrow})$ $+(c_{A,\mathbf{R}-\mathbf{a}_2,\uparrow}c_{C,\mathbf{R}-\mathbf{a}_3,\downarrow}-c_{C,\mathbf{R}-\mathbf{a}_3,\uparrow}c_{A,\mathbf{R}-\mathbf{a}_2,\downarrow})$ $+(c_{A,\mathbf{R}+\mathbf{a}_2,\uparrow}c_{C,\mathbf{R}+\mathbf{a}_3,\downarrow}-c_{C,\mathbf{R}+\mathbf{a}_3,\uparrow}c_{A,\mathbf{R}+\mathbf{a}_2,\downarrow})$ $+(c_{B,\mathbf{R}-\mathbf{a}_1,\uparrow}c_{A,\mathbf{R}-\mathbf{a}_2,\downarrow}-c_{A,\mathbf{R}-\mathbf{a}_2,\uparrow}c_{B,\mathbf{R}-\mathbf{a}_1,\downarrow})$ $+(c_{B,\mathbf{R}+\mathbf{a}_1,\uparrow}c_{A,\mathbf{R}+\mathbf{a}_2,\downarrow}-c_{A,\mathbf{R}+\mathbf{a}_2,\uparrow}c_{B,\mathbf{R}+\mathbf{a}_1,\downarrow})]$	$(f^{A_2}_{\mathrm{NN}})^\dagger_t \propto \frac{1}{\sqrt{6}}\begin{pmatrix}0 & -\cos(k_3) & \cos(k_1)\\ \cos(k_3) & 0 & -\cos(k_2)\\ -\cos(k_1) & \cos(k_2) & 0\end{pmatrix}$
B_1	triplet	$\frac{1}{\sqrt{6}}\sum_{\mathbf{R}}[(c_{C,\mathbf{R}-\mathbf{a}_3,\uparrow}c_{B,\mathbf{R}+\mathbf{a}_1,\downarrow}-c_{B,\mathbf{R}+\mathbf{a}_1,\uparrow}c_{C,\mathbf{R}-\mathbf{a}_3,\downarrow})$ $-(c_{C,\mathbf{R}+\mathbf{a}_3,\uparrow}c_{B,\mathbf{R}-\mathbf{a}_1,\downarrow}-c_{B,\mathbf{R}-\mathbf{a}_1,\uparrow}c_{C,\mathbf{R}+\mathbf{a}_3,\downarrow})$ $-(c_{A,\mathbf{R}-\mathbf{a}_2,\uparrow}c_{C,\mathbf{R}-\mathbf{a}_3,\downarrow}-c_{C,\mathbf{R}-\mathbf{a}_3,\uparrow}c_{A,\mathbf{R}-\mathbf{a}_2,\downarrow})$ $+(c_{A,\mathbf{R}+\mathbf{a}_2,\uparrow}c_{C,\mathbf{R}+\mathbf{a}_3,\downarrow}-c_{C,\mathbf{R}+\mathbf{a}_3,\uparrow}c_{A,\mathbf{R}+\mathbf{a}_2,\downarrow})$ $+(c_{B,\mathbf{R}-\mathbf{a}_1,\uparrow}c_{A,\mathbf{R}-\mathbf{a}_2,\downarrow}-c_{A,\mathbf{R}-\mathbf{a}_2,\uparrow}c_{B,\mathbf{R}-\mathbf{a}_1,\downarrow})$ $-(c_{B,\mathbf{R}+\mathbf{a}_1,\uparrow}c_{A,\mathbf{R}+\mathbf{a}_2,\downarrow}-c_{A,\mathbf{R}+\mathbf{a}_2,\uparrow}c_{B,\mathbf{R}+\mathbf{a}_1,\downarrow})]$	$(f^{B_1}_{\mathrm{NN}})^\dagger_t \propto \frac{i}{\sqrt{6}}\begin{pmatrix}0 & -\sin(k_3) & -\sin(k_1)\\ -\sin(k_3) & 0 & \sin(k_2)\\ -\sin(k_1) & \sin(k_2) & 0\end{pmatrix}$
$(E_1)_{11}$	triplet	$\frac{1}{\sqrt{12}}\sum_{\mathbf{R}}[-(c_{C,\mathbf{R}-\mathbf{a}_3,\uparrow}c_{B,\mathbf{R}+\mathbf{a}_1,\downarrow}-c_{B,\mathbf{R}+\mathbf{a}_1,\uparrow}c_{C,\mathbf{R}-\mathbf{a}_3,\downarrow})$ $+(c_{C,\mathbf{R}+\mathbf{a}_3,\uparrow}c_{B,\mathbf{R}-\mathbf{a}_1,\downarrow}-c_{B,\mathbf{R}-\mathbf{a}_1,\uparrow}c_{C,\mathbf{R}+\mathbf{a}_3,\downarrow})$ $-2(c_{A,\mathbf{R}-\mathbf{a}_2,\uparrow}c_{C,\mathbf{R}-\mathbf{a}_3,\downarrow}-c_{C,\mathbf{R}-\mathbf{a}_3,\uparrow}c_{A,\mathbf{R}-\mathbf{a}_2,\downarrow})$ $+2(c_{A,\mathbf{R}+\mathbf{a}_2,\uparrow}c_{C,\mathbf{R}+\mathbf{a}_3,\downarrow}-c_{C,\mathbf{R}+\mathbf{a}_3,\uparrow}c_{\mathbf{R}+\mathbf{a}_2,A,\downarrow})$ $-(c_{B,\mathbf{R}-\mathbf{a}_1,\uparrow}c_{A,\mathbf{R}-\mathbf{a}_2,\downarrow}-c_{A,\mathbf{R}-\mathbf{a}_2,\uparrow}c_{B,\mathbf{R}-\mathbf{a}_1,\downarrow})$ $+(c_{B,\mathbf{R}+\mathbf{a}_1,\uparrow}c_{A,\mathbf{R}+\mathbf{a}_2,\downarrow}-c_{A,\mathbf{R}+\mathbf{a}_2,\uparrow}c_{B,\mathbf{R}+\mathbf{a}_1,\downarrow})]$	$(f^{E_1}_{11,\mathrm{NN}})^\dagger_t \propto \frac{i}{\sqrt{12}}\begin{pmatrix}0 & \sin(k_3) & -2\sin(k_1)\\ \sin(k_3) & 0 & -\sin(k_2)\\ -2\sin(k_1) & -\sin(k_2) & 0\end{pmatrix}$
$(E_1)_{21}$	triplet	$\frac{1}{2}\sum_{\mathbf{R}}[(c_{C,\mathbf{R}-\mathbf{a}_3,\uparrow}c_{B,\mathbf{R}+\mathbf{a}_1,\downarrow}-c_{B,\mathbf{R}+\mathbf{a}_1,\uparrow}c_{C,\mathbf{R}-\mathbf{a}_3,\downarrow})$ $-(c_{C,\mathbf{R}+\mathbf{a}_3,\uparrow}c_{B,\mathbf{R}-\mathbf{a}_1,\downarrow}-c_{B,\mathbf{R}-\mathbf{a}_1,\uparrow}c_{C,\mathbf{R}+\mathbf{a}_3,\downarrow})$ $-(c_{B,\mathbf{R}-\mathbf{a}_1,\uparrow}c_{A,\mathbf{R}-\mathbf{a}_2,\downarrow}-c_{A,\mathbf{R}-\mathbf{a}_2,\uparrow}c_{B,\mathbf{R}-\mathbf{a}_1,\downarrow})$ $+(c_{B,\mathbf{R}+\mathbf{a}_1,\uparrow}c_{A,\mathbf{R}+\mathbf{a}_2,\downarrow}-c_{A,\mathbf{R}+\mathbf{a}_2,\uparrow}c_{B,\mathbf{R}+\mathbf{a}_1,\downarrow})]$	$(f^{E_1}_{21,\mathrm{NN}})^\dagger_t \propto \frac{i}{2}\begin{pmatrix}0 & \sin(k_3) & 0\\ \sin(k_3) & 0 & \sin(k_2)\\ 0 & \sin(k_2) & 0\end{pmatrix}$
$(E_2)_{11}$	triplet	$\frac{1}{2}\sum_{\mathbf{R}}[-(c_{C,\mathbf{R}-\mathbf{a}_3,\uparrow}c_{B,\mathbf{R}+\mathbf{a}_1,\downarrow}-c_{B,\mathbf{R}+\mathbf{a}_1,\uparrow}c_{C,\mathbf{R}-\mathbf{a}_3,\downarrow})$ $-(c_{C,\mathbf{R}+\mathbf{a}_3,\uparrow}c_{B,\mathbf{R}-\mathbf{a}_1,\downarrow}-c_{B,\mathbf{R}-\mathbf{a}_1,\uparrow}c_{C,\mathbf{R}+\mathbf{a}_3,\downarrow})$ $+(c_{B,\mathbf{R}-\mathbf{a}_1,\uparrow}c_{A,\mathbf{R}-\mathbf{a}_2,\downarrow}-c_{A,\mathbf{R}-\mathbf{a}_2,\uparrow}c_{B,\mathbf{R}-\mathbf{a}_1,\downarrow})$ $+(c_{B,\mathbf{R}+\mathbf{a}_1,\uparrow}c_{A,\mathbf{R}+\mathbf{a}_2,\downarrow}-c_{A,\mathbf{R}+\mathbf{a}_2,\uparrow}c_{B,\mathbf{R}+\mathbf{a}_1,\downarrow})]$	$(f^{E_2}_{11,\mathrm{NN}})^\dagger_t \propto \frac{1}{2}\begin{pmatrix}0 & -\cos(k_3) & 0\\ \cos(k_3) & 0 & \cos(k_2)\\ 0 & -\cos(k_2) & 0\end{pmatrix}$
$(E_2)_{21}$	triplet	$\frac{1}{\sqrt{12}}\sum_{\mathbf{R}}[-(c_{C,\mathbf{R}-\mathbf{a}_3,\uparrow}c_{B,\mathbf{R}+\mathbf{a}_1,\downarrow}-c_{B,\mathbf{R}+\mathbf{a}_1,\uparrow}c_{C,\mathbf{R}-\mathbf{a}_3,\downarrow})$ $-(c_{C,\mathbf{R}+\mathbf{a}_3,\uparrow}c_{B,\mathbf{R}-\mathbf{a}_1,\downarrow}-c_{B,\mathbf{R}-\mathbf{a}_1,\uparrow}c_{C,\mathbf{R}+\mathbf{a}_3,\downarrow})$ $+2(c_{A,\mathbf{R}-\mathbf{a}_2,\uparrow}c_{C,\mathbf{R}-\mathbf{a}_3,\downarrow}-c_{C,\mathbf{R}-\mathbf{a}_3,\uparrow}c_{A,\mathbf{R}-\mathbf{a}_2,\downarrow})$ $+2(c_{A,\mathbf{R}+\mathbf{a}_2,\uparrow}c_{C,\mathbf{R}+\mathbf{a}_3,\downarrow}-c_{C,\mathbf{R}+\mathbf{a}_3,\uparrow}c_{A,\mathbf{R}+\mathbf{a}_2,\downarrow})$ $-(c_{B,\mathbf{R}-\mathbf{a}_1,\uparrow}c_{A,\mathbf{R}-\mathbf{a}_2,\downarrow}-c_{A,\mathbf{R}-\mathbf{a}_2,\uparrow}c_{B,\mathbf{R}-\mathbf{a}_1,\downarrow})$ $-(c_{B,\mathbf{R}+\mathbf{a}_1,\uparrow}c_{A,\mathbf{R}+\mathbf{a}_2,\downarrow}-c_{A,\mathbf{R}+\mathbf{a}_2,\uparrow}c_{B,\mathbf{R}+\mathbf{a}_1,\downarrow})]$	$(f^{E_2}_{21,\mathrm{NN}})^\dagger_t \propto \frac{1}{\sqrt{12}}\begin{pmatrix}0 & \cos(k_3) & 2\cos(k_1)\\ -\cos(k_3) & 0 & \cos(k_2)\\ -2\cos(k_1) & -\cos(k_2) & 0\end{pmatrix}$

Table C.2: Summary of the different nearest neighbor pairing states on the kagome lattice. The pairing matrix is written in Nambu formalism $\left(c_{A,-\mathbf{k},\downarrow}\ c_{B,-\mathbf{k},\downarrow}\ c_{C,-\mathbf{k},\downarrow}\right)\left(\Delta^\Gamma\right)^\dagger_{s/t}\left(c_{A,\mathbf{k},\uparrow}\ c_{B,\mathbf{k},\uparrow}\ c_{C,\mathbf{k},\uparrow}\right)^T$, where subscript s/t refers to singlet/triplet pairs. The matrices are written in a gauge which is non-periodic in momentum space.

Irrep	Spin state	Real space interaction	Momentum space pairing matrix
A_1	singlet	$\frac{1}{\sqrt{6}}\sum_{\mathbf{R}}[(c_{C,\mathbf{R}+\mathbf{a}_3,\uparrow}c_{B,\mathbf{R}+\mathbf{a}_1,\downarrow}+c_{B,\mathbf{R}+\mathbf{a}_1,\uparrow}c_{C,\mathbf{R}+\mathbf{a}_3,\downarrow})$ $+(c_{B,\mathbf{R}-\mathbf{a}_1,\uparrow}c_{C,\mathbf{R}-\mathbf{a}_3,\downarrow}+c_{C,\mathbf{R}-\mathbf{a}_3,\uparrow}c_{B,\mathbf{R}-\mathbf{a}_1,\downarrow})$ $+(c_{B,\mathbf{R}-\mathbf{a}_1,\uparrow}c_{A,\mathbf{R}+\mathbf{a}_2,\downarrow}+c_{A,\mathbf{R}+\mathbf{a}_2,\uparrow}c_{B,\mathbf{R}-\mathbf{a}_1,\downarrow})$ $+(c_{A,\mathbf{R}-\mathbf{a}_2,\uparrow}c_{B,\mathbf{R}+\mathbf{a}_1,\downarrow}+c_{B,\mathbf{R}+\mathbf{a}_1,\uparrow}c_{A,\mathbf{R}-\mathbf{a}_2,\downarrow})$ $+(c_{C,\mathbf{R}-\mathbf{a}_3,\uparrow}c_{A,\mathbf{R}+\mathbf{a}_2,\downarrow}+c_{A,\mathbf{R}+\mathbf{a}_2,\uparrow}c_{C,\mathbf{R}-\mathbf{a}_3,\downarrow})$ $+(c_{C,\mathbf{R}+\mathbf{a}_3,\uparrow}c_{A,\mathbf{R}-\mathbf{a}_2,\downarrow}+c_{A,\mathbf{R}-\mathbf{a}_2,\uparrow}c_{C,\mathbf{R}+\mathbf{a}_3,\downarrow})]$	$(f^{A_1}_{\mathrm{NNN}})^\dagger_s \propto \frac{1}{\sqrt{6}}\begin{pmatrix}0 & \cos(\mathbf{k}\cdot(\mathbf{a}_1+\mathbf{a}_2)) & \cos(\mathbf{k}\cdot(\mathbf{a}_2+\mathbf{a}_3))\\ \cos(\mathbf{k}\cdot(\mathbf{a}_1+\mathbf{a}_2)) & 0 & \cos(\mathbf{k}\cdot(\mathbf{a}_3-\mathbf{a}_1))\\ \cos(\mathbf{k}\cdot(\mathbf{a}_2+\mathbf{a}_3)) & \cos(\mathbf{k}\cdot(\mathbf{a}_3-\mathbf{a}_1)) & 0\end{pmatrix}$
B_1	singlet	$\frac{1}{\sqrt{6}}\sum_{\mathbf{R}}[(c_{C,\mathbf{R}+\mathbf{a}_3,\uparrow}c_{B,\mathbf{R}+\mathbf{a}_1,\downarrow}+c_{B,\mathbf{R}+\mathbf{a}_1,\uparrow}c_{C,\mathbf{R}+\mathbf{a}_3,\downarrow})$ $-(c_{B,\mathbf{R}-\mathbf{a}_1,\uparrow}c_{C,\mathbf{R}-\mathbf{a}_3,\downarrow}+c_{C,\mathbf{R}-\mathbf{a}_3,\uparrow}c_{B,\mathbf{R}-\mathbf{a}_1,\downarrow})$ $-(c_{B,\mathbf{R}-\mathbf{a}_1,\uparrow}c_{A,\mathbf{R}+\mathbf{a}_2,\downarrow}+c_{A,\mathbf{R}+\mathbf{a}_2,\uparrow}c_{B,\mathbf{R}-\mathbf{a}_1,\downarrow})$ $+(c_{A,\mathbf{R}-\mathbf{a}_2,\uparrow}c_{B,\mathbf{R}+\mathbf{a}_1,\downarrow}+c_{B,\mathbf{R}+\mathbf{a}_1,\uparrow}c_{A,\mathbf{R}-\mathbf{a}_2,\downarrow})$ $-(c_{C,\mathbf{R}-\mathbf{a}_3,\uparrow}c_{A,\mathbf{R}+\mathbf{a}_2,\downarrow}+c_{A,\mathbf{R}+\mathbf{a}_2,\uparrow}c_{C,\mathbf{R}-\mathbf{a}_3,\downarrow})$ $+(c_{C,\mathbf{R}+\mathbf{a}_3,\uparrow}c_{A,\mathbf{R}-\mathbf{a}_2,\downarrow}+c_{A,\mathbf{R}-\mathbf{a}_2,\uparrow}c_{C,\mathbf{R}+\mathbf{a}_3,\downarrow})]$	$(f^{B_1}_{\mathrm{NNN}})^\dagger_s \propto \frac{i}{\sqrt{6}}\begin{pmatrix}0 & \sin(\mathbf{k}\cdot(\mathbf{a}_1+\mathbf{a}_2)) & \sin(\mathbf{k}\cdot(\mathbf{a}_2+\mathbf{a}_3))\\ -\sin(\mathbf{k}\cdot(\mathbf{a}_1+\mathbf{a}_2)) & 0 & \sin(\mathbf{k}\cdot(\mathbf{a}_3-\mathbf{a}_1))\\ -\sin(\mathbf{k}\cdot(\mathbf{a}_2+\mathbf{a}_3)) & -\sin(\mathbf{k}\cdot(\mathbf{a}_3-\mathbf{a}_1)) & 0\end{pmatrix}$
$(E_1)_{11}$	singlet	$\frac{1}{\sqrt{12}}\sum_{\mathbf{R}}[-(c_{C,\mathbf{R}+\mathbf{a}_3,\uparrow}c_{B,\mathbf{R}+\mathbf{a}_1,\downarrow}+c_{B,\mathbf{R}+\mathbf{a}_1,\uparrow}c_{C,\mathbf{R}+\mathbf{a}_3,\downarrow})$ $+(c_{B,\mathbf{R}-\mathbf{a}_1,\uparrow}c_{C,\mathbf{R}-\mathbf{a}_3,\downarrow}+c_{C,\mathbf{R}-\mathbf{a}_3,\uparrow}c_{B,\mathbf{R}-\mathbf{a}_1,\downarrow})$ $+(c_{B,\mathbf{R}-\mathbf{a}_1,\uparrow}c_{A,\mathbf{R}+\mathbf{a}_2,\downarrow}+c_{A,\mathbf{R}+\mathbf{a}_2,\uparrow}c_{B,\mathbf{R}-\mathbf{a}_1,\downarrow})$ $-(c_{A,\mathbf{R}-\mathbf{a}_2,\uparrow}c_{B,\mathbf{R}+\mathbf{a}_1,\downarrow}+c_{B,\mathbf{R}+\mathbf{a}_1,\uparrow}c_{A,\mathbf{R}-\mathbf{a}_2,\downarrow})$ $-2(c_{C,\mathbf{R}-\mathbf{a}_3,\uparrow}c_{A,\mathbf{R}+\mathbf{a}_2,\downarrow}+c_{A,\mathbf{R}+\mathbf{a}_2,\uparrow}c_{C,\mathbf{R}-\mathbf{a}_3,\downarrow})$ $+2(c_{C,\mathbf{R}+\mathbf{a}_3,\uparrow}c_{A,\mathbf{R}-\mathbf{a}_2,\downarrow}+c_{A,\mathbf{R}-\mathbf{a}_2,\uparrow}c_{C,\mathbf{R}+\mathbf{a}_3,\downarrow})]$	$(f^{E_1}_{11,\mathrm{NNN}})^\dagger_s \propto \frac{i}{\sqrt{12}}\begin{pmatrix}0 & -\sin(\mathbf{k}\cdot(\mathbf{a}_1+\mathbf{a}_2)) & 2\sin(\mathbf{k}\cdot(\mathbf{a}_2+\mathbf{a}_3))\\ \sin(\mathbf{k}\cdot(\mathbf{a}_1+\mathbf{a}_2)) & 0 & -\sin(\mathbf{k}\cdot(\mathbf{a}_3-\mathbf{a}_1))\\ -2\sin(\mathbf{k}\cdot(\mathbf{a}_2+\mathbf{a}_3)) & \sin(\mathbf{k}\cdot(\mathbf{a}_3-\mathbf{a}_1)) & 0\end{pmatrix}$
$(E_1)_{21}$	singlet	$\frac{1}{2}\sum_{\mathbf{R}}[(c_{C,\mathbf{R}+\mathbf{a}_3,\uparrow}c_{B,\mathbf{R}+\mathbf{a}_1,\downarrow}+c_{B,\mathbf{R}+\mathbf{a}_1,\uparrow}c_{C,\mathbf{R}+\mathbf{a}_3,\downarrow})$ $-(c_{B,\mathbf{R}-\mathbf{a}_1,\uparrow}c_{C,\mathbf{R}-\mathbf{a}_3,\downarrow}+c_{C,\mathbf{R}-\mathbf{a}_3,\uparrow}c_{B,\mathbf{R}-\mathbf{a}_1,\downarrow})$ $+(c_{B,\mathbf{R}-\mathbf{a}_1,\uparrow}c_{A,\mathbf{R}+\mathbf{a}_2,\downarrow}+c_{A,\mathbf{R}+\mathbf{a}_2,\uparrow}c_{B,\mathbf{R}-\mathbf{a}_1,\downarrow})$ $-(c_{A,\mathbf{R}-\mathbf{a}_2,\uparrow}c_{B,\mathbf{R}+\mathbf{a}_1,\downarrow}+c_{B,\mathbf{R}+\mathbf{a}_1,\uparrow}c_{A,\mathbf{R}-\mathbf{a}_2,\downarrow})]$	$(f^{E_1}_{21,\mathrm{NNN}})^\dagger_s \propto \frac{i}{2}\begin{pmatrix}0 & -\sin(\mathbf{k}\cdot(\mathbf{a}_1+\mathbf{a}_2)) & 0\\ \sin(\mathbf{k}\cdot(\mathbf{a}_1+\mathbf{a}_2)) & 0 & \sin(\mathbf{k}\cdot(\mathbf{a}_3-\mathbf{a}_1))\\ 0 & -\sin(\mathbf{k}\cdot(\mathbf{a}_3-\mathbf{a}_1)) & 0\end{pmatrix}$
$(E_2)_{11}$	singlet	$\frac{1}{\sqrt{12}}\sum_{\mathbf{R}}[-(c_{C,\mathbf{R}+\mathbf{a}_3,\uparrow}c_{B,\mathbf{R}+\mathbf{a}_1,\downarrow}+c_{B,\mathbf{R}+\mathbf{a}_1,\uparrow}c_{C,\mathbf{R}+\mathbf{a}_3,\downarrow})$ $-(c_{B,\mathbf{R}-\mathbf{a}_1,\uparrow}c_{C,\mathbf{R}-\mathbf{a}_3,\downarrow}+c_{C,\mathbf{R}-\mathbf{a}_3,\uparrow}c_{B,\mathbf{R}-\mathbf{a}_1,\downarrow})$ $-(c_{B,\mathbf{R}-\mathbf{a}_1,\uparrow}c_{A,\mathbf{R}+\mathbf{a}_2,\downarrow}+c_{A,\mathbf{R}+\mathbf{a}_2,\uparrow}c_{B,\mathbf{R}-\mathbf{a}_1,\downarrow})$ $-(c_{A,\mathbf{R}-\mathbf{a}_2,\uparrow}c_{B,\mathbf{R}+\mathbf{a}_1,\downarrow}+c_{B,\mathbf{R}+\mathbf{a}_1,\uparrow}c_{A,\mathbf{R}-\mathbf{a}_2,\downarrow})$ $+2(c_{C,\mathbf{R}-\mathbf{a}_3,\uparrow}c_{A,\mathbf{R}+\mathbf{a}_2,\downarrow}+c_{A,\mathbf{R}+\mathbf{a}_2,\uparrow}c_{C,\mathbf{R}-\mathbf{a}_3,\downarrow})$ $+2(c_{C,\mathbf{R}+\mathbf{a}_3,\uparrow}c_{A,\mathbf{R}-\mathbf{a}_2,\downarrow}+c_{A,\mathbf{R}-\mathbf{a}_2,\uparrow}c_{C,\mathbf{R}+\mathbf{a}_3,\downarrow})]$	$(f^{E_2}_{11,\mathrm{NNN}})^\dagger_s \propto \frac{1}{\sqrt{12}}\begin{pmatrix}0 & -\cos(\mathbf{k}\cdot(\mathbf{a}_1+\mathbf{a}_2)) & 2\cos(\mathbf{k}\cdot(\mathbf{a}_2+\mathbf{a}_3))\\ -\cos(\mathbf{k}\cdot(\mathbf{a}_1+\mathbf{a}_2)) & 0 & -\cos(\mathbf{k}\cdot(\mathbf{a}_3-\mathbf{a}_1))\\ 2\cos(\mathbf{k}\cdot(\mathbf{a}_2+\mathbf{a}_3)) & -\cos(\mathbf{k}\cdot(\mathbf{a}_3-\mathbf{a}_1)) & 0\end{pmatrix}$
$(E_2)_{21}$	singlet	$\frac{1}{2}\sum_{\mathbf{R}}[-(c_{C,\mathbf{R}+\mathbf{a}_3,\uparrow}c_{B,\mathbf{R}+\mathbf{a}_1,\downarrow}+c_{B,\mathbf{R}+\mathbf{a}_1,\uparrow}c_{C,\mathbf{R}+\mathbf{a}_3,\downarrow})$ $-(c_{B,\mathbf{R}-\mathbf{a}_1,\uparrow}c_{C,\mathbf{R}-\mathbf{a}_3,\downarrow}+c_{C,\mathbf{R}-\mathbf{a}_3,\uparrow}c_{B,\mathbf{R}-\mathbf{a}_1,\downarrow})$ $+(c_{B,\mathbf{R}-\mathbf{a}_1,\uparrow}c_{A,\mathbf{R}+\mathbf{a}_2,\downarrow}+c_{A,\mathbf{R}+\mathbf{a}_2,\uparrow}c_{B,\mathbf{R}-\mathbf{a}_1,\downarrow})$ $+(c_{A,\mathbf{R}-\mathbf{a}_2,\uparrow}c_{B,\mathbf{R}+\mathbf{a}_1,\downarrow}+c_{B,\mathbf{R}+\mathbf{a}_1,\uparrow}c_{A,\mathbf{R}-\mathbf{a}_2,\downarrow})]$	$(f^{E_2}_{21,\mathrm{NNN}})^\dagger_s \propto \frac{1}{2}\begin{pmatrix}0 & -\cos(\mathbf{k}\cdot(\mathbf{a}_1+\mathbf{a}_2)) & 0\\ -\cos(\mathbf{k}\cdot(\mathbf{a}_1+\mathbf{a}_2)) & 0 & \cos(\mathbf{k}\cdot(\mathbf{a}_3-\mathbf{a}_1))\\ 0 & \cos(\mathbf{k}\cdot(\mathbf{a}_3-\mathbf{a}_1)) & 0\end{pmatrix}$
A_2	triplet	$\frac{1}{\sqrt{6}}\sum_{\mathbf{R}}[(c_{B,\mathbf{R}+\mathbf{a}_1,\uparrow}c_{C,\mathbf{R}+\mathbf{a}_3,\downarrow}-c_{C,\mathbf{R}+\mathbf{a}_3,\uparrow}c_{B,\mathbf{R}+\mathbf{a}_1,\downarrow})$ $+(c_{B,\mathbf{R}-\mathbf{a}_1,\uparrow}c_{C,\mathbf{R}-\mathbf{a}_3,\downarrow}-c_{C,\mathbf{R}-\mathbf{a}_3,\uparrow}c_{B,\mathbf{R}-\mathbf{a}_1,\downarrow})$ $+(c_{A,\mathbf{R}+\mathbf{a}_2,\uparrow}c_{B,\mathbf{R}-\mathbf{a}_1,\downarrow}-c_{B,\mathbf{R}-\mathbf{a}_1,\uparrow}c_{A,\mathbf{R}+\mathbf{a}_2,\downarrow})$ $+(c_{A,\mathbf{R}-\mathbf{a}_2,\uparrow}c_{B,\mathbf{R}+\mathbf{a}_1,\downarrow}-c_{B,\mathbf{R}+\mathbf{a}_1,\uparrow}c_{A,\mathbf{R}-\mathbf{a}_2,\downarrow})$ $+(c_{C,\mathbf{R}-\mathbf{a}_3,\uparrow}c_{A,\mathbf{R}+\mathbf{a}_2,\downarrow}-c_{A,\mathbf{R}+\mathbf{a}_2,\uparrow}c_{C,\mathbf{R}-\mathbf{a}_3,\downarrow})$ $+(c_{C,\mathbf{R}+\mathbf{a}_3,\uparrow}c_{A,\mathbf{R}-\mathbf{a}_2,\downarrow}-c_{A,\mathbf{R}-\mathbf{a}_2,\uparrow}c_{C,\mathbf{R}+\mathbf{a}_3,\downarrow})]$	$(f^{A_2}_{\mathrm{NNN}})^\dagger_t \propto \frac{1}{\sqrt{6}}\begin{pmatrix}0 & -\cos(\mathbf{k}\cdot(\mathbf{a}_1+\mathbf{a}_2)) & \cos(\mathbf{k}\cdot(\mathbf{a}_2+\mathbf{a}_3))\\ \cos(\mathbf{k}\cdot(\mathbf{a}_1+\mathbf{a}_2)) & 0 & -\cos(\mathbf{k}\cdot(\mathbf{a}_3-\mathbf{a}_1))\\ -\cos(\mathbf{k}\cdot(\mathbf{a}_2+\mathbf{a}_3)) & \cos(\mathbf{k}\cdot(\mathbf{a}_3-\mathbf{a}_1)) & 0\end{pmatrix}$
B_2	triplet	$\frac{1}{\sqrt{6}}\sum_{\mathbf{R}}[(c_{B,\mathbf{R}+\mathbf{a}_1,\uparrow}c_{C,\mathbf{R}+\mathbf{a}_3,\downarrow}-c_{C,\mathbf{R}+\mathbf{a}_3,\uparrow}c_{B,\mathbf{R}+\mathbf{a}_1,\downarrow})$ $-(c_{B,\mathbf{R}-\mathbf{a}_1,\uparrow}c_{C,\mathbf{R}-\mathbf{a}_3,\downarrow}-c_{C,\mathbf{R}-\mathbf{a}_3,\uparrow}c_{B,\mathbf{R}-\mathbf{a}_1,\downarrow})$ $-(c_{A,\mathbf{R}+\mathbf{a}_2,\uparrow}c_{B,\mathbf{R}-\mathbf{a}_1,\downarrow}-c_{B,\mathbf{R}-\mathbf{a}_1,\uparrow}c_{A,\mathbf{R}+\mathbf{a}_2,\downarrow})$ $+(c_{A,\mathbf{R}-\mathbf{a}_2,\uparrow}c_{B,\mathbf{R}+\mathbf{a}_1,\downarrow}-c_{B,\mathbf{R}+\mathbf{a}_1,\uparrow}c_{A,\mathbf{R}-\mathbf{a}_2,\downarrow})$ $-(c_{C,\mathbf{R}-\mathbf{a}_3,\uparrow}c_{A,\mathbf{R}+\mathbf{a}_2,\downarrow}-c_{A,\mathbf{R}+\mathbf{a}_2,\uparrow}c_{C,\mathbf{R}-\mathbf{a}_3,\downarrow})$ $+(c_{C,\mathbf{R}+\mathbf{a}_3,\uparrow}c_{A,\mathbf{R}-\mathbf{a}_2,\downarrow}-c_{A,\mathbf{R}-\mathbf{a}_2,\uparrow}c_{C,\mathbf{R}+\mathbf{a}_3,\downarrow})]$	$(f^{B_2}_{\mathrm{NNN}})^\dagger_t \propto \frac{i}{\sqrt{6}}\begin{pmatrix}0 & -\sin(\mathbf{k}\cdot(\mathbf{a}_1+\mathbf{a}_2)) & \sin(\mathbf{k}\cdot(\mathbf{a}_2+\mathbf{a}_3))\\ -\sin(\mathbf{k}\cdot(\mathbf{a}_1+\mathbf{a}_2)) & 0 & -\sin(\mathbf{k}\cdot(\mathbf{a}_3-\mathbf{a}_1))\\ \sin(\mathbf{k}\cdot(\mathbf{a}_2+\mathbf{a}_3)) & -\sin(\mathbf{k}\cdot(\mathbf{a}_3-\mathbf{a}_1)) & 0\end{pmatrix}$
$(E_1)_{11}$	triplet	$\frac{1}{2}\sum_{\mathbf{R}}[(c_{B,\mathbf{R}+\mathbf{a}_1,\uparrow}c_{C,\mathbf{R}+\mathbf{a}_3,\downarrow}-c_{C,\mathbf{R}+\mathbf{a}_3,\uparrow}c_{B,\mathbf{R}+\mathbf{a}_1,\downarrow})$ $-(c_{B,\mathbf{R}-\mathbf{a}_1,\uparrow}c_{C,\mathbf{R}-\mathbf{a}_3,\downarrow}-c_{C,\mathbf{R}-\mathbf{a}_3,\uparrow}c_{B,\mathbf{R}-\mathbf{a}_1,\downarrow})$ $+(c_{A,\mathbf{R}+\mathbf{a}_2,\uparrow}c_{B,\mathbf{R}-\mathbf{a}_1,\downarrow}-c_{B,\mathbf{R}-\mathbf{a}_1,\uparrow}c_{A,\mathbf{R}+\mathbf{a}_2,\downarrow})$ $-(c_{A,\mathbf{R}-\mathbf{a}_2,\uparrow}c_{B,\mathbf{R}+\mathbf{a}_1,\downarrow}-c_{B,\mathbf{R}+\mathbf{a}_1,\uparrow}c_{A,\mathbf{R}-\mathbf{a}_2,\downarrow})]$	$(f^{E_1}_{11,\mathrm{NNN}})^\dagger_t \propto \frac{i}{2}\begin{pmatrix}0 & \sin(\mathbf{k}\cdot(\mathbf{a}_1+\mathbf{a}_2)) & 0\\ \sin(\mathbf{k}\cdot(\mathbf{a}_1+\mathbf{a}_2)) & 0 & -\sin(\mathbf{k}\cdot(\mathbf{a}_3-\mathbf{a}_1))\\ 0 & -\sin(\mathbf{k}\cdot(\mathbf{a}_3-\mathbf{a}_1)) & 0\end{pmatrix}$
$(E_1)_{21}$	triplet	$\frac{1}{\sqrt{12}}\sum_{\mathbf{R}}[-(c_{B,\mathbf{R}+\mathbf{a}_1,\uparrow}c_{C,\mathbf{R}+\mathbf{a}_3,\downarrow}-c_{C,\mathbf{R}+\mathbf{a}_3,\uparrow}c_{B,\mathbf{R}+\mathbf{a}_1,\downarrow})$ $+(c_{B,\mathbf{R}-\mathbf{a}_1,\uparrow}c_{C,\mathbf{R}-\mathbf{a}_3,\downarrow}-c_{C,\mathbf{R}-\mathbf{a}_3,\uparrow}c_{B,\mathbf{R}-\mathbf{a}_1,\downarrow})$ $+(c_{A,\mathbf{R}+\mathbf{a}_2,\uparrow}c_{B,\mathbf{R}-\mathbf{a}_1,\downarrow}-c_{B,\mathbf{R}-\mathbf{a}_1,\uparrow}c_{A,\mathbf{R}+\mathbf{a}_2,\downarrow})$ $-(c_{A,\mathbf{R}-\mathbf{a}_2,\uparrow}c_{B,\mathbf{R}+\mathbf{a}_1,\downarrow}-c_{B,\mathbf{R}+\mathbf{a}_1,\uparrow}c_{A,\mathbf{R}-\mathbf{a}_2,\downarrow})$ $-2(c_{C,\mathbf{R}-\mathbf{a}_3,\uparrow}c_{A,\mathbf{R}+\mathbf{a}_2,\downarrow}-c_{A,\mathbf{R}+\mathbf{a}_2,\uparrow}c_{C,\mathbf{R}-\mathbf{a}_3,\downarrow})$ $+2(c_{C,\mathbf{R}+\mathbf{a}_3,\uparrow}c_{A,\mathbf{R}-\mathbf{a}_2,\downarrow}-c_{A,\mathbf{R}-\mathbf{a}_2,\uparrow}c_{C,\mathbf{R}+\mathbf{a}_3,\downarrow})]$	$(f^{E_1}_{21,\mathrm{NNN}})^\dagger_t \propto \frac{i}{\sqrt{12}}\begin{pmatrix}0 & \sin(\mathbf{k}\cdot(\mathbf{a}_1+\mathbf{a}_2)) & 2\sin(\mathbf{k}\cdot(\mathbf{a}_2+\mathbf{a}_3))\\ \sin(\mathbf{k}\cdot(\mathbf{a}_1+\mathbf{a}_2)) & 0 & \sin(\mathbf{k}\cdot(\mathbf{a}_3-\mathbf{a}_1))\\ 2\sin(\mathbf{k}\cdot(\mathbf{a}_2+\mathbf{a}_3)) & \sin(\mathbf{k}\cdot(\mathbf{a}_3-\mathbf{a}_1)) & 0\end{pmatrix}$
$(E_2)_{11}$	triplet	$\frac{1}{2}\sum_{\mathbf{R}}[-(c_{B,\mathbf{R}+\mathbf{a}_1,\uparrow}c_{C,\mathbf{R}+\mathbf{a}_3,\downarrow}-c_{C,\mathbf{R}+\mathbf{a}_3,\uparrow}c_{B,\mathbf{R}+\mathbf{a}_1,\downarrow})$ $-(c_{B,\mathbf{R}-\mathbf{a}_1,\uparrow}c_{C,\mathbf{R}-\mathbf{a}_3,\downarrow}-c_{C,\mathbf{R}-\mathbf{a}_3,\uparrow}c_{B,\mathbf{R}-\mathbf{a}_1,\downarrow})$ $+(c_{A,\mathbf{R}+\mathbf{a}_2,\uparrow}c_{B,\mathbf{R}-\mathbf{a}_1,\downarrow}-c_{B,\mathbf{R}-\mathbf{a}_1,\uparrow}c_{A,\mathbf{R}+\mathbf{a}_2,\downarrow})$ $+(c_{A,\mathbf{R}-\mathbf{a}_2,\uparrow}c_{B,\mathbf{R}+\mathbf{a}_1,\downarrow}-c_{B,\mathbf{R}+\mathbf{a}_1,\uparrow}c_{A,\mathbf{R}-\mathbf{a}_2,\downarrow})]$	$(f^{E_2}_{11,\mathrm{NNN}})^\dagger_t \propto \frac{1}{2}\begin{pmatrix}0 & -\cos(\mathbf{k}\cdot(\mathbf{a}_1+\mathbf{a}_2)) & 0\\ \cos(\mathbf{k}\cdot(\mathbf{a}_1+\mathbf{a}_2)) & 0 & \cos(\mathbf{k}\cdot(\mathbf{a}_3-\mathbf{a}_1))\\ 0 & -\cos(\mathbf{k}\cdot(\mathbf{a}_3-\mathbf{a}_1)) & 0\end{pmatrix}$
$(E_2)_{21}$	triplet	$\frac{1}{\sqrt{12}}\sum_{\mathbf{R}}[-(c_{B,\mathbf{R}+\mathbf{a}_1,\uparrow}c_{C,\mathbf{R}+\mathbf{a}_3,\downarrow}-c_{C,\mathbf{R}+\mathbf{a}_3,\uparrow}c_{B,\mathbf{R}+\mathbf{a}_1,\downarrow})$ $-(c_{B,\mathbf{R}-\mathbf{a}_1,\uparrow}c_{C,\mathbf{R}-\mathbf{a}_3,\downarrow}-c_{C,\mathbf{R}-\mathbf{a}_3,\uparrow}c_{B,\mathbf{R}-\mathbf{a}_1,\downarrow})$ $-(c_{A,\mathbf{R}+\mathbf{a}_2,\uparrow}c_{B,\mathbf{R}-\mathbf{a}_1,\downarrow}-c_{B,\mathbf{R}-\mathbf{a}_1,\uparrow}c_{A,\mathbf{R}+\mathbf{a}_2,\downarrow})$ $-(c_{A,\mathbf{R}-\mathbf{a}_2,\uparrow}c_{B,\mathbf{R}+\mathbf{a}_1,\downarrow}-c_{B,\mathbf{R}+\mathbf{a}_1,\uparrow}c_{A,\mathbf{R}-\mathbf{a}_2,\downarrow})$ $+2(c_{C,\mathbf{R}-\mathbf{a}_3,\uparrow}c_{A,\mathbf{R}+\mathbf{a}_2,\downarrow}-c_{A,\mathbf{R}+\mathbf{a}_2,\uparrow}c_{C,\mathbf{R}-\mathbf{a}_3,\downarrow})$ $+2(c_{C,\mathbf{R}+\mathbf{a}_3,\uparrow}c_{A,\mathbf{R}-\mathbf{a}_2,\downarrow}-c_{A,\mathbf{R}-\mathbf{a}_2,\uparrow}c_{C,\mathbf{R}+\mathbf{a}_3,\downarrow})]$	$(f^{E_2}_{21,\mathrm{NNN}})^\dagger_t \propto \frac{1}{\sqrt{12}}\begin{pmatrix}0 & \cos(\mathbf{k}\cdot(\mathbf{a}_1+\mathbf{a}_2)) & 2\cos(\mathbf{k}\cdot(\mathbf{a}_2+\mathbf{a}_3))\\ -\cos(\mathbf{k}\cdot(\mathbf{a}_1+\mathbf{a}_2)) & 0 & \cos(\mathbf{k}\cdot(\mathbf{a}_3-\mathbf{a}_1))\\ -2\cos(\mathbf{k}\cdot(\mathbf{a}_2+\mathbf{a}_3)) & -\cos(\mathbf{k}\cdot(\mathbf{a}_3-\mathbf{a}_1)) & 0\end{pmatrix}$

Table C.3: Summary of the different next nearest neighbor pairing states on the kagome lattice. The pairing matrix is written in Nambu formalism $\left(c_{A,-\mathbf{k},\downarrow}\ c_{B,-\mathbf{k},\downarrow}\ c_{C,-\mathbf{k},\downarrow}\right)\left(\Delta^\Gamma\right)^\dagger_{s/t}\left(c_{A,\mathbf{k},\uparrow}\ c_{B,\mathbf{k},\uparrow}\ c_{C,\mathbf{k},\uparrow}\right)^T$, where subscript s/t refers to singlet/triplet pairs. The matrices are written in a gauge which is non-periodic in momentum space.

Irrep	Spin state	Real space interaction	Momentum space pairing matrix
A_1	singlet	$\frac{1}{\sqrt{3}}\sum_{\mathbf{R}}[c_{B,\mathbf{R}+\mathbf{a}_1,\uparrow}c_{B,\mathbf{R}-\mathbf{a}_1,\downarrow}+c_{B,\mathbf{R}-\mathbf{a}_1,\uparrow}c_{B,\mathbf{R}+\mathbf{a}_1,\downarrow}$ $+c_{A,\mathbf{R}+\mathbf{a}_2,\uparrow}c_{A,\mathbf{R}-\mathbf{a}_2,\downarrow}+c_{A,\mathbf{R}-\mathbf{a}_2,\uparrow}c_{A,\mathbf{R}+\mathbf{a}_2,\downarrow}$ $+c_{C,\mathbf{R}+\mathbf{a}_3,\uparrow}c_{C,\mathbf{R}-\mathbf{a}_3,\downarrow}+c_{C,\mathbf{R}-\mathbf{a}_3,\uparrow}c_{C,\mathbf{R}+\mathbf{a}_3,\downarrow}]$	$(f^{A_1}_{3rd})^\dagger_s \propto \frac{1}{\sqrt{3}}\begin{pmatrix}\cos(2k_2) & 0 & 0\\ 0 & \cos(2k_1) & 0\\ 0 & 0 & \cos(2k_3)\end{pmatrix}$
$(E_2)_{11}$	singlet	$\frac{1}{\sqrt{6}}\sum_{\mathbf{R}}[2(c_{B,\mathbf{R}+\mathbf{a}_1,\uparrow}c_{B,\mathbf{R}-\mathbf{a}_1,\downarrow}+c_{B,\mathbf{R}-\mathbf{a}_1,\uparrow}c_{B,\mathbf{R}+\mathbf{a}_1,\downarrow})$ $-(c_{A,\mathbf{R}+\mathbf{a}_2,\uparrow}c_{A,\mathbf{R}-\mathbf{a}_2,\downarrow}+c_{A,\mathbf{R}-\mathbf{a}_2,\uparrow}c_{A,\mathbf{R}+\mathbf{a}_2,\downarrow})$ $-(c_{C,\mathbf{R}+\mathbf{a}_3,\uparrow}c_{C,\mathbf{R}-\mathbf{a}_3,\downarrow}+c_{C,\mathbf{R}-\mathbf{a}_3,\uparrow}c_{C,\mathbf{R}+\mathbf{a}_3,\downarrow})]$	$(f^{E_2}_{11,3rd})^\dagger_s \propto \frac{1}{\sqrt{6}}\begin{pmatrix}-\cos(2k_2) & 0 & 0\\ 0 & 2\cos(2k_1) & 0\\ 0 & 0 & -\cos(2k_3)\end{pmatrix}$
$(E_2)_{21}$	singlet	$\frac{1}{\sqrt{2}}\sum_{\mathbf{R}}[c_{A,\mathbf{R}+\mathbf{a}_2,\uparrow}c_{A,\mathbf{R}-\mathbf{a}_2,\downarrow}+c_{A,\mathbf{R}-\mathbf{a}_2,\uparrow}c_{A,\mathbf{R}+\mathbf{a}_2,\downarrow}$ $-(c_{C,\mathbf{R}+\mathbf{a}_3,\uparrow}c_{C,\mathbf{R}-\mathbf{a}_3,\downarrow}+c_{C,\mathbf{R}-\mathbf{a}_3,\uparrow}c_{C,\mathbf{R}+\mathbf{a}_3,\downarrow})]$	$(f^{E_2}_{21,3rd})^\dagger_s \propto \frac{1}{\sqrt{2}}\begin{pmatrix}\cos(2k_2) & 0 & 0\\ 0 & 0 & 0\\ 0 & 0 & -\cos(2k_3)\end{pmatrix}$
B_1	triplet	$\frac{1}{\sqrt{3}}\sum_{\mathbf{R}}[c_{B,\mathbf{R}+\mathbf{a}_1,\uparrow}c_{B,\mathbf{R}-\mathbf{a}_1,\downarrow}-c_{B,\mathbf{R}-\mathbf{a}_1,\uparrow}c_{B,\mathbf{R}+\mathbf{a}_1,\downarrow}$ $+c_{A,\mathbf{R}-\mathbf{a}_2,\uparrow}c_{A,\mathbf{R}+\mathbf{a}_2,\downarrow}-c_{A,\mathbf{R}+\mathbf{a}_2,\uparrow}c_{A,\mathbf{R}-\mathbf{a}_2,\downarrow}$ $+c_{C,\mathbf{R}+\mathbf{a}_3,\uparrow}c_{C,\mathbf{R}-\mathbf{a}_3,\downarrow}-c_{C,\mathbf{R}-\mathbf{a}_3,\uparrow}c_{C,\mathbf{R}+\mathbf{a}_3,\downarrow}]$	$(f^{B_1}_{3rd})^\dagger_t \propto \frac{1}{\sqrt{3}}\begin{pmatrix}-\sin(2k_2) & 0 & 0\\ 0 & \sin(2k_1) & 0\\ 0 & 0 & \sin(2k_3)\end{pmatrix}$
$(E_1)_{11}$	triplet	$\frac{1}{\sqrt{6}}\sum_{\mathbf{R}}[2(c_{B,\mathbf{R}+\mathbf{a}_1,\uparrow}c_{B,\mathbf{R}-\mathbf{a}_1,\downarrow}-c_{B,\mathbf{R}-\mathbf{a}_1,\uparrow}c_{B,\mathbf{R}+\mathbf{a}_1,\downarrow})$ $+c_{A,\mathbf{R}+\mathbf{a}_2,\uparrow}c_{A,\mathbf{R}-\mathbf{a}_2,\downarrow}-c_{A,\mathbf{R}-\mathbf{a}_2,\uparrow}c_{A,\mathbf{R}+\mathbf{a}_2,\downarrow}$ $+c_{C,\mathbf{R}-\mathbf{a}_3,\uparrow}c_{C,\mathbf{R}+\mathbf{a}_3,\downarrow}-c_{C,\mathbf{R}+\mathbf{a}_3,\uparrow}c_{C,\mathbf{R}-\mathbf{a}_3,\downarrow}]$	$(f^{E_1}_{11,3rd})^\dagger_t \propto \frac{1}{\sqrt{6}}\begin{pmatrix}\sin(2k_2) & 0 & 0\\ 0 & 2\sin(2k_1) & 0\\ 0 & 0 & -\sin(2k_3)\end{pmatrix}$
$(E_1)_{21}$	triplet	$\frac{1}{\sqrt{2}}\sum_{\mathbf{R}}[c_{A,\mathbf{R}+\mathbf{a}_2,\uparrow}c_{A,\mathbf{R}-\mathbf{a}_2,\downarrow}-c_{A,\mathbf{R}-\mathbf{a}_2,\uparrow}c_{A,\mathbf{R}+\mathbf{a}_2,\downarrow}$ $+c_{C,\mathbf{R}+\mathbf{a}_3,\uparrow}c_{C,\mathbf{R}-\mathbf{a}_3,\downarrow}-c_{C,\mathbf{R}-\mathbf{a}_3,\uparrow}c_{C,\mathbf{R}+\mathbf{a}_3,\downarrow}]$	$(f^{E_1}_{21,3rd})^\dagger_t \propto \frac{1}{\sqrt{2}}\begin{pmatrix}\sin(2k_2) & 0 & 0\\ 0 & 0 & 0\\ 0 & 0 & \sin(2k_3)\end{pmatrix}$

Table C.4: Summary of the different 3rd nearest neighbor in-hexagon pairing states on the kagome lattice. The pairing matrix is written in Nambu formalism $\left(c_{A,-\mathbf{k},\downarrow}\ c_{B,-\mathbf{k},\downarrow}\ c_{C,-\mathbf{k},\downarrow}\right)(\Delta^\Gamma)^\dagger_{s/t}\left(c_{A,\mathbf{k},\uparrow}\ c_{B,\mathbf{k},\uparrow}\ c_{C,\mathbf{k},\uparrow}\right)^T$, where subscript s/t refers to singlet/triplet pairs. The matrices are written in a gauge which is non-periodic in momentum space.

Appendix D

Transformation of the superconducting order parameter from sublattice to band space

Our objective is to perform a transformation of the order parameter from sublattice and momentum space to band and momentum space. For this purpose we will employ the unitary transformation that diagonalizes the normal state, tight-binding Hamiltonian H_{TB} and thus transforms from sublattice to band basis

$$c_{n,\mathbf{k},\sigma} = \sum_{s} u_{sn}(\mathbf{k}) c_{s,\mathbf{k},\sigma} \,, \tag{D.1}$$

where $c_{n,\mathbf{k},\sigma}$ and $c_{s,\mathbf{k},\sigma}$ are fermionic annihilation operators in band and sublattice space, respectively. Equivalently, the transformation written in matrix notation is

$$\begin{pmatrix} c_{1,\mathbf{k},\sigma} \\ c_{2,\mathbf{k},\sigma} \\ c_{3,\mathbf{k},\sigma} \end{pmatrix} = U(\mathbf{k}) \begin{pmatrix} c_{A,\mathbf{k},\sigma} \\ c_{B,\mathbf{k},\sigma} \\ c_{C,\mathbf{k},\sigma} \end{pmatrix} \,, \tag{D.2}$$

or

$$\tilde{c}_{\mathbf{k},\sigma} = U(\mathbf{k}) c_{\mathbf{k},\sigma} \,, \tag{D.3}$$

where

$$\tilde{c}_{\mathbf{k},\sigma} \equiv \begin{pmatrix} c_{1,\mathbf{k},\sigma} & c_{2,\mathbf{k},\sigma} & c_{3,\mathbf{k},\sigma} \end{pmatrix}^T \,, \tag{D.4}$$

with $n = 1, 2, 3$ indexing the energy bands, and

$$c_{\mathbf{k},\sigma} = \begin{pmatrix} c_{A,\mathbf{k},\sigma} & c_{B,\mathbf{k},\sigma} & c_{C,\mathbf{k},\sigma} \end{pmatrix}^T \,, \tag{D.5}$$

while

$$\tilde{c}^{\dagger}_{\mathbf{k},\sigma} = c^{\dagger}_{\mathbf{k},\sigma} U^{\dagger}(\mathbf{k}) \tag{D.6}$$

Utilizing the definition of a unitary matrix $U^{\dagger}U = \mathbb{1}$, the transformation of the tight-binding Hamiltonian takes the form

$$c^{\dagger}_{\mathbf{k},\uparrow} H_{\mathrm{TB}}(\mathbf{k}) c_{\mathbf{k},\uparrow} = c^{\dagger}_{\mathbf{k},\uparrow} U^{\dagger}(\mathbf{k}) U(\mathbf{k}) H_{\mathrm{TB}}(\mathbf{k}) U^{\dagger}(\mathbf{k}) U(\mathbf{k}) c_{\mathbf{k},\uparrow} = \tilde{c}^{\dagger}_{\mathbf{k},\uparrow} H^{B}_{\mathrm{TB}}(\mathbf{k}) \tilde{c}_{\mathbf{k},\uparrow} \tag{D.7}$$

where $c^\dagger_{\mathbf{k},\sigma} = (c^\dagger_{A,\mathbf{k},\sigma}, c^\dagger_{B,\mathbf{k},\sigma}, c^\dagger_{C,\mathbf{k},\sigma})$. On the other hand, the transformation of the order parameter, which is on the off-diagonal of the mean-field BdG Hamiltonian (see equation (4.7) of Chapter 4), is

$$-c^\dagger_{\mathbf{k},\uparrow}\Delta_{\mathbf{k}}(c^\dagger_{-\mathbf{k},\downarrow})^T = -c^\dagger_{\mathbf{k},\uparrow}U^\dagger(\mathbf{k})U(\mathbf{k})\Delta_{\mathbf{k}}(c^\dagger_{-\mathbf{k},\downarrow})^T = -\tilde{c}^\dagger_{\mathbf{k},\uparrow}U(\mathbf{k})\Delta_{\mathbf{k}}(c^\dagger_{-\mathbf{k},\downarrow})^T \tag{D.8}$$

From equation (D.6) we deduce

$$(\tilde{c}^\dagger_{-\mathbf{k},\downarrow})^T = (U^\dagger(-\mathbf{k}))^T(c^\dagger_{-\mathbf{k},\downarrow})^T \tag{D.9}$$

and therefore

$$-\tilde{c}^\dagger_{\mathbf{k},\uparrow}U(\mathbf{k})\Delta_{\mathbf{k}}(U^\dagger(-\mathbf{k})U(-\mathbf{k}))^T(c^\dagger_{-\mathbf{k},\downarrow})^T = -\tilde{c}^\dagger_{\mathbf{k},\uparrow}U(\mathbf{k})\Delta_{\mathbf{k}}(U(-\mathbf{k}))^T(\tilde{c}^\dagger_{-\mathbf{k},\downarrow})^T \tag{D.10}$$

Thus, in accordance with [46], we find that while the normal state Hamiltonian in band space is given by $H^B_{\mathrm{TB}}(\mathbf{k}) = U(\mathbf{k})H_{\mathrm{TB}}(\mathbf{k})U^\dagger(\mathbf{k})$ (the superscript B denoting energy band basis), the order parameter transforms as

$$\Delta^B_{\mathbf{k}} = U(\mathbf{k})\Delta_{\mathbf{k}}U^T(-\mathbf{k}) \tag{D.11}$$

The gap matrix connects particle and hole spaces. If there is only intraband pairing $\Delta^B_{\mathbf{k}}$ is block diagonal. A non block-diagonal gap matrix indicates interband pairing [46].

Appendix E

Illustrations of lattice harmonics of the irreps in the D_6 point group

The lowest order lattice harmonics for the A_2, B_1, B_2, E_1 and E_2 irreps are shown in Figures E.1, E.2, E.3, E.4 and E.5, respectively.

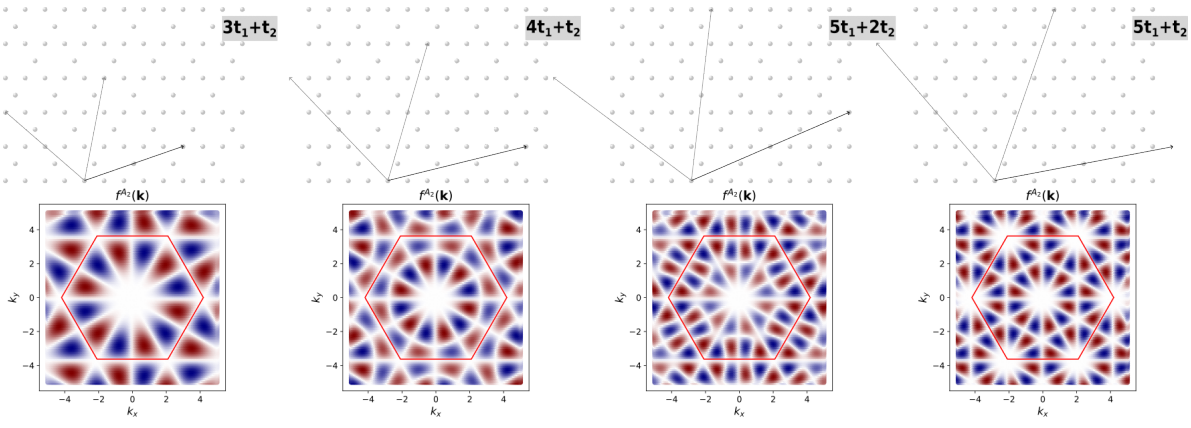

Figure E.1: $f_{\mathbf{a}}^{A_2}(\mathbf{k})$ plotted for four different vectors, $\mathbf{a} = 3\mathbf{t}_1+\mathbf{t}_2, 4\mathbf{t}_1+\mathbf{t}_2, 5\mathbf{t}_1+2\mathbf{t}_2, 5\mathbf{t}_1+\mathbf{t}_2$, yielding the four lowest order lattice harmonics transforming as the A_2 irrep. The hexagonal Brillouin zone is superimposed in red.

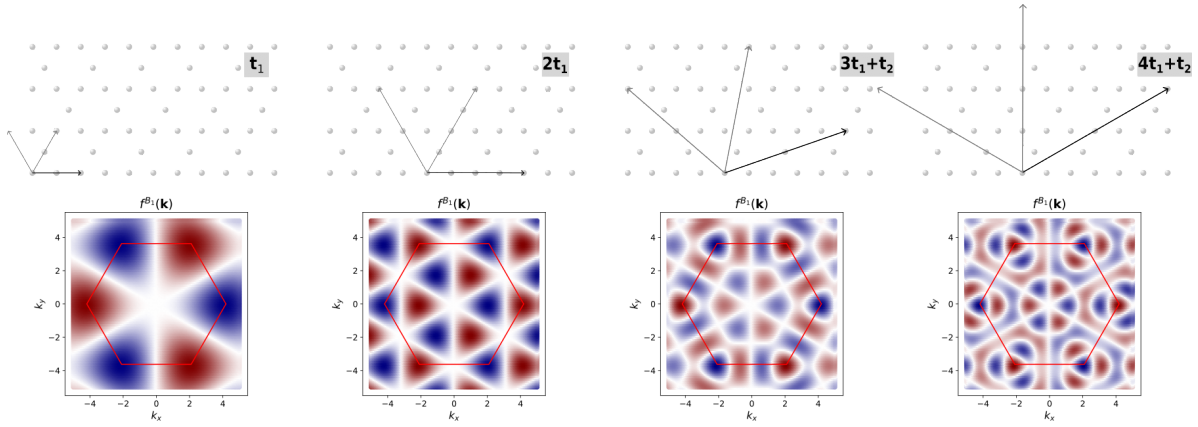

Figure E.2: $f_{\mathbf{a}}^{B_1}(\mathbf{k})$ plotted for four different vectors, $\mathbf{a} = \mathbf{t}_1, 2\mathbf{t}_1, 3\mathbf{t}_1 + \mathbf{t}_2, 4\mathbf{t}_1 + \mathbf{t}_2$, yielding the four lowest order lattice harmonics transforming as the B_1 irrep. The hexagonal Brillouin zone is superimposed in red.

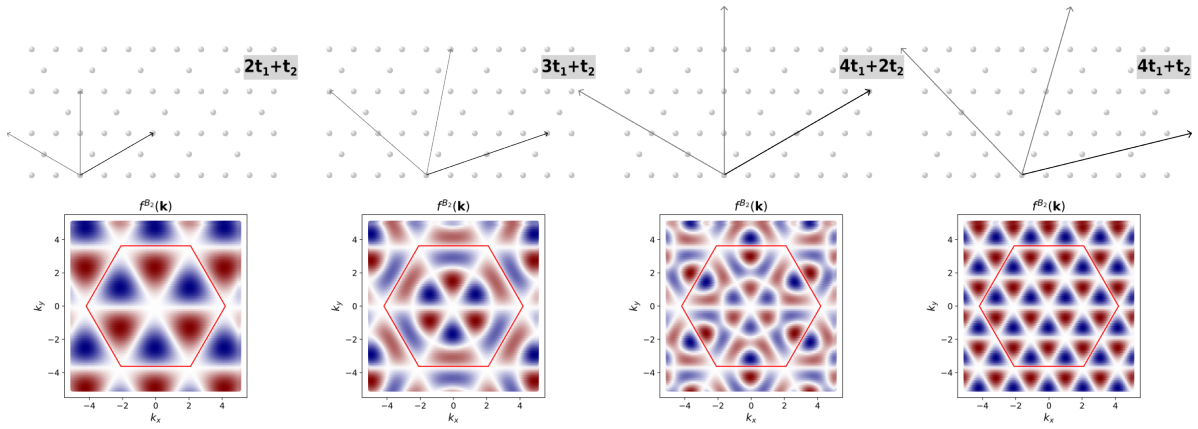

Figure E.3: $f_{\mathbf{a}}^{B_2}(\mathbf{k})$ plotted for four different vectors, $\mathbf{a} = 2\mathbf{t}_1+\mathbf{t}_2, 3\mathbf{t}_1+\mathbf{t}_2, 4\mathbf{t}_1+2\mathbf{t}_2, 4\mathbf{t}_1+\mathbf{t}_2$, yielding the four lowest order lattice harmonics transforming as the B_2 irrep. The hexagonal Brillouin zone is superimposed in red.

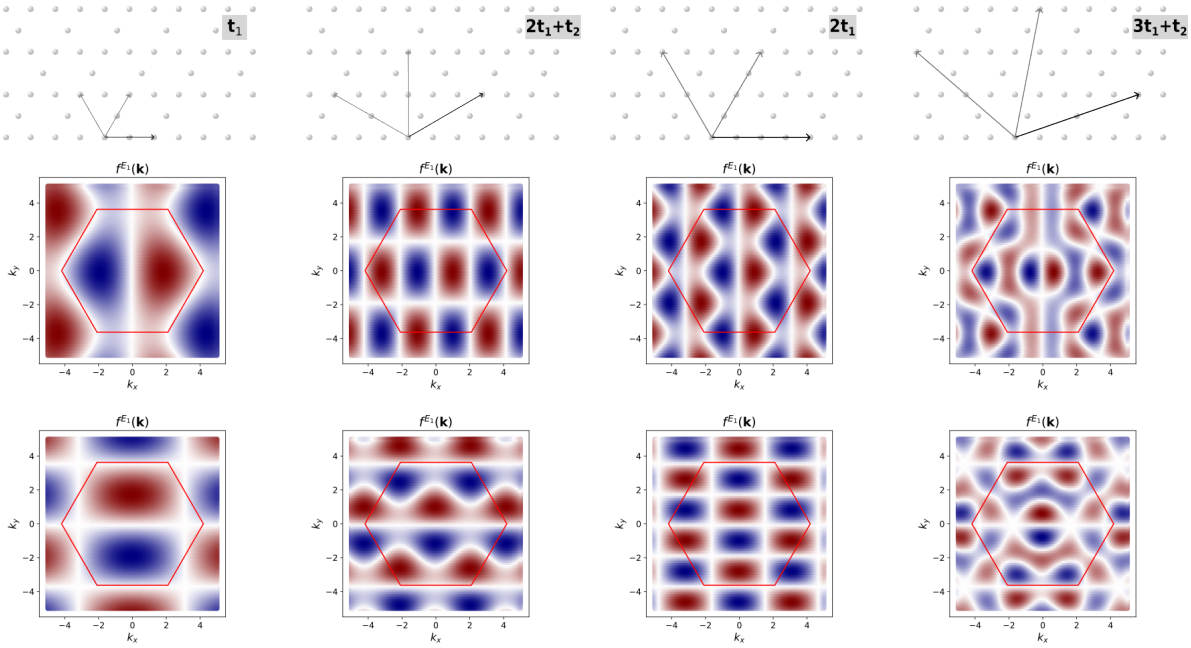

Figure E.4: $f_{\mathbf{a}}^{E_1}(\mathbf{k})$ plotted for four different vectors, $\mathbf{a} = \mathbf{t}_1, 2\mathbf{t}_1 + \mathbf{t}_2, 2\mathbf{t}_1, 3\mathbf{t}_1 + \mathbf{t}_2$, yielding the four lowest order lattice harmonics transforming as the E_1 irrep. The upper row corresponds to $f_{\mathbf{a}}^{E_1}(\mathbf{k})_{11}$ and the lower row to $f_{\mathbf{a}}^{E_1}(\mathbf{k})_{21}$. The hexagonal Brillouin zone is superimposed in red.

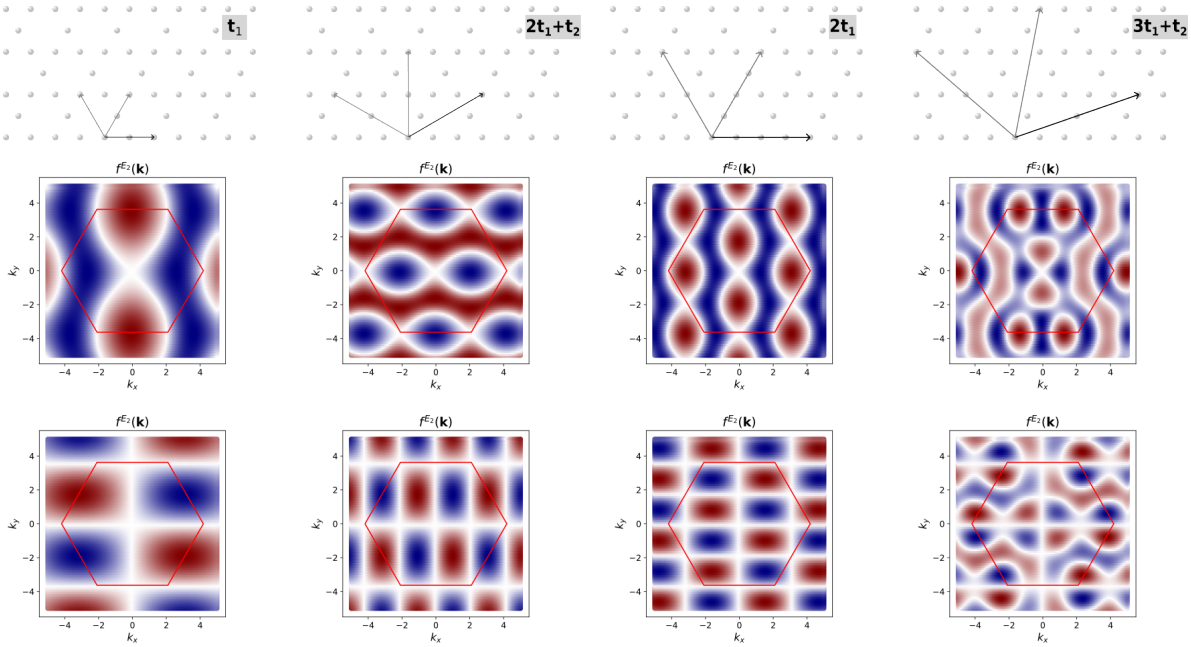

Figure E.5: $f_{\mathbf{a}}^{E_2}(\mathbf{k})$ plotted for four different vectors, $\mathbf{a} = \mathbf{t}_1, 2\mathbf{t}_1 + \mathbf{t}_2, 2\mathbf{t}_1, 3\mathbf{t}_1 + \mathbf{t}_2$, yielding the four lowest order lattice harmonics transforming as the E_2 irrep. The upper row corresponds to $f_{\mathbf{a}}^{E_2}(\mathbf{k})_{11}$ and the lower row to $f_{\mathbf{a}}^{E_2}(\mathbf{k})_{21}$. The hexagonal Brillouin zone is superimposed in red.

Appendix F

Self-consistent solution of Bogoliubov-de-Gennes gap equation

In this section we derive the gap equation for the kagome lattice which has the additional sublattice degree of freedom. The starting point is the following interaction between an electron and its time-reversed partner

$$\mathcal{H}_{\text{int}} = \frac{1}{N^2} \sum_{\mathbf{k},\mathbf{k}',s_1,s_2,s_3,s_4} V^{s_1,s_2,s_3,s_4}_{\mathbf{k},\mathbf{k}'} c^\dagger_{s_1,\mathbf{k},\uparrow} c^\dagger_{s_2,-\mathbf{k},\downarrow} c_{s_3,-\mathbf{k}',\downarrow} c_{s_4,\mathbf{k}',\uparrow} \,. \tag{F.1}$$

Diagrammatically, the interaction is shown in Figure F.1. To obtain a mean-field theory, it is assumed that fluctuations of the form

$$\delta c^\dagger_{s_1,\mathbf{k},\uparrow} c^\dagger_{s_2,-\mathbf{k},\downarrow} = c^\dagger_{s_1,\mathbf{k},\uparrow} c^\dagger_{s_2,-\mathbf{k},\downarrow} - \langle c^\dagger_{s_1,\mathbf{k},\uparrow} c^\dagger_{s_2,-\mathbf{k},\downarrow} \rangle \tag{F.2}$$

are small and we define $(A^{s_1,s_2}_{\mathbf{k}})^\dagger \equiv c^\dagger_{s_1,\mathbf{k},\uparrow} c^\dagger_{s_2,-\mathbf{k},\downarrow}$ ($A^{s_3,s_4}_{\mathbf{k}'} \equiv c_{s_3,-\mathbf{k}',\downarrow} c_{s_4,\mathbf{k}',\uparrow}$) to simplify the expressions. The interaction to first order in fluctuations then becomes

$$\begin{aligned}
\mathcal{H}_{\text{int}} &= \frac{1}{N^2} \sum_{\mathbf{k},\mathbf{k}',s_1,s_2,s_3,s_4} V^{s_1,s_2,s_3,s_4}_{\mathbf{k},\mathbf{k}'} (\delta (A^{s_1,s_2}_{\mathbf{k}})^\dagger + \langle (A^{s_1,s_2}_{\mathbf{k}})^\dagger \rangle)(\delta A^{s_3,s_4}_{\mathbf{k}'} + \langle A^{s_3,s_4}_{\mathbf{k}'} \rangle) \\
&\approx \frac{1}{N^2} \sum_{\mathbf{k},\mathbf{k}',s_1,s_2,s_3,s_4} V^{s_1,s_2,s_3,s_4}_{\mathbf{k},\mathbf{k}'} (\delta (A^{s_1,s_2}_{\mathbf{k}})^\dagger \langle A^{s_3,s_4}_{\mathbf{k}'} \rangle + \delta A^{s_3,s_4}_{\mathbf{k}'} \langle (A^{s_1,s_2}_{\mathbf{k}})^\dagger \rangle + \langle (A^{s_1,s_2}_{\mathbf{k}})^\dagger \rangle \langle A^{s_3,s_4}_{\mathbf{k}'} \rangle) \\
&= \frac{1}{N^2} \sum_{\mathbf{k},\mathbf{k}',s_1,s_2,s_3,s_4} V^{s_1,s_2,s_3,s_4}_{\mathbf{k},\mathbf{k}'} (\langle A^{s_3,s_4}_{\mathbf{k}'} \rangle (A^{s_1,s_2}_{\mathbf{k}})^\dagger + \langle (A^{s_1,s_2}_{\mathbf{k}})^\dagger \rangle A^{s_3,s_4}_{\mathbf{k}'} - \langle A^{s_3,s_4}_{\mathbf{k}'} \rangle \langle (A^{s_1,s_2}_{\mathbf{k}})^\dagger \rangle) \\
&= \frac{-1}{N} \sum_{\mathbf{k}} (\sum_{s_1,s_2} \Delta^{s_1,s_2}_{\mathbf{k}} c^\dagger_{s_1,\mathbf{k},\uparrow} c^\dagger_{s_2,-\mathbf{k},\downarrow} + \sum_{s_3,s_4} (\Delta^{s_3,s_4}_{\mathbf{k}})^\dagger c_{s_3,-\mathbf{k},\downarrow} c_{s_4,\mathbf{k},\uparrow}) + C = \mathcal{H}^{MF}_{\text{int}} + C \,,
\end{aligned} \tag{F.3}$$

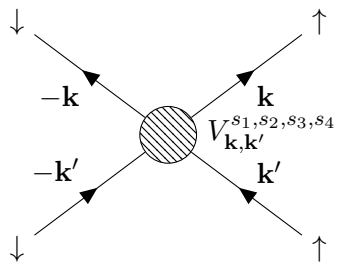

Figure F.1: The interaction in equation (F.1).

where C is a constant term and

$$\Delta_{\mathbf{k}}^{s_1,s_2} = \frac{-1}{N}\sum_{\mathbf{k}',s_3,s_4} V_{\mathbf{k},\mathbf{k}'}^{s_1,s_2,s_3,s_4}\left\langle c_{s_3,-\mathbf{k}',\downarrow}c_{s_4,\mathbf{k}',\uparrow}\right\rangle = \frac{V_{\mathrm{SC}}}{N}(f_{\mathbf{k}}^{s_2,s_1})^*\sum_{\mathbf{k}',s_3,s_4} f_{\mathbf{k}'}^{s_3,s_4}\left\langle c_{s_3,-\mathbf{k}',\downarrow}c_{s_4,\mathbf{k}',\uparrow}\right\rangle . \quad \text{(F.4)}$$

Here it was assumed that the pairing potential can be divided into two functions which transform according to the irrep of our interest, thus $V_{\mathbf{k},\mathbf{k}'}^{s_1,s_2,s_3,s_4} = -V_{\mathrm{SC}}(f_{\mathbf{k}}^{s_2,s_1})^* f_{\mathbf{k}'}^{s_3,s_4}$. Solving the equation by a Bogoliubov transformation which we choose to define as

$$\begin{pmatrix} c_{s,\mathbf{k},\uparrow} \\ c_{s,-\mathbf{k},\downarrow}^\dagger \end{pmatrix} = \begin{pmatrix} u_{s,n}(\mathbf{k}) & v_{s,n}(\mathbf{k}) \\ v_{s,n}^*(\mathbf{k}) & -u_{s,n}^*(\mathbf{k}) \end{pmatrix}\begin{pmatrix} \gamma_{n,\mathbf{k},\uparrow} \\ \gamma_{n,-\mathbf{k},\downarrow}^\dagger \end{pmatrix} . \quad \text{(F.5)}$$

The detailed form of the unitary matrix is

$$\begin{pmatrix} u_{A,1} & u_{A,2} & u_{A,3} & v_{A,1} & v_{A,2} & v_{A,3} \\ u_{B,1} & u_{B,2} & u_{B,3} & v_{B,1} & v_{B,2} & v_{B,3} \\ u_{C,1} & u_{C,2} & u_{C,3} & v_{C,1} & v_{C,2} & v_{C,3} \\ v_{A,1}^* & v_{A,2}^* & v_{A,3}^* & -u_{A,1}^* & -u_{A,2}^* & -u_{A,3}^* \\ v_{B,1}^* & v_{B,2}^* & v_{B,3}^* & -u_{B,1}^* & -u_{B,2}^* & -u_{B,3}^* \\ v_{C,1}^* & v_{C,2}^* & v_{C,3}^* & -u_{C,1}^* & -u_{C,2}^* & -u_{C,3}^* \end{pmatrix} , \quad \text{(F.6)}$$

where we have suppressed the momentum dependence. Additionally

$$\begin{pmatrix} c_{s,\mathbf{k},\uparrow}^\dagger & c_{s,-\mathbf{k},\downarrow} \end{pmatrix} = \begin{pmatrix} \gamma_{n,\mathbf{k},\uparrow}^\dagger & \gamma_{n,-\mathbf{k},\downarrow} \end{pmatrix}\begin{pmatrix} u_{n,s}^*(\mathbf{k}) & v_{n,s}(\mathbf{k}) \\ v_{n,s}^*(\mathbf{k}) & -u_{n,s}(\mathbf{k}) \end{pmatrix} . \quad \text{(F.7)}$$

Thus

$$\begin{aligned}
&\frac{N}{V_{\mathrm{SC}}}\Delta_{\mathbf{k}}^{s_1,s_2} = \\
&(f_{\mathbf{k}}^{s_2,s_1})^*\sum_{\mathbf{k}',s_3,s_4} f_{\mathbf{k}'}^{s_3,s_4}\left\langle[\sum_n v_{n,s_3}(\mathbf{k}')\gamma_{n,\mathbf{k}',\uparrow}^\dagger - u_{n,s_3}(\mathbf{k}')\gamma_{n,-\mathbf{k}',\downarrow}][\sum_n u_{s_4,n}(\mathbf{k}')\gamma_{n,\mathbf{k}',\uparrow} + v_{s_4,n}(\mathbf{k}')\gamma_{n,-\mathbf{k}',\downarrow}^\dagger]\right\rangle \\
&= (f_{\mathbf{k}}^{s_2,s_1})^*\sum_{\mathbf{k}',s_3,s_4} f_{\mathbf{k}'}^{s_3,s_4}[\sum_n v_{n,s_3}(\mathbf{k}')u_{s_4,n}(\mathbf{k}')\left\langle\gamma_{n,\mathbf{k}',\uparrow}^\dagger\gamma_{n,\mathbf{k}',\uparrow}\right\rangle - u_{n,s_3}(\mathbf{k}')v_{s_4,n}(\mathbf{k}')\left\langle\gamma_{n,-\mathbf{k}',\downarrow}\gamma_{n,-\mathbf{k}',\downarrow}^\dagger\right\rangle] \\
&= (f_{\mathbf{k}}^{s_2,s_1})^*\sum_{\mathbf{k}',s_3,s_4} f_{\mathbf{k}'}^{s_3,s_4}[\sum_n v_{n,s_3}(\mathbf{k}')u_{s_4,n}(\mathbf{k}')n_F(E_{n,\mathbf{k}'}) - u_{n,s_3}(\mathbf{k}')v_{s_4,n}(\mathbf{k}')(1-n_F(E_{n,-\mathbf{k}'}))] \\
&= (f_{\mathbf{k}}^{s_2,s_1})^*\sum_{\mathbf{k}'}[\sum_n n_F(E_{n,\mathbf{k}'})\sum_{s_3} v_{n,s_3}(\mathbf{k}')\sum_{s_4} f_{\mathbf{k}'}^{s_3,s_4}u_{s_4,n}(\mathbf{k}') \\
&- (1-n_F(E_{n,\mathbf{k}'}))\sum_{s_3} u_{n,s_3}(\mathbf{k}')\sum_{s_4} f_{\mathbf{k}'}^{s_3,s_4}v_{s_4,n}(\mathbf{k}')] \qquad \text{(F.8)}
\end{aligned}$$

where $n = 1,2,3$ is a sum over bands, and it was used that since $H(\mathbf{k}) = H(-\mathbf{k})$ then $E_n(\mathbf{k}) = E_n(-\mathbf{k})$ (this is easily proved by using the fact that if the Hamiltonian is invariant under a C_2 operation, i.e. commutes with the C_2 operator, then, transforming into band space, the diagonal Hamiltonian is also invariant under the corresponding C_2 operation in the band space basis). Furthermore, it was used that in the diagonal Hamiltonian, the bogoliubons are free fermions and therefore their distribution follows the regular Fermi-Dirac distribution $\left\langle\gamma_{n,\mathbf{k}',\uparrow}^\dagger\gamma_{n,\mathbf{k}',\uparrow}\right\rangle = n_F(E_{n,\mathbf{k}'})$. The final expression of equation (F.8) is written such that the matrix form is clear: the n sum is a trace and the s_3 and s_4 sums are matrix multiplications. An algorithm which self-consistently solves for $\Delta_{\mathbf{k}}^{s_1,s_2}$ is the following

1. Guess an initial $\Delta_{\mathbf{k}}^i$.

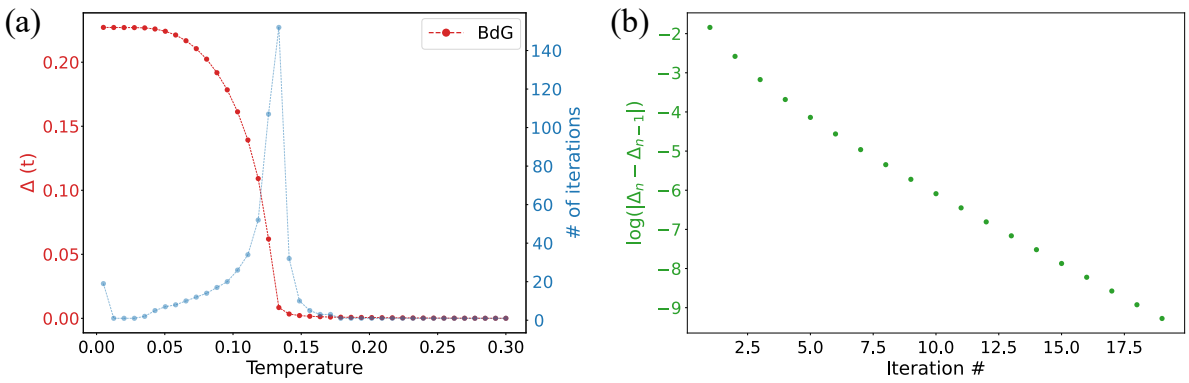

Figure F.2: (a) Example of a gap calculated from equation (F.8) and plotted for a range of temperatures T (red). For the numerical calculation, a momentum grid containing 3600 **k**-points in the first Brillouin zone was used. The chemical potential $\mu = 0.4$ and $V_{\mathrm{SC}} = 2$ in equation (F.8). The number of iterations required for convergence (blue) increases at the critical temperature. (b) The (logarithm of the) absolute difference between the order parameter calculated in the current iteration step, Δ_n, and the former, Δ_{n-1}.

2. Diagonalize $H_{\mathrm{BdG}} = H_{\mathrm{TB}} + H_{\mathrm{int}}^{MF}$.
3. Calculate a new $\Delta_{\mathbf{k}}^{f}$ using equation (F.8).
4. Set $\Delta_{\mathbf{k}}^{i} = \Delta_{\mathbf{k}}^{f}$.
5. Repeat until a predefined convergence criteria is satisfied.

The algorithm is run for a set of temperatures T to obtain the result in Figure F.2. Since we use the absolute difference between the order parameter calculated in the current iteration step, Δ_n, and the former, Δ_{n-1}, to conclude convergence it was checked whether this difference smoothly decreases or whether it has jumps. In the latter case it could be more advantageous to update the order parameter according to $\Delta^i = \alpha\Delta^i + (1-\alpha)\Delta^f$ with $\alpha \in (0,1)$. The convergence criteria was in general set be a difference of maximally 10^{-5}. As the initial guess of Δ^i for all temperatures different than the first one we used the final value of Δ from the former temperature. This generally decreases the number of iterations needed but it only works if the code can run in series and not if one wants to run for each temperature in parallel.

Bibliography

[1] van Delft, D. & Kes, P. The discovery of superconductivity. *Physics Today* **63**, 38–43 (2010). URL https://doi.org/10.1063/1.3490499. https://pubs.aip.org/physicstoday/article-pdf/63/9/38/9879861/38_1_online.pdf.

[2] Ray, P. J. Figure 2.4 in Master thesis, "Structural investigation of $La_{2-x}Sr_xCuO_{4+y}$ - Following staging as a function of temperature" (2015).

[3] Bardeen, J., Cooper, L. N. & Schrieffer, J. R. Theory of Superconductivity. *Phys. Rev.* **108**, 1175–1204 (1957). URL https://link.aps.org/doi/10.1103/PhysRev.108.1175.

[4] Sigrist, M. Introduction to Unconventional Superconductivity. *AIP Conference Proceedings* **789**, 165–243 (2005). URL https://doi.org/10.1063/1.2080350. https://pubs.aip.org/aip/acp/article-pdf/789/1/165/11444756/165_1_online.pdf.

[5] Parks, R. *Superconductivity: Part 2 (In Two Parts)*. Superconductivity (Taylor & Francis, 1969). URL https://books.google.dk/books?id=D4hK-yGBEmoC.

[6] Bednorz, J. G. & Müller, K. A. Possible high-T_c superconductivity in the $BaLaCuO$ system. *Zeitschrift für Physik B Condensed Matter* **64**, 189–193 (1986). URL https://doi.org/10.1007/BF01303701.

[7] Norman, M. R. Entering the Nickel Age of Superconductivity. *Physics* **13** (2020). URL https://physics.aps.org/articles/v13/85.

[8] Holbæk, S. C., Christensen, M. H., Kreisel, A. & Andersen, B. M. Unconventional superconductivity protected from disorder on the kagome lattice (2023). 2307.12861.

[9] Ortiz, B. R. *et al.* New kagome prototype materials: discovery of KV_3Sb_5, RbV_3Sb_5, and CsV_3Sb_5. *Phys. Rev. Mater.* **3**, 094407 (2019). URL https://link.aps.org/doi/10.1103/PhysRevMaterials.3.094407.

[10] Ortiz, B. R. *et al.* CsV_3Sb_5: A $\mathbb{Z}_2$ Topological Kagome Metal with a Superconducting Ground State. *Phys. Rev. Lett.* **125**, 247002 (2020). URL https://link.aps.org/doi/10.1103/PhysRevLett.125.247002.

[11] Ortiz, B. R. *et al.* Superconductivity in the $\mathbb{Z}_2$ kagome metal KV_3Sb_5. *Phys. Rev. Mater.* **5**, 034801 (2021). URL https://link.aps.org/doi/10.1103/PhysRevMaterials.5.034801.

[12] Yin, Q. *et al.* Superconductivity and Normal-State Properties of Kagome Metal RbV_3Sb_5 Single Crystals. *Chinese Physics Letters* **38**, 037403 (2021). URL https://dx.doi.org/10.1088/0256-307X/38/3/037403.

[13] Jiang, K. *et al.* Kagome superconductors AV_3Sb_5 $(A = K, Rb, Cs)$. *National Science Review* **10** (2022). URL https://doi.org/10.1093%2Fnsr%2Fnwac199.

[14] Ortiz, B. R. *et al.* Complete miscibility amongst the AV_3Sb_5 kagome superconductors: Design of mixed A-site AV_3Sb_5 (A: K, rb, cs) alloys. *Phys. Rev. Mater.* **7**, 014801 (2023). URL https://link.aps.org/doi/10.1103/PhysRevMaterials.7.014801.

[15] Yu, F. H. *et al.* Unusual competition of superconductivity and charge-density-wave state in a compressed topological kagome metal. *Nature Communications* **12**, 3645 (2021). URL https://doi.org/10.1038/s41467-021-23928-w.

[16] Jiang, Y.-X. *et al.* Unconventional chiral charge order in kagome superconductor KV_3Sb_5. *Nature Materials* **20**, 1353–1357 (2021). URL https://doi.org/10.1038/s41563-021-01034-y.

[17] Roppongi, M. *et al.* Bulk evidence of anisotropic s-wave pairing with no sign change in the kagome superconductor CsV_3Sb_5. *Nature Communications* **14**, 667 (2023). URL https://doi.org/10.1038/s41467-023-36273-x.

[18] Buiarelli, L. Master's thesis, "Structural properties of kagome-layered crystals" (2023).

[19] Buiarelli, L. Private communication (2023).

[20] Xu, H.-S. *et al.* Multiband superconductivity with Sign-Preserving Order Parameter in Kagome Superconductor CsV_3Sb_5. *Phys. Rev. Lett.* **127**, 187004 (2021). URL https://link.aps.org/doi/10.1103/PhysRevLett.127.187004.

[21] Zhang, W. *et al.* Nodeless Superconductivity in Kagome Metal CsV_3Sb_5 with and without Time Reversal Symmetry Breaking. *Nano Letters* **23**, 872–879 (2023). URL https://doi.org/10.1021/acs.nanolett.2c04103.

[22] Mielke, C. *et al.* Time-reversal symmetry-breaking charge order in a kagome superconductor. *Nature* **602**, 245–250 (2022). URL https://doi.org/10.1038%2Fs41586-021-04327-z.

[23] Kang, M. *et al.* Twofold van Hove singularity and origin of charge order in topological kagome superconductor CsV_3Sb_5. *Nature Physics* **18**, 301–308 (2022). URL https://doi.org/10.1038/s41567-021-01451-5.

[24] Haverkort, M. W., Elfimov, I. S., Tjeng, L. H., Sawatzky, G. A. & Damascelli, A. Strong Spin-Orbit Coupling Effects on the Fermi Surface of Sr_2RuO_4 and Sr_2RhO_4. *Phys. Rev. Lett.* **101**, 026406 (2008). URL https://link.aps.org/doi/10.1103/PhysRevLett.101.026406.

[25] Ritz, E. *et al.* Superconductivity from Orbital-Selective Electron-Phonon Coupling in AV_3Sb_5 (2023). 2304.14822.

[26] Hellebek, E. Master thesis, "Charge order in kagome metals" (2022).

[27] Hu, Y. *et al.* Rich nature of Van Hove singularities in Kagome superconductor CsV_3Sb_5. *Nature Communications* **13**, 2220 (2022). URL https://doi.org/10.1038/s41467-022-29828-x.

[28] Kiesel, M. L. & Thomale, R. Sublattice interference in the kagome Hubbard model. *Physical Review B* **86** (2012). URL https://doi.org/10.1103%2Fphysrevb.86.121105.

[29] Denner, M. M., Thomale, R. & Neupert, T. Analysis of Charge Order in the Kagome Metal. *Physical Review Letters* **127** (2021). URL https://doi.org/10.1103%2Fphysrevlett.127.217601.

[30] Grinenko, V. *et al.* Unsplit superconducting and time reversal symmetry breaking transitions in Sr_2RuO_4 under hydrostatic pressure and disorder. *Nature Communications* **12** (2021). URL https://doi.org/10.1038%2Fs41467-021-24176-8.

[31] Bruus, H. & Flensberg, K. *Many-Body Quantum Theory in Condensed Matter Physics: An Introduction*. Oxford Graduate Texts (OUP Oxford, 2004). URL https://books.google.dk/books?id=v5vhg1tYLC8C.

[32] Katzer, G. Character table for the D_6 point group. URL http://gernot-katzers-spice-pages.com/character_tables/D6.html. Accessed on March 14, 2023.

[33] Arovas, D. Lecture Notes on Group Theory in Physics (A Work in Progress) (2022).

[34] Mineev, V., Samokhin, K. & Landau, L. *Introduction to Unconventional Superconductivity* (Taylor & Francis, 1999). URL https://books.google.dk/books?id=2BXYWT8m068C.

[35] Ding, P., Lee, C. H., Wu, X. & Thomale, R. Diagnosis of pairing symmetry by vortex and edge spectra in kagome superconductors. *Phys. Rev. B* **105**, 174518 (2022). URL https://link.aps.org/doi/10.1103/PhysRevB.105.174518.

[36] Andersen, B. M. Coexistence of Magnetic and Superconducting Order in the High-T_c Materials (2004).

[37] Wang, Q.-H. & Wang, Z. D. Impurity and interface bound states in $d_{x^2-y^2}+id_{xy}$ and p_x+ip_y superconductors. *Phys. Rev. B* **69**, 092502 (2004). URL https://link.aps.org/doi/10.1103/PhysRevB.69.092502.

[38] Server, M. R. Master thesis, "Theoretical Studies of Superconductivity in Sr_2RuO_4" (2021).

[39] Anderson, P. Theory of dirty superconductors. *Journal of Physics and Chemistry of Solids* **11**, 26–30 (1959). URL https://www.sciencedirect.com/science/article/pii/0022369759900368.

[40] Rømer, A. T., Hirschfeld, P. J. & Andersen, B. M. Raising the Critical Temperature by Disorder in Unconventional Superconductors Mediated by Spin Fluctuations. *Phys. Rev. Lett.* **121**, 027002 (2018). URL https://link.aps.org/doi/10.1103/PhysRevLett.121.027002.

[41] Gastiasoro, M. N., Bernardini, F. & Andersen, B. M. Unconventional Disorder Effects in Correlated Superconductors. *Phys. Rev. Lett.* **117**, 257002 (2016). URL https://link.aps.org/doi/10.1103/PhysRevLett.117.257002.

[42] Kamppinen, T., Rysti, J., Volard, M.-M., Volovik, G. E. & Eltsov, V. B. Topological nodal line in superfluid ^3He and the Anderson theorem. *Nature Communications* **14**, 4276 (2023). URL https://doi.org/10.1038/s41467-023-39977-2.

[43] Andersen, L., Ramires, A., Wang, Z., Lorenz, T. & Ando, Y. Generalized Anderson's theorem for superconductors derived from topological insulators. *Science Advances* **6**, eaay6502 (2020). URL https://www.science.org/doi/abs/10.1126/sciadv.aay6502. https://www.science.org/doi/pdf/10.1126/sciadv.aay6502.

[44] Zinkl, B. & Ramires, A. Sensitivity of superconducting states to the impurity location in layered materials. *Phys. Rev. B* **106**, 014515 (2022). URL https://link.aps.org/doi/10.1103/PhysRevB.106.014515.

[45] Möckli, D. & Ramires, A. Superconductivity in disordered locally noncentrosymmetric materials: An application to $CeRh_2As_2$. *Phys. Rev. B* **104**, 134517 (2021). URL https://link.aps.org/doi/10.1103/PhysRevB.104.134517.

[46] Ramires, A. Nonunitary superconductivity in complex quantum materials. *Journal of Physics: Condensed Matter* **34**, 304001 (2022). URL https://dx.doi.org/10.1088/1361-648X/ac6d3a.